PhD Thesis

A Trigger System with Online Track Recognition for the μ–e Conversion Search in the COMET Phase-I Experiment

Author:
Yu Nakazawa

Supervisor:
Prof. Masaharu Aoki

December 19, 2020

Abstract

The COMET Phase-I experiment searches for the muon-to-electron conversion in an aluminium muonic atom, which is strongly prohibited in the Standard Model. It could probe a new physics process beyond the Standard Model. The design value of the experimental single event sensitivity is 3.0×10^{-15} in a 150 day-long physics measurement. To this end, a highly intense pulsed muon beam and a detector system are constructed at the Japan Proton Accelerator Research Complex (J-PARC). The detector system consists of a cylindrical drift chamber (CDC) with about 5000 channels and 96 arrays of trigger hodoscopes. The drift chamber measures positions of the conversion-electron track to evaluate its momentum, and the hodoscopes measure its timing.

An initial simulation study indicates the use of the new muon beam gives an unacceptably high trigger rate for the data acquisition system. Therefore, a fast online trigger system has been designed. This system is called the COMET trigger (COTTRI) system. The COTTRI system handles hit information of the CDC to make triggers only for signal-like events using field-programmable gate arrays (FPGAs). FPGA-based electronics – ten front-end boards and one merger board – compose the COTTRI system. On the front-end boards, data from each CDC channel is classified into signal-like and background-like hits by using look-up tables. The merger board collects the data from all the channels and sends it to the central trigger system, which makes the trigger decision using the information of the other detectors. The data acquisition system requires a trigger rate of less than 26 kHz. The total processing time of the full trigger system must be less than 7 μs due to the buffering time of the CDC readout electronics.

Both the front-end and merger boards for the trigger system were designed and produced. The firmware written in the hardware description language was also developed for the both. The COTTRI system was installed in the full trigger system, and the total processing time was measured. It was 3.1 μs and met the requirement. A 12-hour operation test of the COTTRI system was performed using one-sixth of the CDC readout region in a setup of a cosmic-ray measurement. As a result, the data transfer and processing in the COTTRI system were demonstrated to be robust and stable.

The performance of the COTTRI system was estimated by applying the full simulation of the COMET Phase-I experiment. In this Monte Carlo study, 9215 bunches were produced. Data of each CDC channel is classified by gradient boosted decision trees that generate the lookup tables on the front-end boards mentioned before. In the final trigger decision, a geometrical filter by the combination of hit positions in the CDC and hodoscopes makes the background suppression even higher. Since the pulsed beam is adapted, the background level in the detector system changes with time; the time window of measurement is delayed. The background level in the detector system changes with time because the pulse beam is adapted. For this reason, the time window of measurement is set to be delayed from the beam bunch timing. Possible patterns of the time window were considered. The COTTRI system provides a signal-event acceptance of 86.0% to 96.8% for any time window while keeping the trigger rate of 13 kHz with a safety factor of two.

Acknowledgements

I express my deeply gratitude to Prof. Yoshitaka Kuno. He gave me an opportunity to work on the COMET experiment. Thanks to this, I could enjoy many experiences with many collaborators. I would like to thank Prof. Masaharu Aoki for giving me constructive comments and warm encouragement. I also thank Dr. Akira Sato for helpful advice in meetings. We also enjoyed going fishing as private sessions.

I am deeply grateful to Dr. Yuki Fujii for teaching me many essential points in the trigger development. We had many enjoyable discussions not only of things related with the development but of other experimental physics results. He might endure my stupid questions and mistakes sometimes.

I would like to show my appreciation to Dr. Hisataka Yoshida. He supported me from the start to the end of my researches. To Dr. Manabu Moritsu, thank you for management of the detector system.

I would like to thank Prof. Satoshi Mihara for supporting to develop the trigger system in KEK. My heartfelt appreciation goes to Dr. Kazuki Ueno. He organised the radiation hardness group in the COMET experiment, and we had many radiation tests for the part selection for the electronics. Thanks to the positive result of them, the trigger electronics could be designed. Thank all the members of the radiation hardness group for working with me. I offer my thanks to Kazuki and Masayoshi Shoji. They supported the development of the trigger electronics very much. Thank Dr. Tomohisa Uchida and Eitaro Hamada so much for giving me advice and comments about coding the hardware description language.

To Kou Oishi, thank you for teaching me how to use the simulation code. To Dr. Yuki Nakai, thank you for teaching me characteristics of the trigger counters which he has developed.

I am thankful to Chen Wu and Dr. TingSam Wong for teaching me the ABC of the simulation work. To Dorian Pieters and Giorgi Kumsiahvili, thank you for proofreading the manuscript and encouraging me many times. To Dr. Takahisa Itahashi, Dr. Yoshio Koide, and Dr. Yoshitaka Kawashima, I feel appreciation about telling me their helpful experiences and their wonderful feature works. They are very diligent, and therefore I respect them. Thank Yoshiki Sato and Yuya Higuchi for assistance with the mass production of the simulation data in this study. I appreciate all the members of our laboratory, Daiki Nagao, Yao Weichao, Yuta Higashino, Sun SiYuan, and Yuki Nishimura.

Finally, I owe a deep gratitude to mum and dad. Without their supports, I could not stand at the starting line of my physics life. I am proud of my family.

Contents

List of Figures

List of Tables

Chapter 1

Introduction

The Standard Model (SM) in particle physics successfully depicts and predicts a lot of phenomena. Nevertheless, the SM misses explanations of some remaining issues, such as the existence of dark matter, the matter-antimatter asymmetry of the Universe. We are looking forward to conclusive evidence of new physics beyond the SM. This chapter introduces a powerful tool for a new physics search, a neutrinoless coherent transition of a muon into an electron in a muonic atom.

1.1 Muon

In 1937, three papers reported the observation of a particle in cosmic-ray events [1, 2, 3]. The mass of this particle was not the same as the electron mass whilst its charge is the same as the electron charge. It was initially believed that this particle is a mesotron predicted by Yukawa in 1934 [4]. The subsequent experiments measured the nature of mesotron. In 1947, Fermi and Teller pointed out a disagreement between the theoretical expectations and an experimental result [5] where the behavior of positive and negative mesotrons had been compared [6]. At that time, the muon (μ) appeared for the first time. The mesotron was discovered after the muon and named pion. This is a story of the muon discovery.

In the SM, the muon is the 2nd generation of charged lepton. The muon mass is $105.6\,\mathrm{MeV/c^2}$, which is about 200 times larger than the electron mass, and its lifetime is $2.2\,\mu\mathrm{s}$. The muon interacts with matter via not the strong force but the electroweak and gravity forces. In the SM, free muons decay into an electron and two neutrinos with the branching ratio of almost 100% [7]. In addition to these three particles, either a gamma ray or an electron-positron pair is very rarely contained in the final product, too.

After the first pion production by using an accelerator in the 1960s, accelerator-produced pions were used to obtain artificial muon sources. The powerful muon sources, nowadays, were constructed around the world. Thus, the muons, the second-generation elementary particle that is relatively easy to produce in large quantities, are used in research for further understanding the SM and discovery of new physics. Muon rare decay searches and precision measurement of the g-2 anomaly [8] attract attention.

1.2 Charged lepton flavour violation

In the pre-modern SM where neutrinos were assumed to be mass-less, lepton flavour must be conserved. In the charged-lepton sector, many experiments searched for processes violating lepton flavour for each generation, which corresponds to the lepton family number. Those phenomena are widely known as charged lepton flavour violation (CLFV).

In 1998, the first observation of neutrino oscillation was reported [9], and it indicates that flavour in the neutral-lepton sector is not conserved. Then, a muon has a chance to transit into an electron without neutrino emissions by mediating the neutrino oscillation. The transition, however, is extremely suppressed by the mass ratio between the neutrino and the W-boson. In the SM extended by the neutrino oscillation, the branching ratio of $\mu^- \to e^-\gamma$ is predicted by:

$$\mathcal{BR}\left(\mu \to e\gamma\right) = \frac{3\alpha}{32\pi}\left|\sum_{i=2,3} U^*_{\mu i} U_{ei} \frac{\delta m^2_{i1}}{M^2_W}\right|^2 \sim \mathcal{O}\left(10^{-54}\right), \tag{1.1}$$

where α is the fine structure constant, U_{ji} is an element of the Pontecorvo-Maki-Nakagawa-Sakata (PMNS) matrix defined by a flavour sector of j and a mass eigenstate i, δm^2_{i1} is a squared mass difference between the 1-st and i-th eigenstates, and M_W is the mass of W boson [10].

1.3 CLFV searches

After the muon discovery, many experiments were dedicated to elucidating the nature of the muon. At that time, the muon was actually known as a mesotron predicted by Yukawa. In 1947, the first experiment, which searched for $\mu^- \to e^-\gamma$ using the cosmic rays, was reported [11]. The mesotron decay was expected to emit an electron and a single neutrino, as suggested by the Yukawa explanation [12], but it had not been verified. The purpose of this experiment was to test an alternative hypothesis that the mesotron decayed into an electron and a photon. The experiments followed this have been performed to search for rare muon decays, such as the $\mu^- \to e^-\gamma$ process, the $\mu \to eee$ process, and the muon-to-electron conversion in a nucleus ($\mu \to e$ conversion). The current motivation of the search is to discover the evidence of new physics.

The branching ratio for each process has been gradually improved for $\sim$ 70 years. The history of the CLFV searches is summarised in Figure 1.1. So far, no experiments have caught excess of the CLFV events. The MEG experiment at the Paul Scherrer Institute (PSI) set the current best limit for $\mu \to e\gamma$ to be $BR < 4.2 \times 10^{-13}$ (90% C.L.) in 2016 [15]. An upgrade of the MEG experiment, the MEG II experiment, will start taking data to improve the current sensitivity by one order of magnitude. A series of the SINDRUM experiments, SINDRUM and SINDRUM-II, at the PSI gave the current limits for the branching ratios $BR\left(\mu \to eee\right) < 1.0 \times 10^{-12}$ (90% C.L.) in 1988 [16] and $BR\left(\mu^- + \mathrm{Au} \to \mathrm{e}^- + \mathrm{Au}\right) < 7.0 \times 10^{-13}$ (90% C.L.) in 2006 [17], respectively. The Mu3e experiment at the PSI will start to reach the upper limit of $BR\left(\mu \to eee\right) < 10^{-16}$. Two experiments will be performed to search for the $\mu \to e$ conversion. One is the COMET experiment described in Chapter 2. The other one is the Mu2e experiment at Fermilab [18].

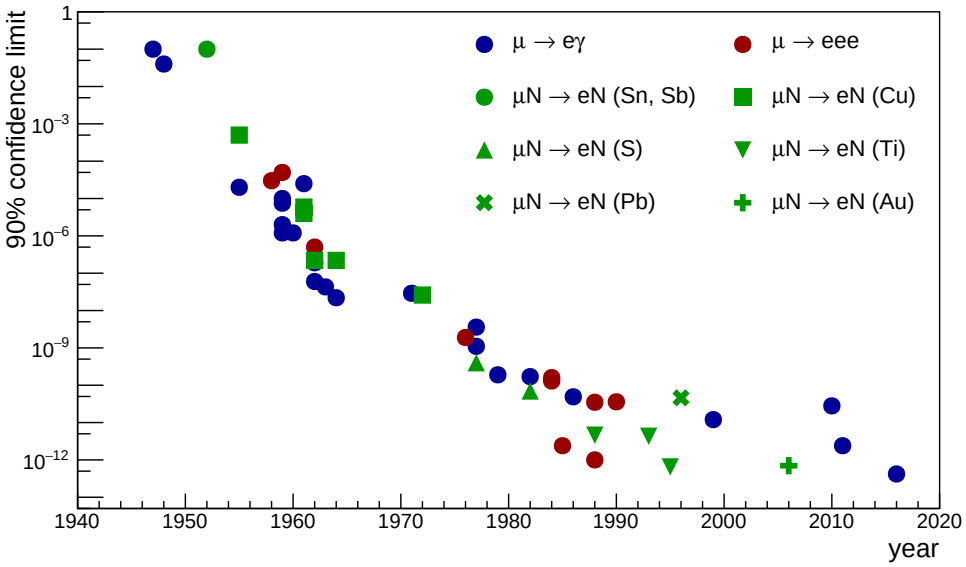

Figure 1.1: History of the charged lepton flavour violation searches [13, 14, 15].

1.4 Muon to electron conversion

The $\mu \to e$ conversion is a neutrino-less transition of a muon into an electron while the muon is electromagnetically bound to a nucleus. This process is represented by:

$$\mu^- + N(A, Z) \to e^- + N(A, Z), \tag{1.2}$$

where $N(A, Z)$ is the atomic nucleus with a mass number of A and a atomic number of Z. A muon, which is stopped in the matter, is bound by the atomic nucleus to form a muonic atom. The bound muon immediately cascades down to the 1s orbit and reaches the ground state while emitting X-rays, which are called muonic X-rays. Then, the muon goes to a three-body decay in the orbit or is captured by the nucleus in the SM. The former process releases an electron and two invisible neutrinos with the continuous electron energy spectrum. On the other hand, the latter process changes a proton to a neutron in the nucleus with neutrino emission. As in equation 1.2, the electron from the $\mu \to e$ conversion is emitted without changing the state of the atomic nucleus.

1.4.1 New physics beyond the Standard Model

The general relationship between the $\mu \to e$ conversion and other CLFV processes can be revealed in a model-independent analysis, e.g. an effective Lagrangian:

$$\mathcal{L} = \frac{1}{\kappa + 1} \frac{m_\mu}{\Lambda^2} \left(\bar{\mu_R} \sigma^{\mu\nu} e_L F_{\mu\nu}\right) + \frac{\kappa}{\kappa + 1} \frac{1}{\Lambda^2} \left(\bar{\mu_R} \gamma^\mu e_L\right) \left(\bar{q_L} \gamma_\mu q_L\right) + h.c. \tag{1.3}$$

The each parameters are summarised below:

L and R : the chirality of the fermion field,

$F^{\mu\nu}$: strength of the photon field,

m_μ : the muon mass,

Λ : an effective mass scale parameter of new physics, whose unit is mass-dimension of one, and

κ : a dimensionless parameter which indicates the relative size of two different terms.

The first term represents the photonic interaction, which directly mediates $\mu \to e\gamma$. In the $\mu \to e$ conversion, the virtual photon from the new physics process interacts with the nucleus; this interaction is suppressed stronger against $\mu \to e\gamma$. The second term represents the four-fermion interaction. In this term, the $\mu \to e$ conversion is mediated at the leading order, but on the other hand, $\mu \to e\gamma$ is mediated at the one-loop level. These relations affect the effective mass scale of the new physics for each process. For the relationship between the $\mu \to e\gamma$ process and the $\mu \to e$ conversion, Figure 1.2 illustrates the diagrams considered in the effective Lagrangian and the effective mass scale as a function of κ. The $\mu \to e\gamma$ process obviously contributes

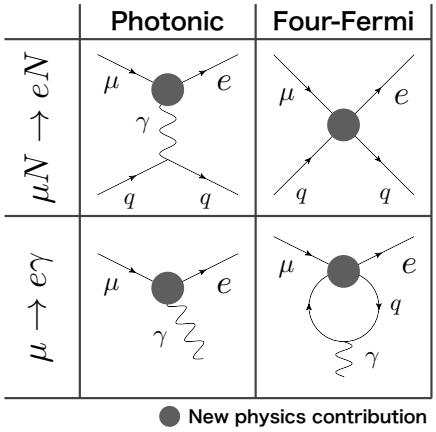

(a) Diagrams of the $\mu \to e\gamma$ and $\mu \to e$ conversion processes

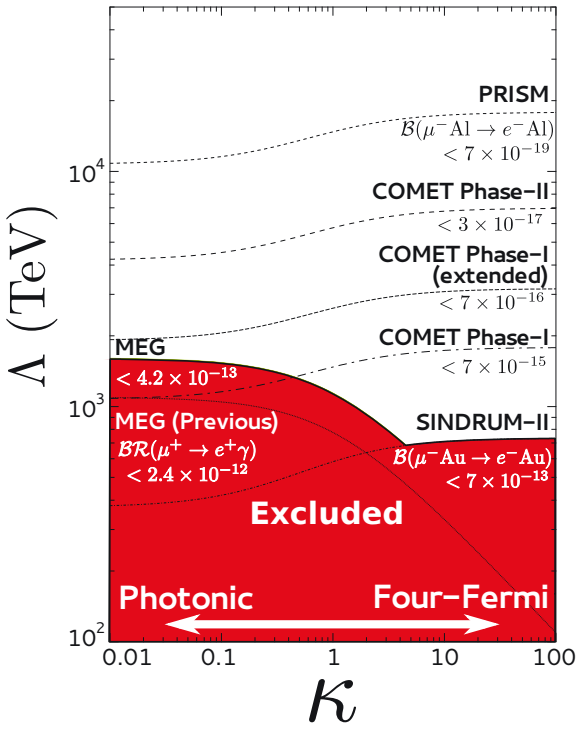

(b) Impact on the mass scale of new physics

Figure 1.2: Mass scale of new physics for each branching ratio of the muon rare decay. The diagrams show patterns of the $\mu \to e\gamma$ and $\mu \to e$ conversion processes mediated by new physics processes. The effective mass scale is described as a function of κ in Equation 1.3 [19].

to the photonic process more than the four-fermion process. On the other hand, the $\mu \to e$ conversion process shows a large contribution to both the photonic and four-fermion processes. This indicates that comparing experimental results between both processes constrain the new physics scale more precisely.

New physics models

Some candidates of new physics models predict the CLFV processes. In general, it can be assumed that the $\mu^- N \to e^- N$ process is driven by the following interaction terms in the new physics Lagrangian:

$$\mathcal{L}_1 \sim g^{\phi}_{e\mu} \bar{\mu} e \phi + g^{\phi}_{qq} \bar{q} q \phi, \tag{1.4}$$

$$\mathcal{L}_2 \sim h_{\mu\psi\phi} \bar{\mu} \psi \phi + h_{e\psi\phi} \bar{e} \psi \phi. \tag{1.5}$$

ϕ is a scalar or vector boson, which interacts fermions with a coupling constant of g^{ϕ}_{ff}. To induce the CLFV process, g^{ϕ}_{ff} must be non-diagonal for leptons. Then, a diagram of $\mu^- N \to e^- N$ process at the tree level is naturally drawn as shown in Figure 1.3. Some models indicate this type of CLFV process, such as models with

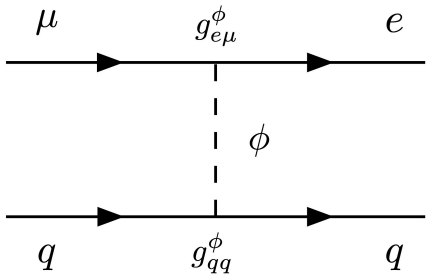

Figure 1.3: Diagram of the $\mu^- N \to e^- N$ conversion mediated by a new scalar boson (ϕ) at the tree level. ϕ couples to fermion with the coupling constant of g^{ϕ}_{ff}.

a massive neutrino, Z', and scalar or vector leptoquark models. For example, a new neutral gauge boson Z' can be introduced [20]. If Z' and the SM neutral gauge boson Z are the mass eigenstates of the $U(1)$ gauge boson, the CLFV processes are naturally induced by the off-diagonal elements.

A similar diagram at the tree level is expected by assuming the leptoquark models [21, 22]. In these models, the SM is extended by adding a scalar boson which couples to a quark and a lepton. The scalar boson can carry lepton flavour through interactions between a lepton and quark as drawn in Figure 1.4. Thus, CLFV processes are induced.

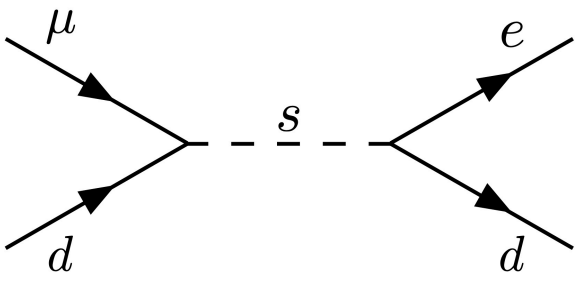

Figure 1.4: Diagram of the $\mu^- N \to e^- N$ conversion mediated by a scalar leptoquark (boson) at the tree level. The scalar boson s mediates an interaction between a fermion and a down quark in a nuleus.

In Equation 1.5, ψ refers to a new fermion, which carries lepton flavour. The interaction between ψ and ϕ carries lepton flavour while involving a lepton with a

coupling constant of $h_{l\psi\phi}$. $h_{l\psi\phi}$ must be non-diagonal as well as g^{ϕ}_{ff}. Figure 1.5 shows the possible diagrams induced by Equation (1.5). This interaction type is

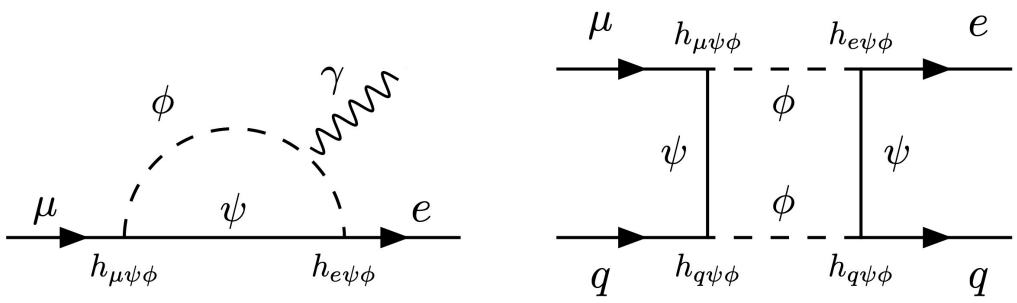

Figure 1.5: Diagrams of the photonic muon rare decay (left panel) and the $\mu^- N \to e^- N$ conversion (right panel) mediated by a new fermion (ψ) and a new scalar or vector boson (ϕ). ϕ and ψ couple to a fermion with the coupling constant of $h_{f\psi\phi}$.

also expected by some new physics candidates, such as models with sterile neutrinos and left-right symmetric models. As an example, the sterile neutrinos are strongly motivated to describe the neutrino mass generation and the neutrino oscillation anomalies in reactor/accelerator experiments [23]. In those models, a sterile neutrino can decay into a $W^{\pm}$ boson and a charged lepton by assuming its large mass. So, the CLFV process is induced via the sterile neutrino in the box and penguin diagrams.

As mentioned above, many candidates of new physics models predict the realisation of the CLFV process at detectable branching ratios. If a scheduled experiment dedicated to the CLFV search detects the processes, its branching ratio makes a big contribution to paring down the candidates by mixing with experimental results of the other physics channels. Furthermore, it points out a target energy scale for the direct measurements at high energy colliders. If CLFV is not detected in the experiments, their new upper limits of branching ratios strongly affect the energy scale of the new physics models.

1.4.2 Signal of the muon to electron conversion

The $\mu \to e$ conversion is characterised by the energy of the conversion electron. The conversion-electron energy $E_{\mu e}$ is calculated as:

$$E_{\mu e} = m_{\mu} - B_{\mu} - E_{rec}, \tag{1.6}$$

where m_{μ} is the muon mass, B_{μ} is the binding energy in the 1s orbit of the nucleus, and E_{rec} is the nuclear recoil energy. E_{rec} is given by $(m_{\mu} - B_{\mu})^2 / 2M_A$, where M_A is a nuclear mass, therefore, its contribution is less than the other terms.

Since the $\mu \to e$ conversion is characterised by the emission of that mono-energetic electron, a pulsed muon source is more appropriate for the detection than a DC muon source in order to suppress beam-related backgrounds. Then, the selection of a target material is important. The COMET and Mu2e experiments plan to use aluminium as the target, which has the relatively long lifetime of the muonic atom, 864 ns. $E_{\mu e}$ for aluminium is 105.0 MeV.

Chapter 2

The COMET experiment

This chapter is an overview of the COMET experiment.

2.1 COMET

The COMET experiment plans to search for the neutrinoless transition of a muon into an electron in an aluminium muonic atom. The experiment will take place in the Nuclear and Particle Physics Experimental Hall (NP Hall) at the Japan Proton Accelerator Research Complex (J-PARC) in Tokai, Japan [24, 25]. The ultimate goal of a single event sensitivity (SES) for the COMET experiment is 3×10^{-17} which is a factor of 10000 better than the current limit from the SINDRUM-II experiment [26]. A two-staged approach – Phase-I and Phase-II – is adopted to carry out the experiment. The purposes of Phase-I are to reach an SES of 3×10^{-15} and to understand features of the new muon beamline in preparation for Phase-II. In Phase-II, by raising the proton-beam power from Phase-I, we will search the $\mu \to e$ conversion with the ultimate sensitivity mentioned before.

Figure 2.1 illustrates the schematic layout of the COMET Phase-I experiment. The experimental facility is composed of three parts: the pion capture solenoid, the muon transport solenoid, and the detector solenoid. In the pion capture solenoid, a proton beam impinges a graphite target to produce a muon beam. The bent muon transport solenoid selects negative-charged and low momentum particles. Muons in the transported beam are stopped in aluminium target disks in the detector solenoid. Those muons decay into electrons or are captured by aluminium nuclei. A detector system surrounding the target disks detects the electrons from the muon decay.

2.1.1 Backgrounds

There are three types of background sources: intrinsic physics backgrounds, beam-related backgrounds, and cosmic-ray induced backgrounds. While the signature of the $\mu \to e$ conversion is the emission of a mono-energetic electron of 105 MeV from a muonic atom, these background sources could generate electrons in the energy region around 100 MeV.

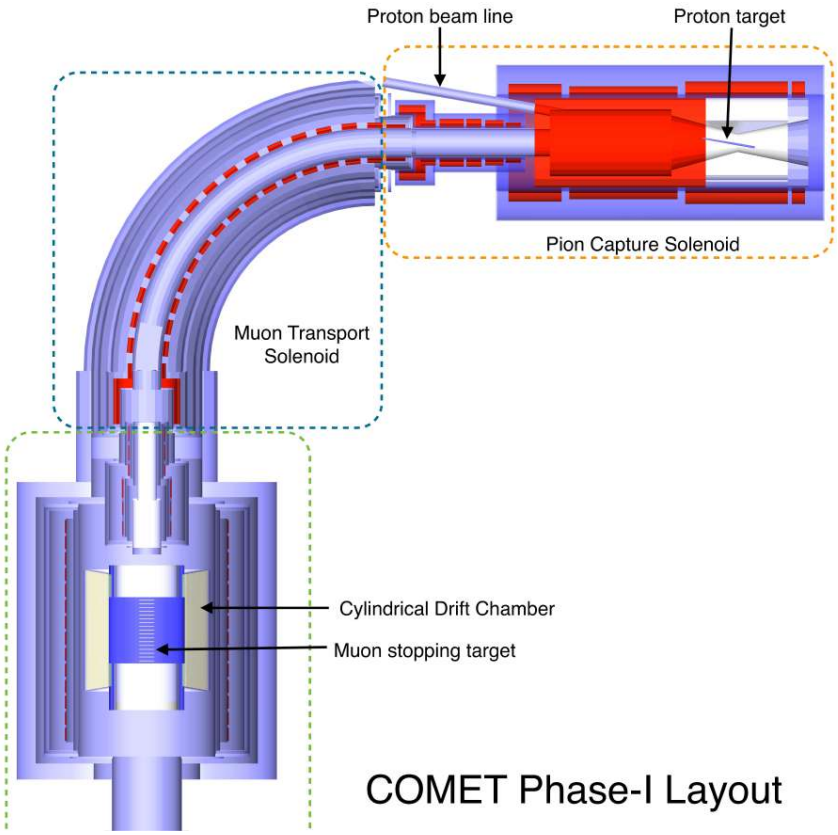

Figure 2.1: Schematic layout of the COMET Phase-I experiment [27].

Intrinsic physics background

Electrons from muon decays in muonic atoms generate the intrinsic physics background events. One of them is muon decay-in-orbit (DIO) where a muon decays into an electron and two neutrinos. In this decay, the electron energy can be larger than half of the muon mass due to the nuclear-recoil effect. The spectrum of the electron energy, $E_{\mu e}$, drops in proportional to $(m_\mu - B_\mu - E_{\mu e})^5$ near the spectrum end-point [28]. Thereby, the decay rate in the signal region is small enough for the experimental sensitivity. Figure 2.2 shows the energy spectrum of the DIO electron in the muonic atom formed in aluminium. To distinguish the conversion electrons

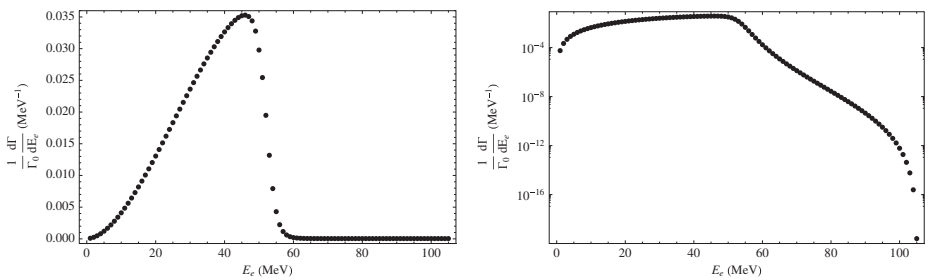

Figure 2.2: DIO electron spectrum for aluminium [28]. The left plot is linear scale, and the right plot is logarithmic scale.

from the DIO electrons, the momentum resolution of the detectors is required to be less than 200 keV/c for the 105 MeV/c electron for the Phase-I sensitivity. Figure 2.3 shows the expected momentum spectrum in the COMET Phase-I experiment, assuming that the detector resolution is 200 keV/c.

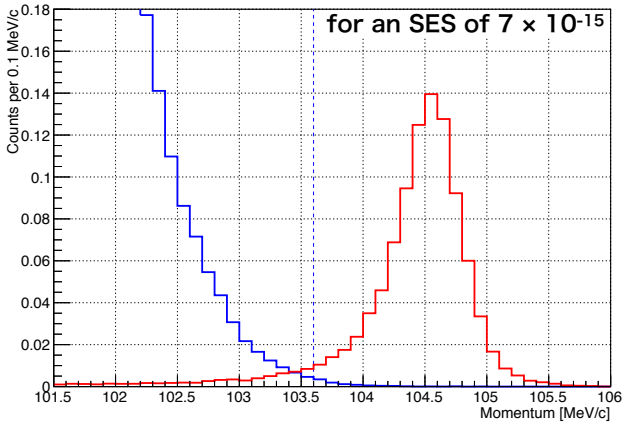

Figure 2.3: Expected momentum spectrum of $\mu \to e$ conversion and DIO electrons in the COMET Phase-I experiment [27]. The red and blue lines correspond to the momentum spectra of the $\mu \to e$ conversion and DIO electrons, respectively. On the right side of the blue dashed line, signals are contaminated with 1% of DIO events. The vertical axis is normalised by the area of the $\mu \to e$ conversion electron spectrum. The DIO-spectrum size is normalised by applying an SES of 7.0×10^{-15}.

Beam-related background

Pions, muons, electrons, and antiprotons in the muon beam are candidates of the beam-related background sources. The proton beam interacts with the graphite target and generates these particles in a wide momentum range. Pions potentially produce signal-like electrons by radiative pion capture (RPC)

$$\pi^- + N(A, Z) \to N(A, Z-1) + \gamma \tag{2.1}$$

and internal/external e^+e^- conversion of

$$\gamma \to e^+ + e^-. \tag{2.2}$$

Muons whose momenta are greater than 77 MeV/c can create signal-like electrons by muon decay in flight in a beam. Electrons emitted by decays of π^0s that are produced at the proton target are mixed into the transported beam and scattered off the target disks. If the energy of those electrons is close to the signal energy region, they have to be taken into account. When proton energy is higher than 5.6 GeV, antiprotons can be produced by proton-nuclear reactions. If these antiprotons are stopped in material and captured by the nucleus, they release huge energy and often generate pions by proton-antiproton annihilation. As mentioned above, the pions may produce background events.

Cosmic-ray induced background

Cosmic-ray muons can generate 105-MeV electrons from decays or interactions with surrounding materials in the detector region. Also, 105-MeV muons can be misidentified as electrons.

2.1.2 Requirements

In order to carry out the COMET Phase-I experiment, the requirements for the proton-beam source, the muon-beam section, and the detector system are:

- the proton-beam source
  - the proton beam needs to be pulsed for the use of a delayed time window of the measurement (measurement window) and the reduction of the beam-related backgrounds, and
  - the number of leakage protons should be as small as possible because they can produce the beam-related backgrounds between the beam pulses.
- the muon-beam section
  - the highly-intense muon beam needs to be produced to reach the sensitivity goal, and
  - the muon transport section needs to select low momentum and negatively charged particles.
- the detector system
  - the momentum resolution needs to be less than 200 keV/c for the 105-MeV electron and
  - the detector system needs to detect cosmic rays to veto their events.

2.2 Muon beamline

2.2.1 Proton beam

In the COMET Phase-I experiment, an 8 GeV, 3.2 kW proton beam is extracted from the J-PARC Main Ring (MR) to produce the highly intense muon beam. Figure 2.4 shows an overview of the J-PARC facilities. Firstly, protons are accelerated to 400 MeV by LINAC. Secondly, the Rapid Cycling Synchrotron (RCS) accelerates them to 3 GeV in one out of two buckets. Finally, the protons are injected into the MR by kicker magnets. In order not to kick any particles remaining in empty buckets, the excitation timing of the injection kicker is shifted forward by 600 ns. This injection method, called single bunch kicking, is a critical aspect for COMET Phase-I to reduce the number of leakage protons. There are nine bunches in the MR, and only four bunches are filled with the protons from the RCS. Then, a bunch is separated from others by at least 1.17 μs. The MR can accelerate the proton beam up to 30 GeV. In COMET Phase-I, an 8-GeV proton beam operation is adopted to keep a low production rate of antiprotons [27].

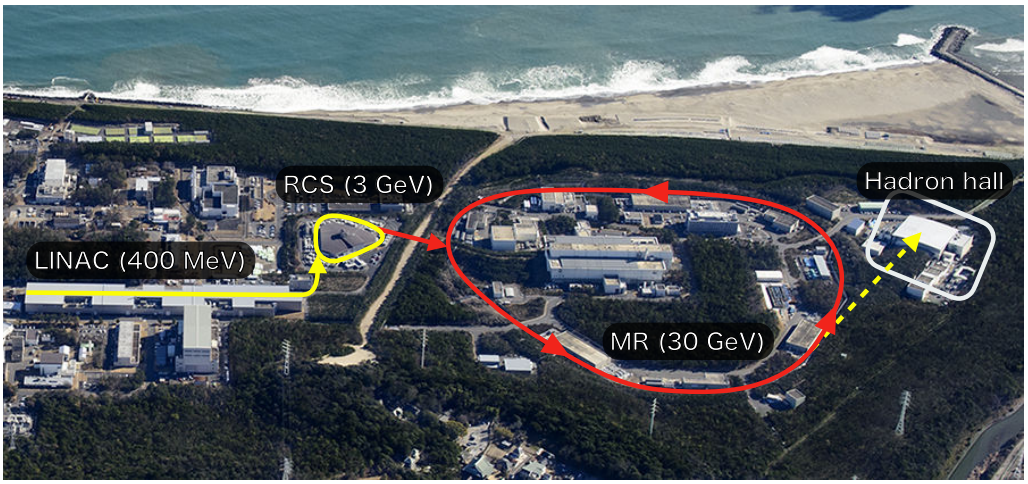

Figure 2.4: J-PARC Centre [24].

The protons in the MR are led to the COMET experimental area in the NP Hall via the B-line. The B-line is being constructed. Not only the COMET experiment but also other hadron experiments plan to use the B-line. The other beamline (A-line) is in operation, and these beamlines will be switched at the switchyard between the MR and the Hadron Hall. The overview of the beamlines is shown in Figure 2.5.

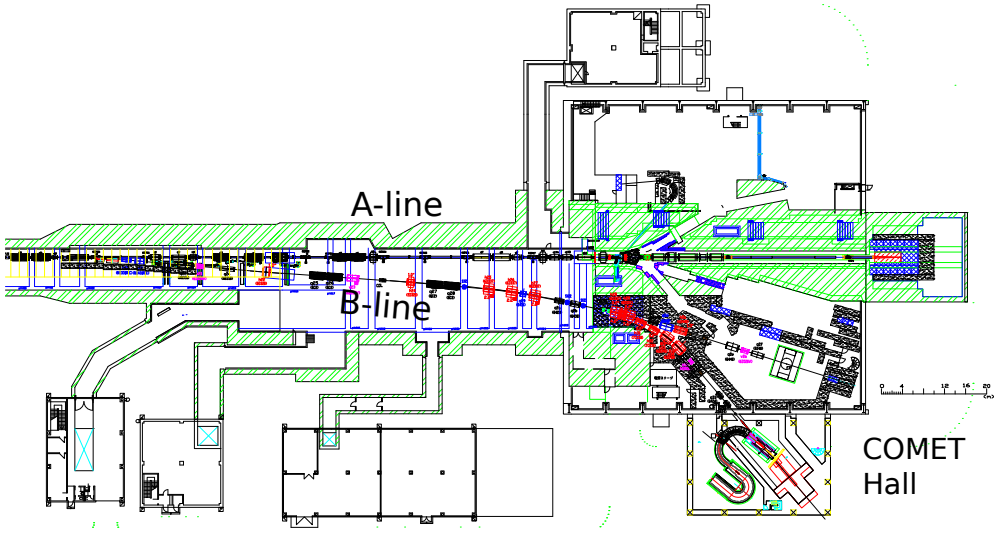

Figure 2.5: Layout of the Hadron Hall [27]. The A and B-lines come from the MR and go to the NP Hall.

The bunched 8-GeV proton beams in the MR are slowly extracted, called bunched slow extraction, and led to the COMET experimental area. The normal slow extraction technique is applied for the 30-GeV proton beam injection into the NP Hall while an RF voltage, which keeps a bunched beam structure in the MR is turned off. On the other hand, the RF voltage needs to be maintained to keep the clear bunched structure during the bunched slow extraction. The use of the higher RF voltage induces a lower number of the leakage protons. However, it makes the heat

load higher on the RF cavity. Thanks to the water-cooling system, an RF voltage of 255 kV could be achieved in the accelerator test. The proton beam extinction factor, $R_{\text{extinction}}$, is used to evaluate the performance of the slow extraction and is given by:

$$R_{\text{extinction}} = \frac{N\,(\text{leakage protons})}{N\,(\,\text{protons per bunch})}. \tag{2.3}$$

By applying the RF voltage of 255 kV, the extinction factor is managed to be as low as 10^{-12}. Then, the beam-related background is estimated to be small enough for the target sensitivity. Figure 2.6 shows the schematic of the beam timing.

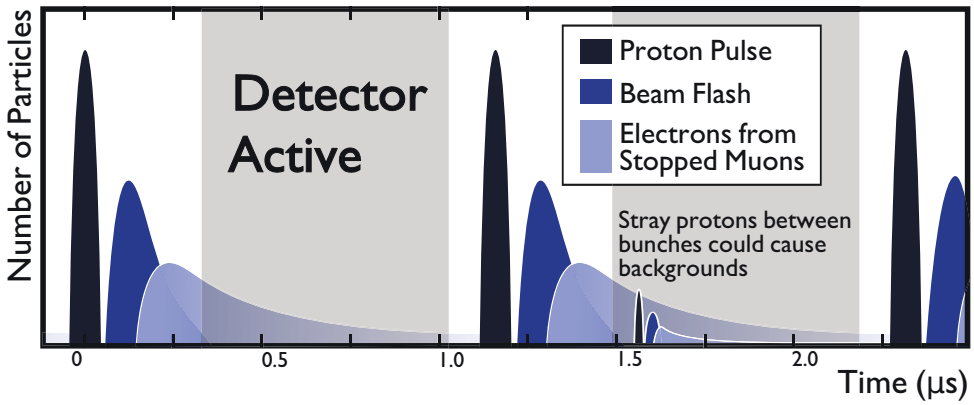

Figure 2.6: Timing structure of the bunched-beam int the COMET Phase-I experiment [19].

2.2.2 Muon beam

Muons and pions are transported to the muon stopping target through the curved solenoid. The muon transport section is required to:

- be long enough for the pion decays and
- efficiently select muons with low momentum to eliminate the background from muon decays in flight.

In the COMET Phase-I experiment, the curved solenoid is tuned to select around 40 MeV/c muons and eliminate muons with a momentum of higher than 75 MeV/c.

The electric charge and momenta of the transported particles are selected in the curved solenoid. The trajectory of a charged particle is helical in the solenoidal magnetic field, and its central axis drifts in the direction perpendicular to the plane of curvature. The magnitude of this drift, D, is given by:

$$D = \frac{1}{qB}\frac{s}{R}\frac{2p_{\parallel}^2 + p_{\perp}^2}{2p_{\parallel}}, \tag{2.4}$$

where q is the electric charge of the particle, B is the magnetic field strength, s is the flight length, R is the radius of curvature of the curved solenoid, $p_{\parallel}$ is the longitudinal momentum, and $p_{\perp}$ is the transverse momentum. The dipole field of about 50 mT

is applied to compensate for the drift distance of trajectories of negatively charged particles from the centre of the beam pipe. Positively-charged particles drift in the opposite direction of negatively-charged particles; a collimator sits at the end of the transport solenoid to cut the positively-charged particles. After these selections, the muon beam goes to the muon stopping target in the detector solenoid.

2.3 Detector

The conversion electrons from the $\mu \to e$ conversion are detected by a cylindrical detector system (CyDet), which consists of a cylindrical drift chamber (CDC) and a cylindrical trigger hodoscope (CTH). The CyDet is installed inside a warm bore of the detector solenoid providing a 1-T magnetic field. Figure 2.7 shows a schematic layout of the CyDet.

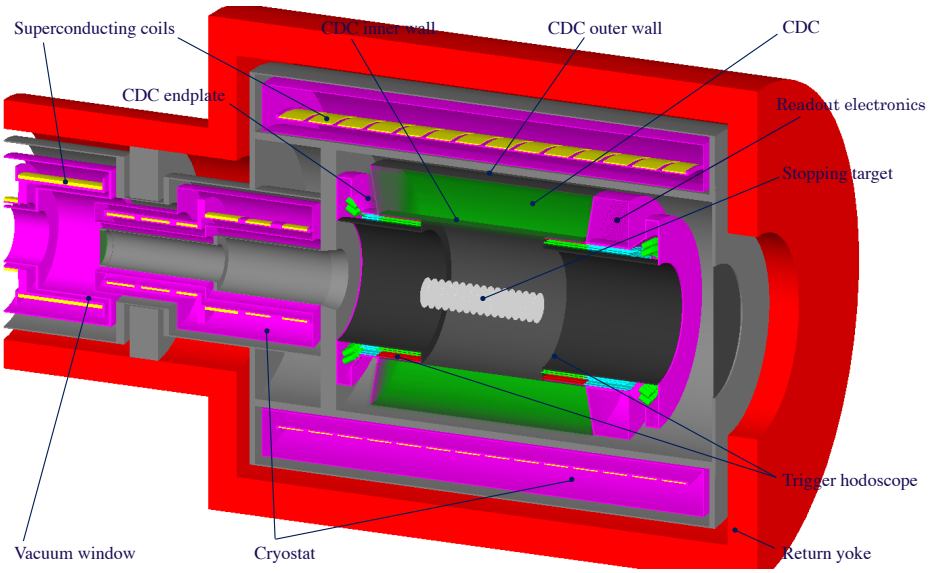

Figure 2.7: Schematic layout of the CyDet [27].

2.3.1 Cylindrical Drift Chamber

The CDC reconstructs helical tracks of charged particles in the magnetic field and accurately measures particle momenta. The main parameters of the CDC are summarised in Table 2.1. The inner and outer walls are made from carbon fibre reinforced plastic (CFRP) of 0.5 mm and 5 mm thickness, respectively. The thickness of the inner wall is determined in order for particles not to lose their energies. The CDC inner wall is designed with a large diameter of about 1.0 m so that beam particles and low-energy DIO electrons hardly reach inside the CDC. The DIO electrons of less than around 70 MeV/c are not accepted, and it can effectively reduce the event rate of the main background. An outer-wall diameter of about 1.7 m makes the acceptance of the CDC large enough to detect electrons from the $\mu \to e$ conversion. In the CDC, 4,986 sense wires and 14,562 field wires are strung in total. An alternated all stereo layer configuration is adapted for all the wires to measure track positions in the longitudinal direction parallel to the CDC axis. The stereo

angles are set to achieve a longitudinal spatial resolution of about 3 mm. The momentum resolution is significantly affected by the multiple scattering effects when a low-energy electron, such as the converted electron, is tracked. Therefore, the material density in the CDC is as small as possible to reduce the multiple scattering effects, and the chamber gas is selected to be He−iC_4H_{10} whose radiation length is 1310 m.

Table 2.1: Main parameters of the CDC.

Inner wall	Material	CFRP
	Length	1495.5 mm
	Radius	496.0-496.5 mm
	Thickness	0.5 mm
Number of sense layers		20 (including two guard layers)
Outer wall	Material	CFRP
	Length	1577.3 mm
	Radius	835.0-840.0 mm
	Thickness	5.0 mm
Sense wire	Material	Au-plated W
	Diameter	25 μm
	Number of wires	4986
	Tension	50 g
Field wire	Material	Al
	Diameter	126 μm
	Number of wires	14562
	Tension	80 g
Gas	Mixture	He−iC_4H_{10} (90:10)
	Volume	2084 L

Drift chamber

A CDC cell is composed of one sense wire and eight field wires that are placed around this sense wire. A high voltage is applied to the sense wire to produce an electric field. On the other hand, the field wires are connected to the ground level to isolate the cell from others.

In a CDC cell, a charged particle ionises the gas and produces primary electrons. Some of those primary electrons acquiring high energy ionise neighbouring atoms, and secondary electrons are produced close to the track of the charged particle. Both primary and secondary electrons move toward a sense wire while being accelerated by the electric field. Near the sense wire, those electrons provide an avalanche amplification, which exponentially increases the number of ionised electrons. Then, the flow of electrons induces a current on the sense wire, and that induced current becomes detectable with readout electronics.

The time from the primary-electron production to the current induction is called "drift time", and the distance between a particle trajectory and a sense wire is called "drift distance". The performance of the drift chamber is characterised by the relationship between the drift time and the drift distance.

CDC readout electronics

To detect the induced current, the readout electronics for the central drift chamber of the Belle II detector (RECBE) [29] are customised and adopted as the COMET CDC readout electronics. The RECBE reads electrical signals from the CDC and measures the signal timing and the total charge. This signal timing includes the drift time and the timing when a charged particle passes through a CDC cell. The amount of charge is proportional to the energy deposition of a charged particle in a CDC cell. The RECBE builds event data from this information and sends it to a data acquisition system.

Figure 2.8 is a picture of the RECBE board. This board has six amplifier shaper

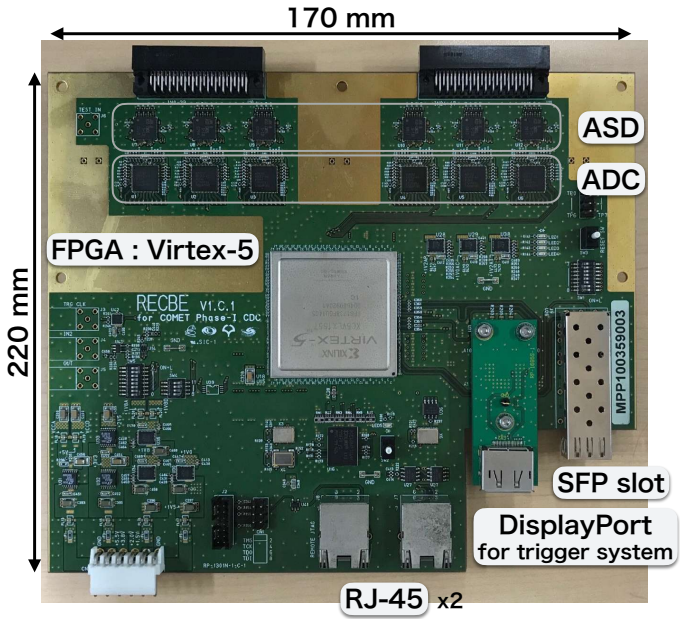

Figure 2.8: Photograph of the RECBE board.

discriminator (ASD) chips, six analog-to-digital converters (ADC) (AD9212ABCPZ-40, Analog Device [30]) chips, a digital-to-analog converter (DAC) (LTC2630ACSC6-HZ12, Linear Technology [31]) chip, a field programmable gate array (FPGA, Virtex5, xc5vlx155t, Xilinx Inc. [32]), two 1.27-mm pitch multi-function two-piece connectors (FX2-52P-1.27DS(71), Hirose Electric Co Ltd), an SFP port, two RJ-45 sockets, and a MEG-Array connector (84512, Amphenol FCI [33]). This board has 48 readout channels; 104 RECBEs are used to read out data from all 4986 CDC wires. The configuration of the RECBEs is shown in Figure 2.9.

ASD, ADC and DAC 8-channel ASD and ADC are adopted. On the RECBE, there are six ASD and ADC chips; it receives signals from up to 48 channels. This ASD is an application-specific integrated circuit (ASIC) developed by the Belle II group and outputs two signals: an analogue signal and a digital signal. Further details are provided in Appendix **??**. A threshold for the digital output is adjusted by using the FPGA through the DAC on the RECBE. The analogue and digital outputs are sent to the ADC and FPGA, respectively. The ADC digitalises this analogue output into a 10-bit value at 30 MSPS and sends it to the FPGA.

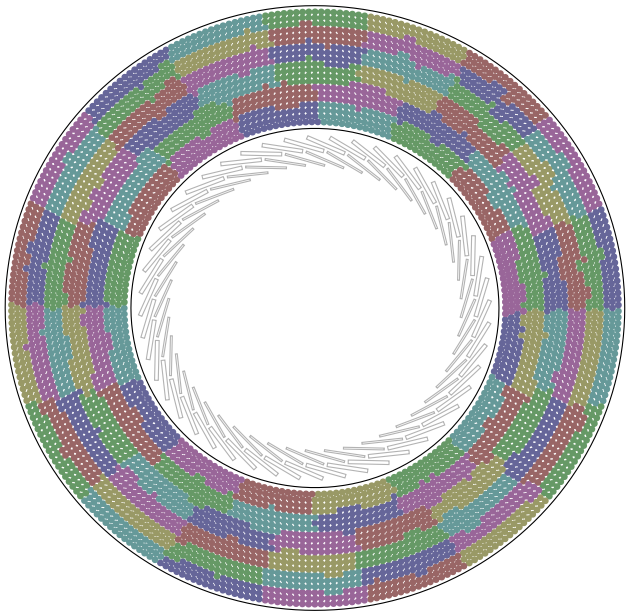

Figure 2.9: Configuration of the RECBE boards. Each dot is a CDC wire. The CDC wires are grouped by RECBE, and each colour section corresponds to a RECBE board.

FPGA The circuit structure of the FPGA is designed by firmware, which is written in a hardware description language. The firmware for the FPGA on the RECBE is composed of modules for each application. Some of them are newly added and modified for the CyDet from the original version for the Belle II CDC. Figure 2.10 illustrates the block diagram of the modules. The most significant task is event data

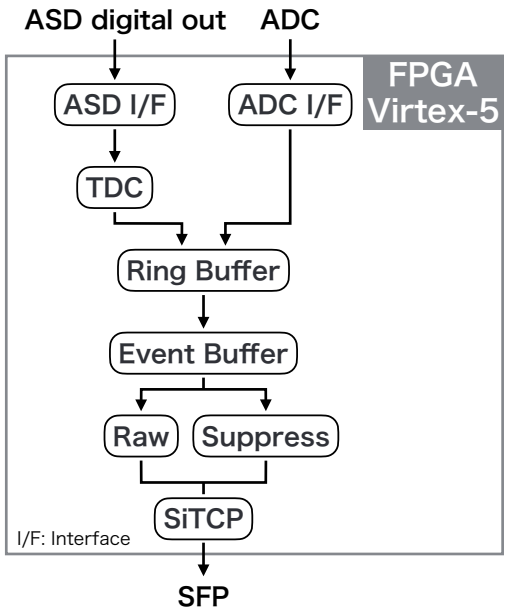

Figure 2.10: Block diagram of modules in the RECBE firmware.

production by using the digital data from the ASD and ADC. The FPGA receives a shared clock of 40 MHz and a trigger signal through one of the RJ-45 sockets.

The shared clock is converted to a 120 MHz system clock for the main system and a 240 MHz clock for the measurement of hit timing. A clock module divides the system clock by four to make a 30 MHz clock for the ADCs. A time-to-digital converter (TDC) module measures the timing of the digital signal from the ASD using a multi-sampling technique. In this technique, the phase of the 240 MHz clock is shifted by 90 degrees, and four clock lines with different phases are prepared. By making use of these four clocks, the performance of the TDC module is equivalent to one at 960 MHz; the time information is divided into a minimum time bin of 1.04 ns. Both waveform and hit timing data are stored in ring buffers with the 30-MHz clock period. 32 samples of the timing information can be generated within a period of the ADC sampling clock of 30 MHz, but only data of the first hit is stored. The ring buffer has 256 addresses. It, therefore, keeps the data for 8.5 μs. An address number in the ring buffer corresponds to the timing in the event window of readout data. The event window is long enough to catch the hits in the drift-time range. The firmware has two data transfer modes for data acquisition (DAQ); raw and suppress modes. The raw mode includes 32 ADC and TDC samples of each channel for a 1.07 μs event window, and it enables waveform analysis. In the suppress mode, ADC samples over a baseline are summed by channel in the event window, and only the ADC sum is transmitted. For the timing information, at most two TDC samples having smaller values are packed in the event data. The raw mode is used in debug runs, and the suppress mode is used in the physics measurement. For more information of the data format, see Appendix A.1.3.

The firmware also includes registers that control setting and monitor status. The following parameters are adjustable by using the registers: the data mode, the event window, the process latency, the ADC baseline for each channel, the threshold of the ASD digital output.

Connectors and Sockets Two 1.27-mm pitch multi-function two-piece connectors connect all the ASD input pins. The right RJ-45 socket in Figure 2.8 is to:

- receive the clock signal and the trigger data from the central trigger system, and
- send the busy signal to the central trigger system.

On the other hand, the left RJ-45 socket is to download the firmware to Virtex-5. These sockets are connected with the FCT RECBE interface board through Ethernet cables, as described in Section 2.4.1. The SFP port works for the communication between Virtex-5 and the DAQ network with SiTCP [34]. SiTCP enables both UDP and TCP/IP communications. UDP communication is applied for setting and reading register values, and TCP/IP communication is applied for data acquisition. An HFBR-7934 connector connects with transceivers on the FPGA. This is attached to an adopter and used for the online trigger system, as described in Chapter 3. These components are summarised in Table 2.2.

Requirements The spatial resolution of the CDC is required to be less than 200 μm to meet the required momentum resolution of less than 200 keV/c for the electron from the $\mu \to e$ conversion. In order not to affect the spatial resolution adversely, the time resolution of the RECBE is required to be less than 1 ns.

Table 2.2: Summary table of the connectors and sockets on the RECBE.

Name	Target	Comment
Multi-function two piece connectors	CDC	Recieving the CDC signal
RJ-45	FCT interface	(In) Clock and trigger, (Out) Busy signal Firmware download
SFP	DAQ PC	Data acquisition
HFBR-7934		Online trigger

The RECBEs are placed on the CDC endplate at the downstream side to suppress electrical noise, as shown in Figure 2.7. According to a simulation study, this region becomes a high radiation environment; all devices have to be tolerable against both total dosage of 1.0 kGy and 1 MeV equivalent neutron fluence of 1.0×10^{12} neutron/cm^2 including a safety factor of five during the 150-day physics measurement. RECBE must be able to work in the 1-T magnetic field. It has been confirmed that the performance of the RECBE has met with the requirements from the previous studies [35, 36, 37].

2.3.2 CyDet Trigger Hodoscope

The CTH detects large-β (fast) charged particles, such as electrons, with a good time resolution and provides the trigger signals for the CyDet.

Many protons are emitted from radiative muon capture processes and detected in the CDC. Even though the energy deposition of protons is much larger than that of electrons in the CDC, the CTH should separate the conversion electrons from protons for the trigger rate reduction. For a similar reason, cosmic-ray muons need to be ignored too. The time resolution of CTH has to be better than the CDC and is required to be less than 1 ns since the trigger detector starts a timer to measure the timing of each hit in the CDC. To this end, this detector consists of 48 sets of Cherenkov and scintillation counters, and these counters are arranged in a ring shape. In order not to scatter particles going to the CDC, the detector ring is located at not the middle region but both upstream and downstream inner ends of the CDC; the CTH detects particles that come out of the CDC.

The Cherenkov counters are adopted to detect only large-β (fast) charged particles. When a charged particle passes through them faster than the speed of light in counter's material, Cherenkov radiation occurs. This relationship is given by:

$$\begin{aligned} \beta \equiv \frac{v}{c} &> \frac{1}{n} \\ \Leftrightarrow \quad v &> \frac{c}{n} \end{aligned} \tag{2.5}$$

where v is the velocity of an incident particle, c is the speed of light, and n is the refraction factor of counter's material. The problem is that alone this counter does not produce enough light to achieve the required time resolution. This problem is compensated by the scintillation counter, which produces a large amount of light. The molecules in the scintillator are excited by the electromagnetic interaction with incident charged particles, and some of them emit visible light. By mixing fluorescent

materials, ultraviolet (UV) rays from excited molecules are converted to detectable wavelengths. Doing this gives a large amount of light, and the rise time of the scintillator becomes less than 1 ns.

A hit coincidence of both Cherenkov and scintillation counters is applied to detect the desired particles. Then, background electrons are carefully considered because they could be detected by using both counters at the same time. These electrons are contained in the muon beam or at detector frames converted from gamma-rays, which are converted from the beam electron or emitted from radiative muon-/pion-/neutron-capture processes. For providing a trigger signal, a four-fold coincidence method, two sets of Cherenkov and scintillator rings, is adopted to greatly reduce the triggers induced by the backgrounds, as shown in Figure 2.11. The majority

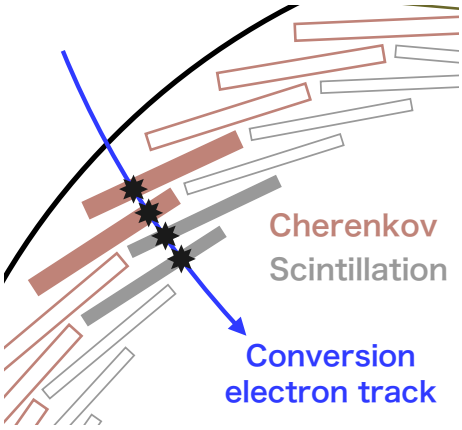

Figure 2.11: Image of the CTH four-fold coincidence for the conversion electron.

of the background electrons generated by gamma rays have an energy lower than 20 MeV, and these electrons in a 1-T magnetic field describe circular trajectories with small radii of less than 7 cm. Since the CTH counters are arranged with large overlapped areas, applying the four-fold coincidence efficiently reduces the trigger rate while maintaining the signal acceptance of the CTH.

The Cherenkov counter is 300 mm × 110 mm × 10 mm UV-transparent acrylic plastic. The scintillation counter is 300 mm × 110 mm × 5 mm polyvinyl-toluene-based scintillator (ELJEN EJ-230) [38]. The Cherenkov counter is thicker than the scintillation counter to increase the larger amount of light. The refractive index of this plastic is 1.5, and the threshold value of the β is 0.67. This scintillator has a rise time of 0.5 ns and decay time of 1.5 ns.

Photosensors are applied to detect both Cherenkov light and scintillation light. There are three requirements for the photosensors:

- a large amplification factor,
- neutron tolerance to 1 MeV equivalent neutron fluence of $1.0 \times 10^{12}\,\mathrm{cm}^{-2}$, and
- magnetic-field tolerance to 1 T.

For the first requirement, the signal-noise ratio (S/N) is required to be larger than 20 to distinguish signals from noise hits clearly. The amplification factor of the photosensor needs to be large enough for both this S/N and the required time resolution. For the second requirement, it is known that some semiconductor-type photosensors

are easily broken by irradiation of neutrons. In the COMET Phase-I experiment, the collision between the 3.2 kW proton beam and the graphite target results in a high radiation environment. According to a simulation study, the photosensor has to survive after the neutron irradiation of $1.0 \times 10^{12}\,\mathrm{cm}^{-2}$ including a safety factor of five. The photosensor must be able to operate in the 1-T magnetic field because the CTH is located inside the detector solenoid. These requirements are met using a fine-mesh photo-multiplier tube (PMT). The fine-mesh PMT does not have any semiconductor sensor, and its fine-mesh dynode has enough magnetic-field tolerance. In the 1-T magnetic field, the gain of the fine-mesh PMT is decreased to 2.5% of the design value, but it is still enough for photon detection. A Hamamatsu H8409-70 PMT, which has a high gain of 1.0×10^7 is adopted as the photosensor of the CTH. This PMT is operated with a pre-amplification board to recover the reduced amplification.

2.3.3 Others

The cosmic-ray muon can generate a background event when hitting the detector or transport section. Therefore, a cosmic-ray veto (CRV) system is set to tag all events with timing when cosmic-rays pass through the active region. This system is composed of scintillation counters and fully covers the sides and top of the detector solenoid. The detection efficiency is estimated to be more than 99.99%.

The number of muons stopped by the aluminium target must be counted to calculate the single event sensitivity of the COMET Phase-I experiment. Muons captured by the aluminium nuclei emit X-rays, called muonic X-rays, transiting from one state to another. The number of stopped muons is given by:

$$N_\mu = \frac{F_{i\to j}}{A_{i\to j} \times \Omega \times \epsilon} \tag{2.6}$$

where i and j are states of the muonic atom; $F_{i\to j}$ is the number of counts in energy peak of the muonic X-ray from state transition of the muonic atom; $A_{i\to j}$ is the state transition probability of the muonic atom; Ω is the solid angle of X-ray measurement; ϵ is the detection efficiency for X-ray. Table 2.3 shows the relative intensity and the energy of the muonic X-rays in each transition type for aluminium atoms. In the COMET Phase-I experiment, a Germanium detector, which is an X-ray detector, is installed on the beam axis and downstream of the detector solenoid to measure the muonic X-rays from the aluminium target.

Table 2.3: Relative intensity of the muonic X-rays from the aluminium target.

Transition	Energy [keV]	Relative intensity [%]
2p $\to$ 1s	346.828 ± 0.002	79.8 ± 0.8
3d $\to$ 2p	66.11 ± 0.02	67.6 ± 1.7
3p $\to$ 1s	412.87 ± 0.05	7.62 ± 0.15
4p $\to$ 1s	435.96 ± 0.10	4.87 ± 0.10

2.4 Trigger and DAQ

The electronic signals from the detectors are processed and recorded by solid systems for trigger and DAQ. All components in the trigger system need to work stably and synchronously while sharing a clock signal. This system also needs to control the trigger rate in order not to miss the event data in the DAQ system. When the trigger rate is over the capability of each component in both trigger and DAQ systems, it is easy to fail the event reconstruction. The trigger and DAQ system is shown in Figure 2.12.

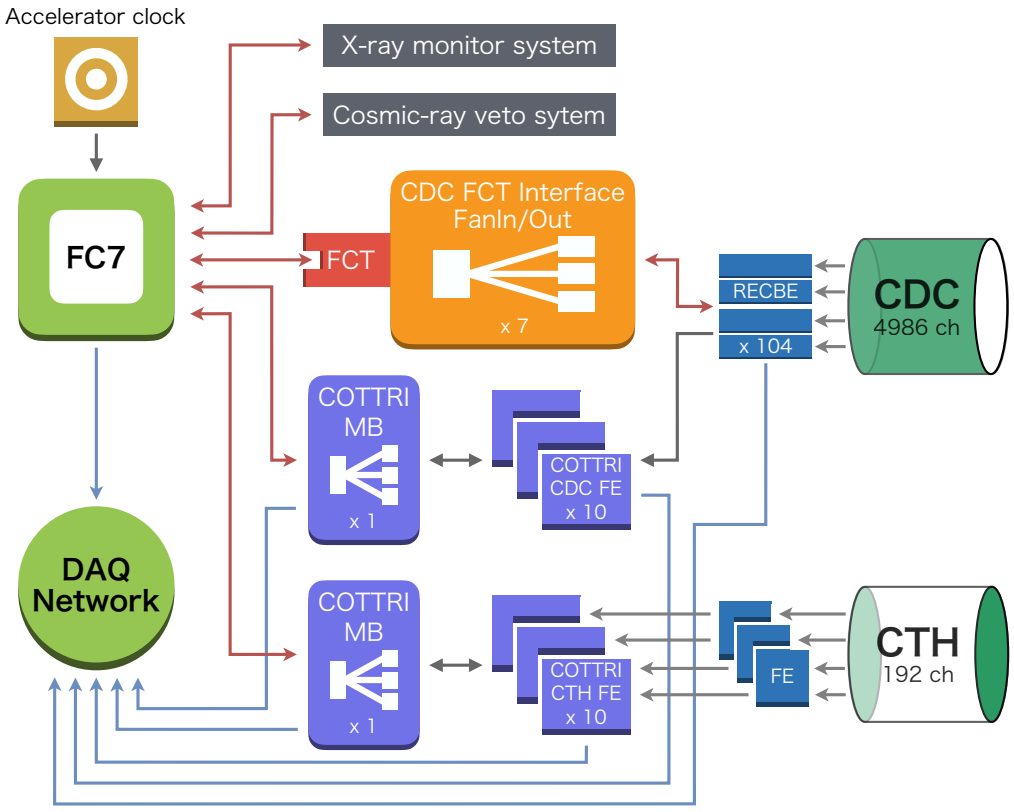

Figure 2.12: Block diagram of the whole trigger system. The green box is the central board in the trigger system. The orange and red boxes are electronics related to fast control. The blue boxes are the front-end electronics for the detectors. The purple boxes are the electronics for the online-trigger generation.

2.4.1 Trigger system

The trigger system mainly consists of the FC7, the FCT, the COTTRI system, and the front-end electronics for the detectors. Each trigger-related board has an FPGA to perform digital data processing such as reading and acquiring data from the detector.

FC7

The FC7 is developed by the Compact Muon Solenoid (CMS) group in the European Organization for Nuclear Research (CERN) [39]. This is the master board in the

trigger system and responsible for four tasks: the final trigger decision, distribution of trigger signals, synchronization of all the electronics, and online monitor for the beamline. The trigger signal from the FC7 is treated as one of the data for fast control.

The data of the detectors including the CRV and X-ray monitor systems are sent to the FC7. The FC7 makes the trigger decision by using the event-condition data and produces a trigger number for offline event matching.

The data acquisition timing not only for the FC7 but for other boards is controlled by applying the trigger. The FC7, therefore, distributes the trigger signal and number to the front-end electronics. By attaching two commercial mezzanine cards, the FC7 communicates with up to 16 trigger-related electronics through multi-gigabit transceivers (MGT). The mezzanine card has eight sockets of small form-factor pluggable plus (SFP+) transceivers and connects with others by utilizing SFP+ transceivers and optical fibres. A protocol, called the MGT link, for the COMET experiment was developed by customizing the Aurora 8B/10B protocol provided by Xilinx [40]. The data transfer rate is 4.8 Gbps with a reference clock of 120 MHz. The reference clock is created by using a sine wave of 12 MHz from the J-PARC accelerator, which is synchronizing with the acceleration timing. The fast-control data format is different between outgoing and incoming data. The output fast-control data is composed of fast-control commands of 14 bits, the trigger event number of 32 bits, FCT control data of 32 bits, FCT control command of 4 bits, and unused space of 2 bits. The input fast-control data is composed of status flags of 4 bits, FCT status data of 16 bits, and trigger data of 64 bits. The MGT link continuously transfers 96 bits within 3 clock cycle, these 84 bits data, an 8 bits comma, and two 2 bits packet identifiers. Thus, the trigger data is transmitted at 40 MHz.

As mentioned above, the process timing of each circuit board must be synchronised to guarantee the simultaneity of data from all the boards. The FC7 stably communicates with other electronics at this trigger-data rate, and then those electronics can reconstruct a 40 MHz clock from the header timing of the trigger data. This clock is used for the timing synchronization in the CyDet trigger system.

Since the measurement window is related to the timing of the beam bunch, the FC7 has to monitor the beamline condition.

Fast Control and Trigger

A fast control and trigger (FCT) board is developed for the COMET experiment to take the role of an interface between the FC7 and each detector readout board by attaching an interface board. The FCT board receives the shared clock and the fast-control data from the FC7 over the MGT link with an SFP+ transceiver and an optical cable. In the original design for the CyDet, the FCT board sends the shared clock and the trigger number to the RECBE and receives the busy signal from RECBEs through the FCT RECBE interface board with 16 registered jack 45 (RJ-45) sockets attached.

The trigger number in the fast-control data is converted to a serial data stream at the timing of the shared clock. Both the shared clock and this data stream of the trigger number are sent to the front-end readout boards. Since the FC7 needs to know the status of the trigger-related boards, the FCT board collects busy signals from the readout boards and sends them to the FC7.

One FCT board communicates with up to 16 readout boards through one FCT interface board. The FCT board connects with the FCT interface board by using an FPGA mezzanine card (FMC) connector. The interface board is produced for each detector front-end electronics. So, it has connectors that match the ones in those electronics. With this design concept, the same firmware of an FPGA (Kintex-7, xc7k160t, Xilinx Inc. [41]) on the FCT board is used for all the electronics. This firmware has an operation mode for each detector readout board, and it is changed by a dual in-line package (DIP) switch on the FCT board.

COTTRI system

Before the final trigger decision in the FC7, the CDC and CTH trigger signals are generated from the data of the CDC and the CTH, respectively. Those processes are carried out in a COMET trigger (COTTRI) system. The COTTRI system consists of two COTTRI merger-boards (MBs), COTTRI CDC front-end boards (FEs), and COTTRI CTH FEs. The same COTTRI MB board is individually used for the processes of the CDC and CTH triggers. The COTTRI CTH FE directly reads data from the CTH photon sensors through the pre-amplification boards, and therefore it has ADCs. It also measures CTH hit timing by using digital signals from the pre-amplification boards. The COTTRI MB for the CTH trigger collects all the CTH hit information from the COTTRI CTH FEs and makes the trigger decision with the coincidence of the CTH hits. The CDC trigger is applied to reduce the trigger rate more by using the CDC hit information. The COTTRI CDC FEs receive compressed information about CDC hits from the RECBEs and pass it to the COTTRI MB. The COTTRI MB makes the CDC trigger decision and sends the trigger signal to the FC7. The details of the COTTRI system for the CDC are described in Chapter 3.

2.4.2 DAQ

The design of the DAQ network is shown in Figure 2.13. The DAQ network needs to process data from over 150 front-end readout devices; the two-layer configuration is adopted for event building. The first layer consists of 1G/10G optical network switches and front-end PCs. The second layer consists of an event building PC with peripheral component interconnect express (PCIe) cards attached, an online analysis PC, and a disk array. The COMET DAQ software is based on a maximum integrated data acquisition system (MIDAS), which is developed at the PSI [42].

Front-end layer

One front-end PC handles about twenty front-end devices through a 1G/10G optical network switch; the network switch connects with the front-end PC and each front-end device at 10 Gbps and 1 Gbps, respectively. The front-end PC converts data from the front-end devices into the MIDAS data format so that it is easy to carry out event building on the back-end layer. The converted data is sent to the event building PC on a 10 Gbps optical line.

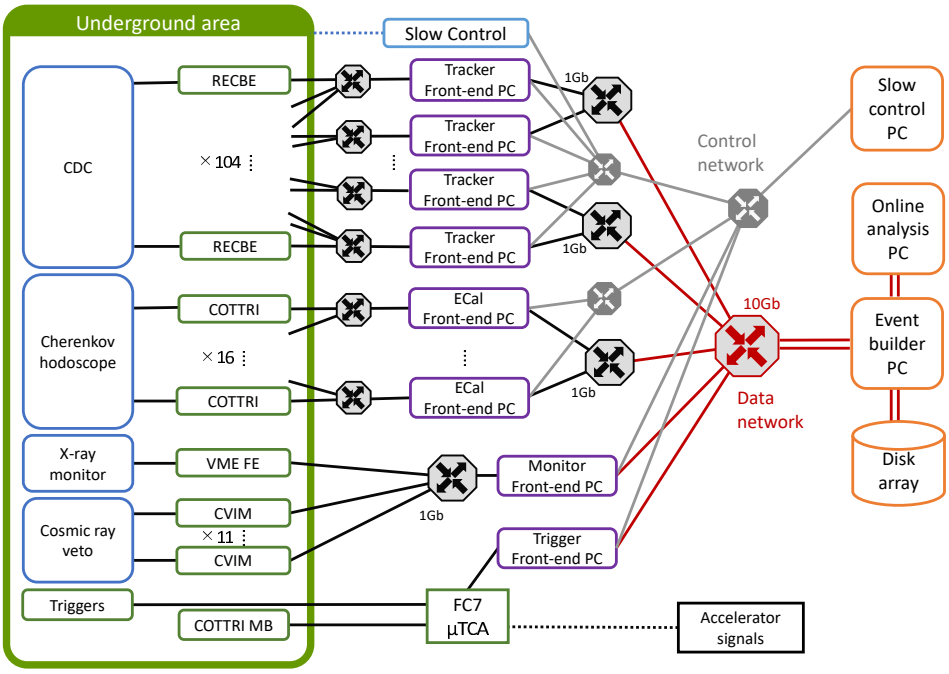

Figure 2.13: Block diagram of the COMET data acquisition system [27].

Back-end layer

A 2U server PC is used as the event building PC that collects all the data in the CyDet system. This PC has three or four high-speed PCIe slots. Each PCIe slot has eight lanes, and therefore a PCIe slot connects with up to four front-end PCs. The maximum transfer rate is about 7.877 GB/s for two lanes (two-way), which is faster than the output rate of the front-end PC. Thus, the event building PC handles up to 12 or 14 front-end PCs; it can operate over 240 front-end devices. After receiving data, the event building PC generates event data and sends it to both the online analysis PC and the disk array. The online analysis PC randomly picks up events from all the data and draws online event displays. The disk array stores all event data for offline analysis.

Expected trigger rate tolerance

The maximum data size of the suppress mode of RECBE is 492 Byte, which consists of a 12 Byte header and 480 Byte channel data. The data size of other devices is not fixed yet, but CDC data size is expected to be larger than half the total data size. According to a simulation study, the CDC hit occupancy in the event window of 1 μs is expected to be around 40%. The entire DAQ throughput is 1 GiB/s due to the use of an event building PC. These values conclude that the CyDet trigger system can stably take data at about 26 kHz.

2.5 Current issue

The highly intense muon beam is indispensable to achieve the sensitivity goal, and it leaves a lot of hits in the CyDet; the expected trigger rate is too high for the

DAQ system. According to a simulation study, the hit rate of each CTH counter is $\mathcal{O}(10^7)$ Hz. Even after the four-fold coincidence, the trigger rate is expected to be over 90 kHz, as discussed in Section 6.5. This rate is still too high for the DAQ system. Besides, this expected value is calculated in the simulation without parameters measured by using the components of the COMET Phase-I because the COMET facility is under construction. It means that the simulation data could have non-negligible uncertainty. From the beam measurement at J-PARC, it is empirically known that the number of protons fluctuates around twice bunch-by-bunch. For the above reasons, the trigger rate must be much lower than the required trigger rate of 26 kHz. To this end, we have two ideas. One is of adding the event building PC to make the entire DAQ throughput higher. The other one is of developing a new trigger system to reduce the trigger rate further. Since the target event containing the conversion electron has never been observed with the branching ratio of 7.0×10^{-13} (90% C.L.) yet, the triggered events are mostly worthless. Those worthless events press data storage and make wasted time in offline analysis. We have selected the latter idea and developed a fast online trigger system using CDC-hit information. This thesis reports the first study of the online trigger efficiency in the COMET Phase-I experiment.

The physics motivation of the $\mu \to e$ conversion search and the COMET Phase-I experiment are introduced in Chapter 1 and this chapter, respectively. To describe the fast online trigger system, this thesis has the following structure:

Chapter 3: the algorithm of the COTTRI system

Chapter 4: the development of the electronics related to the COTTRI system

Chapter 5: the operation test of the COTTRI system using one-sixth of the CDC readout region in a setup of the cosmic-ray measurement

Chapter 6: the simulation study of the COMET Phase-I experiment and estimating the CTH trigger rate

Chapter 7: the detector response simulation to reproduce the digital data processed in the COTTRI system

Chapter 8: estimating the performance of the COTTRI system in the physics measurement

Chapter 9: the discussion about the signal acceptance of the online trigger system and remaining works towards the physics measurement

Chapter 10: the conclusion of this thesis

Chapter 3

FPGA-based fast online trigger system

The online event classification algorithm is implemented in the COTTRI system for the CDC. Together with the RECBEs, the COTTRI system that consists of two FPGA-based electronics works for the trigger rate reduction in this system. This chapter describes the algorithm of the CDC COTTRI system.

3.1 Concept

As discussed in Section 2.5, the CTH trigger rate is not acceptable for the COMET DAQ system. The highly intense muon beam creates a lot of undesirable particles in the detector solenoid or directly interacts with materials on the CTH. DIO electrons that are the intrinsic physics background may leave trajectories similar to the conversion-electron trajectory in the CDC, and offline track reconstruction is required to distinguish them from each other. However, its trigger rate is expected to around 200 Hz. It is difficult for the CTH to eliminate fake trigger events originated by low-energy electrons. In most cases, such a fake trigger is not correlated with the CDC-hit timing. Therefore, the use of the CDC-hit information would help to reduce the trigger rate. To this end, an FPGA-based fast online trigger system using the CDC hit information has been newly developed. The COTTRI system would suppress the trigger rate with the information from the CTH and the CDC.

The DAQ trigger rate is required to be down to 13 kHz with a safety factor of two. It is satisfied with the entire trigger system, whose processing time of the trigger system is limited to be less than 7 μs due to the buffering time of the RECBE.

3.2 Classification concept

The COTTRI system performs online signal-track recognition using gradient boosted decision trees (GBDT) [43], which is one of the ML methods. To separate the signal events from the background events on the online trigger system, two classification stages are adopted: hit classification and event classification, as illustrated in Figure 3.1. GBDTs work for the hit classification in the form of look-up tables (LUTs).

Keys for the classifications are differences of hit and track characteristics between

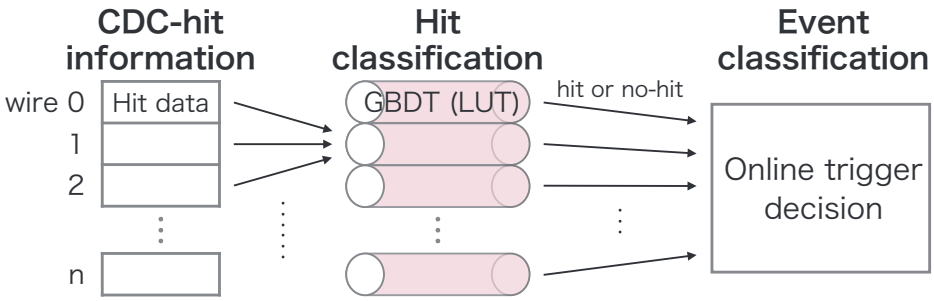

Figure 3.1: Conceptual design of the COTTRI system.

the conversion electron and backgrounds. Figure 3.2 shows a simulated CDC-hit map of a conversion-electron event. In the 1-T magnetic field, trajectories of the

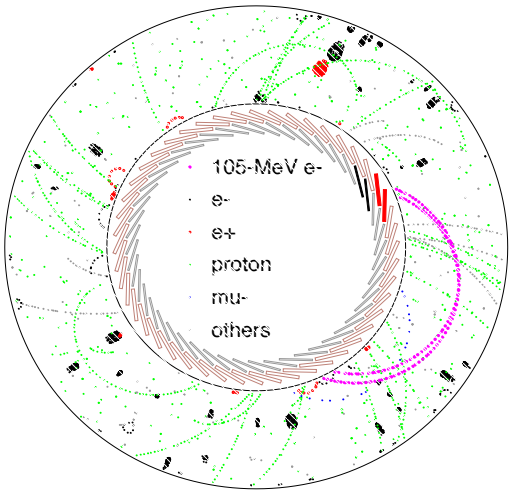

Figure 3.2: Simulated CDC-hit map containing the conversion-electron track. Each dot shows a position where a charged particle loses energy. All the CDC hits in a bunch are drawn. The "others" are heavy particles, such as alpha, triton, and heavy ions.

conversion-electrons are helical with large radii. The radius of the CDC outer wall is determined to fully contain them in the CDC. It may result in making the following characteristics of the CDC hit:

- continuous hits in the same CDC layer,
- difficulty of reaching the outer layers,
- single hit in the same wire, and
- MIP-level energy loss.

The main backgrounds are low-energy electrons from the gamma-ray interactions at the CDC walls and protons from the muon-nuclear-capture processes. The low-energy electrons pass along the wires, and their trajectories are helical with a small radius, resulting in multiple hits on the same wire. The protons mostly have high

momenta and pass through the CDC from inside to outside. Furthermore, they lose more energy than the conversion electrons. The low-energy protons scattered by neutrons move a bit and make hits isolated from other hits. In short, characteristics of the background hits are:

- multiple hits (low-energy electron),
- larger energy loss (proton), and
- an isolated hit (low-energy proton).

The role of the hit classification is to evaluate whether a hit on each wire is signal-like by using GBDTs. Before the GBDT-based evaluation, the CDC wires having multiple hits in a short time are filtered to eliminate hits of the low-energy electrons. The GBDTs give larger output values for the signal-like hits, and these hits are selected for the event classification. Figure 3.3 shows images of the CyDet event display before and after applying the GBDTs. From the characteristic differences

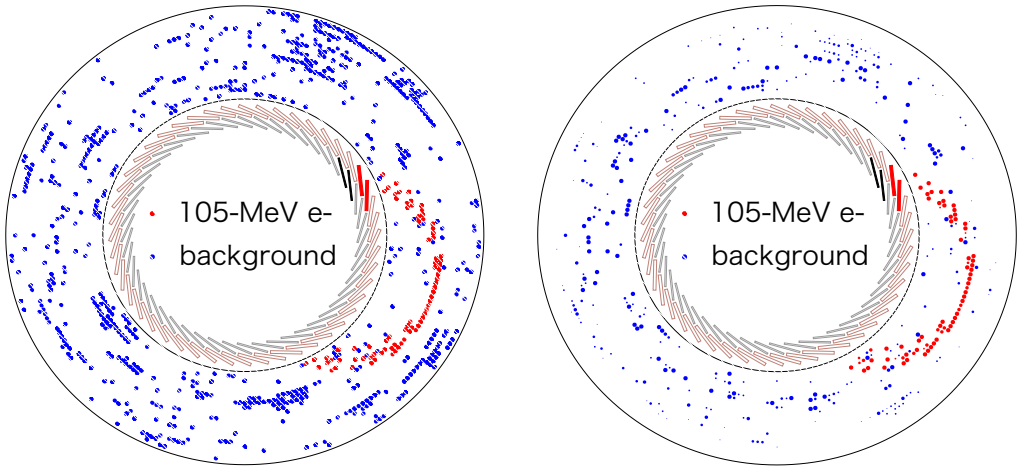

(a) before applying the LUTs (b) after applying the LUTs

Figure 3.3: Simulated event displays within 400 ns in the CyDet (a) before and (b) after applying the GBDTs. Each dot shows a hit-wire position on the CDC endplate in the readout side. In the panel (b), the GBDT outputs are visualised with dot size.

mentioned above, the energy loss on the wire of interest (local wire) and its radial position are selected as the GBDT-input features. The radial position is represented as the CDC-layer identification (ID). The input features include the energy loss on both the left and right neighbors of the local wire in the same layer. The relationship between the local and neighbouring wires is represented in Figure 3.4. The required input features for the GBDTs are summarised in Table 3.1.

In the event classification, the COTTRI system makes the trigger decision using both the CDC and CDC trigger information. The conversion electron leaves hits not in the entire CDC readout area but in a part of this area that is correlated with the CTH-hit positions, as shown in Figure 3.3. An active part of the CDC is defined for each CTH counter to cut background hits. When the number of the signal-like hits in each active part exceeds a threshold, the CDC trigger is generated for each CTH counter. The CTH trigger gives which counters ring after the four-fold coincidence.

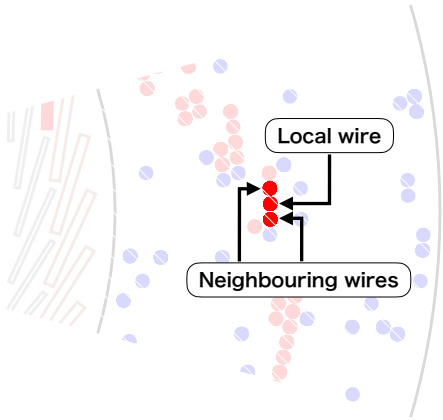

Figure 3.4: Relationship between the local and neighbouring wires.

Table 3.1: Required input features for the GBDTs.

Deposited energy on the local wire
Deposited energy on the neighbouring wire (left)
Deposited energy on the neighbouring wire (right)
Layer ID of the wires

The final trigger decision is performed by taking coincidence between these CDC and CTH triggers. Figure 3.5 illustrates those procedures.

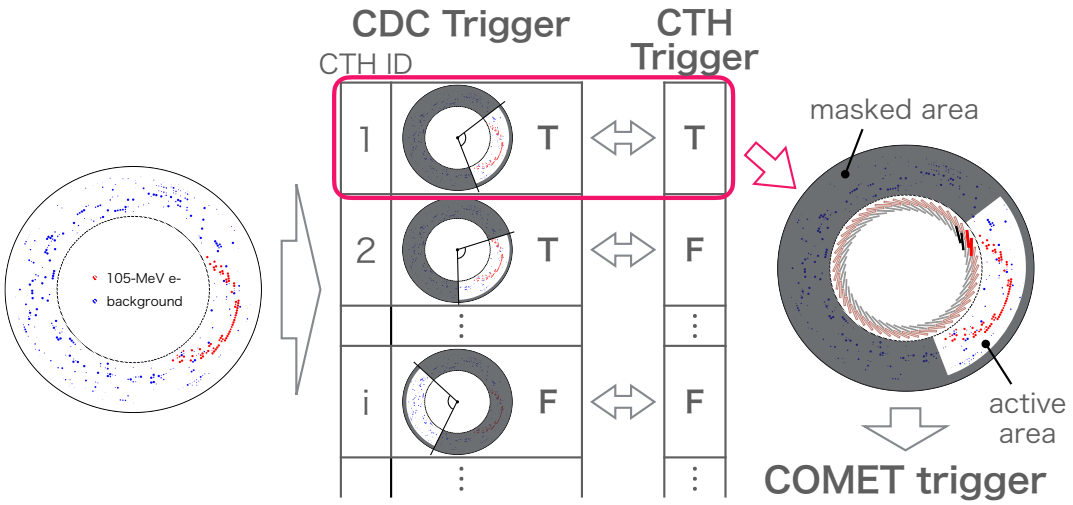

Figure 3.5: Image of the procedures in the event classification. In the tables, "T" (true) and "F" (false) show trigger and non-trigger for each CTH counter, respectively.

3.3 Distributed trigger decision system

The CDC COTTRI system consists of two types of electronics: ten COTTRI CDC Front-end boards (hereinafter, this is called "COTTRI FE") on the first layer and

one COTTRI Merger-board (COTTRI MB) on the second layer. Thus, it becomes a distributed trigger system and controls data for over 4000 CDC channels. The trigger-decision process is asynchronous with the proton bunch and is performed in pipeline.

3.3.1 Layout of the COTTRI system

Figure 3.6 illustrates the layout of the COTTRI system. A COTTRI FE receives

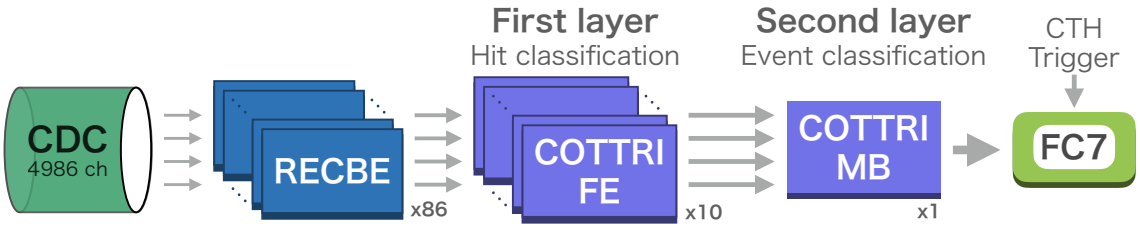

Figure 3.6: Layout of the COTTRI system.

CDC-hit information from ten RECBEs at most and sends the hit-classification score of each RECBE to the COTTRI MB. Using that, the COTTRI MB makes a trigger decision and sends the CDC trigger to the FC7. According to the simulation study mentioned in Chapter 8, the RECBEs on the outer layers have a much smaller contribution to the event classification than the RECBEs on inner layers. Therefore, 18 RECBEs on the outermost board layer do not participate in the COTTRI system. It means that three outer layers of CDC wires including the guard layer are not considered. The configuration of the RECBEs for each COTTRI FE is shown in Figure 3.7.

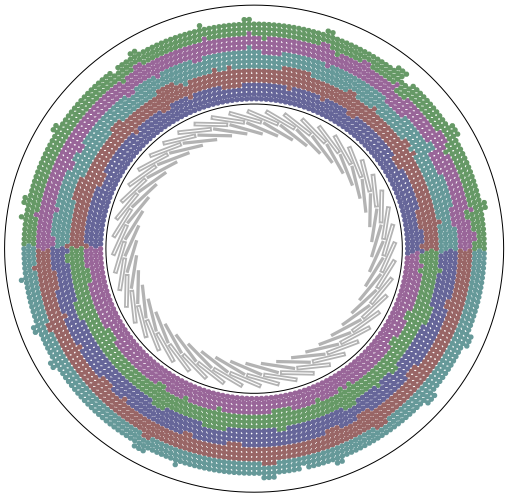

Figure 3.7: Configuration of the RECBE boards for each COTTRI FE. Each dot is a CDC wire. Each colour section corresponds to the readout region for a COTTRI FE.

3.3.2 Process for the trigger decision

When the trigger algorithm is implemented on electronics, constraints of their resource and performance have to be considered carefully. In the case of the COTTRI system, the data size of the GBDT-input feature is limited and has been decided by the size of the LUT. The use of built-in 6-input LUTs on the FPGA was adopted to efficiently consume the FPGA resource. Then, the inputs of these LUTs were decided to be the 2-bit energy-loss information on the local wire and two neighbouring wires in the CDC. The radial-position dependence of the GBDT outputs is expressed by defining the LUTs by wire.

A flowchart of data processing for the COTTRI trigger system is illustrated in Figure 3.8.

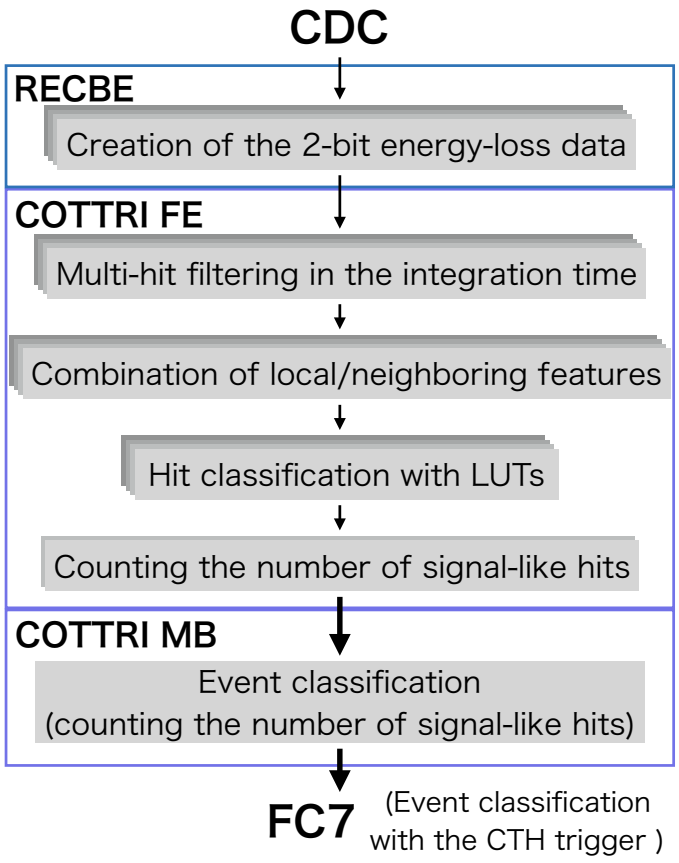

Figure 3.8: Flowchart of data processing for the COTTRI trigger decision.

Pre-process of each hit information

In order to perform the hit classification in the COTTRI FE, the RECBEs create the 2-bit energy-loss data from the CDC-hit information. The data transfer rate between the RECBE and the COTTRI FE is also limited due to the FPGA performance. So, to create the 2-bit data, three ADC samples that are taken at 30 MSPS are integrated, and its sampling rate becomes 10 MSPS.

Hit classification

After that, the 2-bit data is sent to the COTTRI FE. Here, multiple hits in an integration time are first filtered, as illustrated in Figure 3.9. This integration time

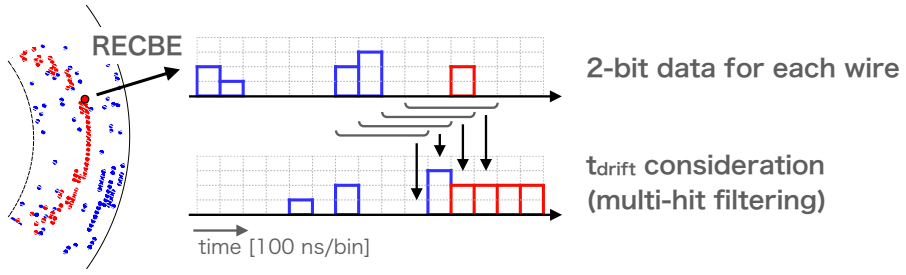

Figure 3.9: Image of multi-hit filtering in the integration time (t_{drift}). The red points and boxes show data of the conversion electron. The blue points and boxes shows data of backgrounds.

is applied for considering the drift time in the CDC cell. The input of the LUT is formed in the combination of the local and neighbouring features. As referring to the LUT, the input for each wire is converted to the output, which is a score representing signal-like. Figure 3.10 illustrates this process. The score is used to

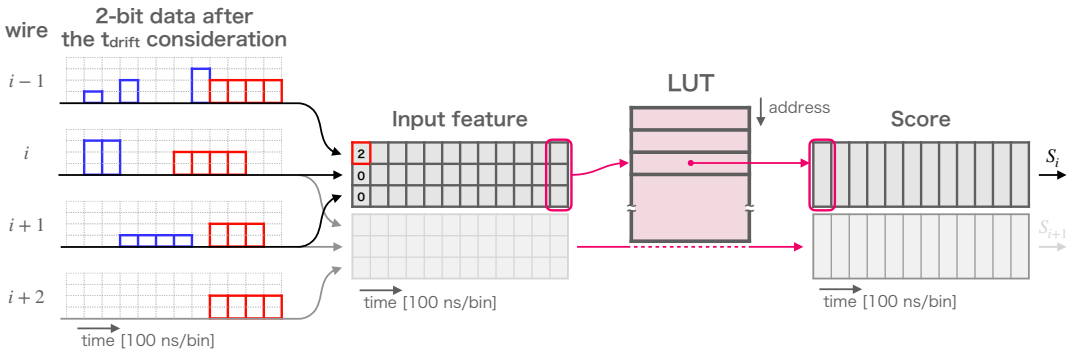

Figure 3.10: Image of the hit classification by LUTs. i is the wire ID, and S is a score. In the 2-bit data histogram, the red and blue lines show hits of the conversion-electron and backgrounds, respectively.

classify hits as signal or background with a threshold. The number of signal-like hits is counted for each RECBE and sent to the COTTRI MB, as illustrated in Figure 3.10.

Event classification

The CDC active section for each CTH module is defined with a readout section of one RECBE as a unit. The COTTRI MB receives the number of signal-like hits for all the RECBEs and sums it up in each active section. By applying a threshold for the summation, the CDC-trigger decision is performed for each CTH module. The CDC-trigger signals are sent to the FC7. Finally, taking a coincidence between the CDC and CTH triggers executes the final trigger decision.

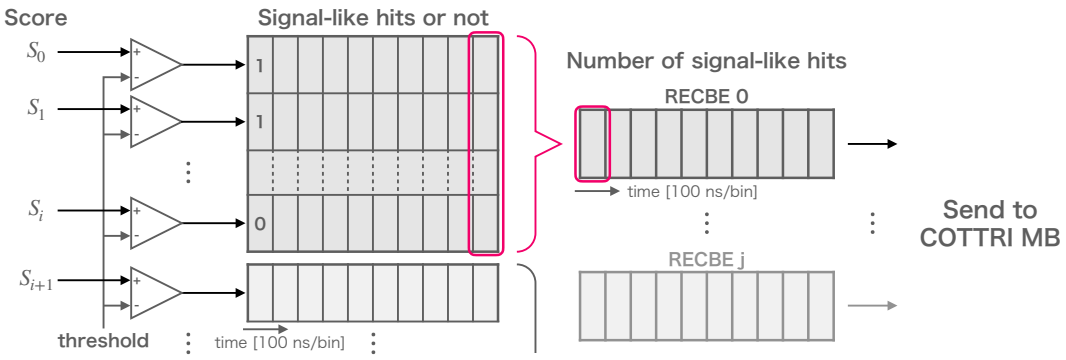

Figure 3.11: Image of counting the number of signal-like hits in the hit classification. i is the wire ID, j is the RECBE ID, and S is a score. In this case, the wire IDs of 0 to i are on RECBE 0.

Chapter 4

Hardware

Electronics have been developed to implement the trigger algorithm introduced in Chapter 3. This chapter describes the detailed hardware configuration of the CDC COTTRI system.

4.1 RECBE

Since the CDC-hit information joins the COTTRI system, functions of the RECBE were expanded. New modules in the firmware and a new adapter board (see Appendix A.1.2) have been developed.

4.1.1 Firmware

In the firmware, the two modules work for the COTTRI system, as shown in Figure 4.1: a 2-bit data generator and a communication protocol. In the 2-bit data

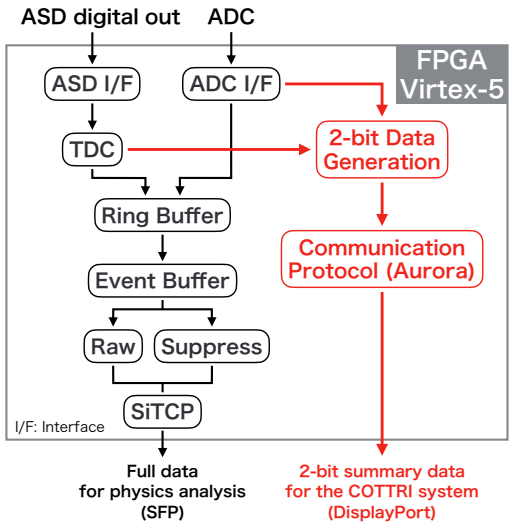

Figure 4.1: Block diagram of the RECBE firmware. The red boxes represent the additional modules.

generator, three continuous samples of ADC are integrated to produce a waveform

sample at 10 MHz for each channel. The integrated ADC value (ADC-sum) is converted to 2-bit data by using three threshold values (Threshold-1, 2, and 3) and the digital output of ASD (Hit-flag). The Hit-flag is asserted when an input signal level exceeds the threshold of the comparator on the ASD chip. The relationships among them are:

- 2'b00: (Hit-flag = Low) || (ADC-sum < Threshold-1)
- 2'b01: (Hit-flag = High) && (Threshold-1 ≤ ADC-sum ≤ Threshold-2)
- 2'b10: (Hit-flag = High) && (Threshold-2 < ADC-sum ≤ Threshold-3)
- 2'b11: (Hit-flag = High) && (Threshold-3 < ADC-sum)

Figure 4.2 draws this conversion process. The communication protocol sends the 2-

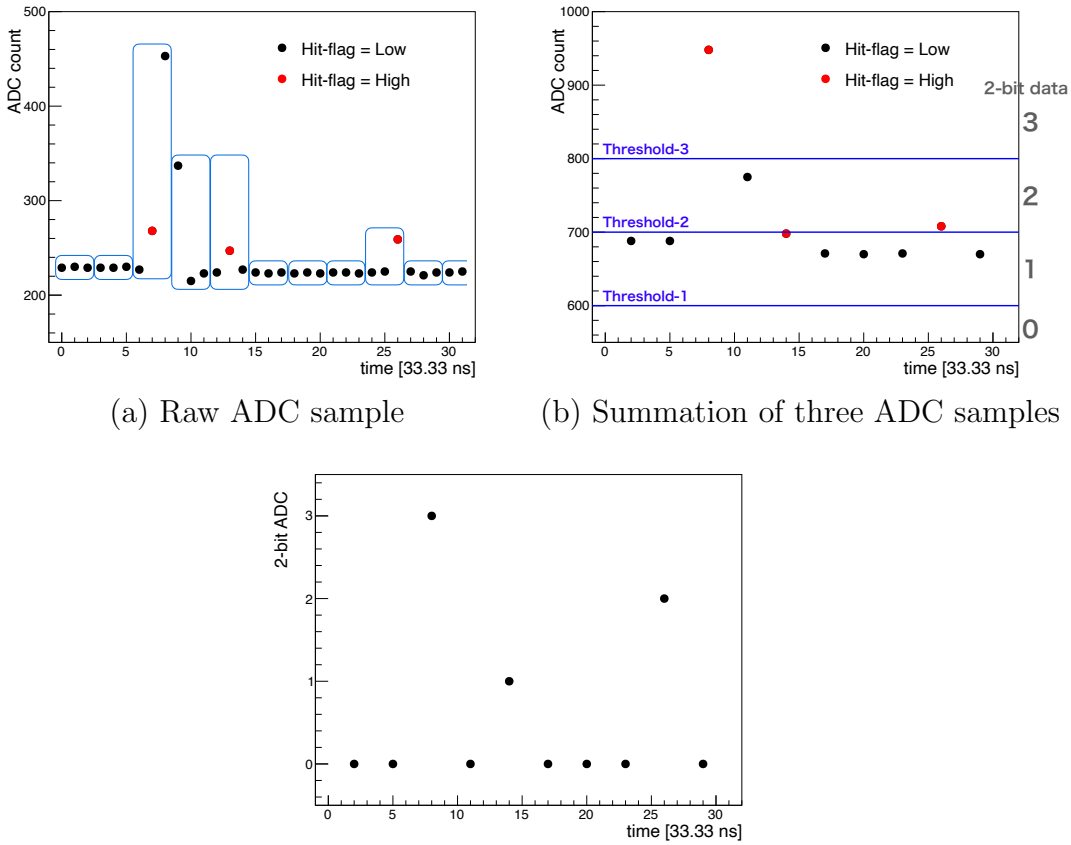

(a) Raw ADC sample

(b) Summation of three ADC samples

(c) 2-bit ADC data

Figure 4.2: ADC conversion process on the RECBE. The conversion is processed in the order of (a), (b), and (c). In panel (a), a blue box shows a group of three ADC samples, which are summed up.

bit data to COTTRI FE using the Aurora 8B/10B protocol provided as a LogicCore IP by Xilinx [44]. The maximum data transfer rate of Virtex5 is 3.125 Gbps/lane. In the trigger system, the frequency of the GTX reference clock is 120 MHz, which is a multiple of the shared clock of 40 MHz, and the data transfer rate is set to 2.4 Gbps/lane. The FCT distributes this 120 MHz clock, so it is received through RJ-45. The data format for Aurora is shown in Table 4.1. A data packet contains

Table 4.1: RECBE data format transferred to the COTTRI FE.

Bit	31	30 29 28 27 26 25	24	23 22 21 20 19 18 17 16 15 14 13 12 11 10 9 8	7 6 5 4 3 2	1 0
Header	0	Parity bits	1	Sent number	Board ID	
2-bit data	0	Parity bits	0	ch11 ←		0
	0	Parity bits	0	ch23 ←		12
	0	Parity bits	0	ch35 ←		24
	0	Parity bits	0	ch47 ←		36

2-bit flag data, 6-bit parity data, and 24-bit data. A data block has a header packet and four data packets: the header packet consists of a sent number of 16 bits and a board ID of 8 bits: each data packet consists of 2-bit data samples of 12 RECBE channels. Only for the header data, the 2-bit flag data is "2'b01". The parity bits are generated by an encoder of an error correction code (ECC) [45]. On the receiver side, the COTTRI FE board, an ECC decoder checks data flips in a data packet using both the data and parity bits: it outputs as follows:

- No data flip: data
- 1 data flip: recovered data and an alert signal
- >2 data flips: non-recovered data and an alert signal

4.2 COTTRI FE

The COTTRI FE board receives 2-bit data of each channel from the RECBEs and converts it to a score of each channel in the hit classification. This board was developed based on the design of the COTTRI MB, which is described in detail in the next section.

4.2.1 Components

The photograph of the COTTRI FE is shown in Figure 4.3. Main components are 11 DisplayPorts (DPs), an FPGA (Kintex7, xc7k355tffg901, Xilinx Inc. [41]), a clock jitter cleaner (Si5326 [46]), an SFP+ port, RJ45 socket, and regulators. This FPGA has 24 gigabit transceivers (GTXs), and each GTX consists of two differential signal pairs for a transmitter (TX) and a receiver (RX). All four signal line pairs are used for the communication: two GTX pairs for TXs and the other two GTX pairs for RXs. The SFP+ port has two lanes for a TX and an RX and occupies a GTX. Therefore, 23 GTXs are used in total. A DP next to the SFP+ slot is for communication with the COTTRI MB. By using its AUX lanes, the COTTRI FE catches the 40 MHz shared clock from the FC7 through the COTTRI MB. The other ten DPs are for communication with the RECBEs. By attaching an SFP transceiver, the SFP+ port works for the DAQ system. An RJ45 connector and a 14-pin joint test action group (JTAG) port are mounted. A 4-pin dip switch functions to select whether to use the RJ45 or 14-pin JTAG port. The details for regulator selection are provided in Appendix A.2.1.

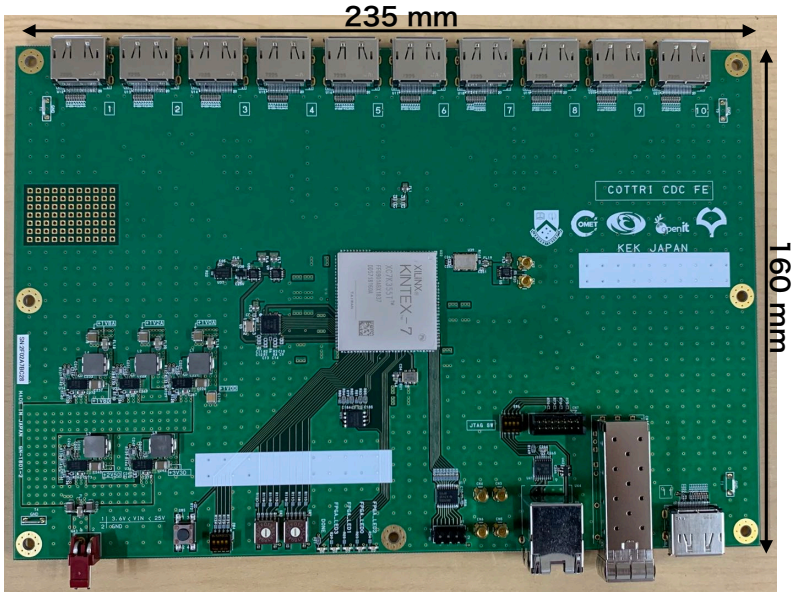

Figure 4.3: Photograph of the COTTRI FE board.

4.2.2 Firmware

All the functions on Kintex7 are summarised in Figure 4.4.

COTTRI system The CDC-hit data from the RECBE is received by using Aurora. The total transfer rate is calculated by:

$$\text{Total transfer rate} = 0.8 \times \text{Line rate} \times \text{Number of lane}. \tag{4.1}$$

The Aurora 8B/10B protocol performs at 2.4 Gbps/lane by applying a clock of 120 MHz. Two GTX lanes are used for the communication with a RECBE board, and then the total transfer rate is 3.84 Gbps/RECBE. ECC modules validate the received data. After ECC data validation, data from each RECBE is given a "valid" flag. Processes of the hit classification start with the timing when the number of "valid" flags exceeds the threshold value set on the register. Even if the communication with some RECBEs is failed due to some trouble, the COTTRI system continues the processes using healthy RECBEs. While the COTTRI system properly works, the hit classification is performed every 100 ns. Shift registers store 2-bit data from the RECBEs with shifting it every 100 ns. For data evaluation of a CDC cell, four samples from shift registers go to an OR circuit, so far. This means that CDC hits for 400 ns are evaluated at once because the time width of drift time distribution in a CDC cell is dominantly around 400 ns. This 400 ns is hereinafter called "integration time". This part can be modified to integrate three or five samples and convert 2-bit hit information as well. After the OR circuits, 6-bit input data for GBDT is generated by using 2-bit data of target and nearest neighbour channels in the CDC. The target channels having no data of neighbours in the COTTRI FE are merged with dummy data, which looks like a signal hit. Lookup tables (LUTs) convert the 6-bit data to the GBDT score optimised by the offline analysis and the simulation. The provided design elements do not include reconfigurable 6-input LUTs. Therefore, reconfigurable 5-input LUTs (CFGLUT5s [47]) carry out the conversion on

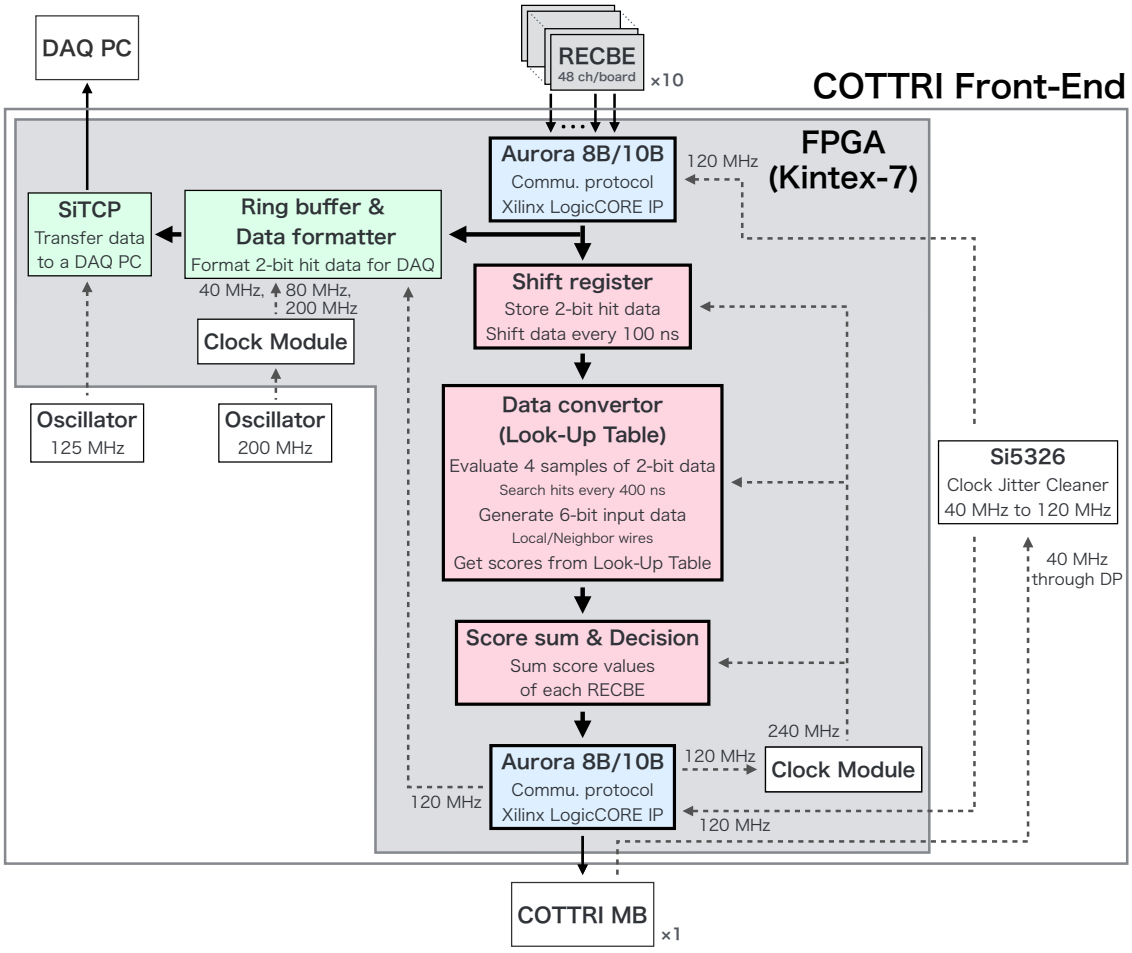

Figure 4.4: Block diagram of the COTTRI-FE firmware.

this step. 1 CFGLUT5 has 5-bit input and 1-bit output; two CFGLUT5s work as a 6-input LUT. Then, 2×6 CFGLUT5s are applied for a target cell. The CFGLUT5 settings are adjustable in operation by writing new setups to registers using UDP communication. All the scores of each RECBE are integrated. The data formatter creates a data stream, and the stream is sent to the COTTRI MB at 10 MHz by using Aurora 8B/10B. For this, the Aurora performs at 2.4 Gbps/lane with a 120 MHz clock, too. The format of the data sent to COTTRI MB is shown in Table 4.2.

Table 4.2: COTTRI-FE data format transferred to the COTTRI MB.

Bit	31	30 29 28 27 26 25	24	23 22 21 20 19 18 17 16	15 14 13 12 11 10 9 8 7 6 5 4 3 2 1 0
Header	0	Parity bits	1	Board ID	Sent number
Integrated score	0	Parity bits	0	RECBE 9	RECBE 8
	0	Parity bits	0	RECBE 7	RECBE 6
	0	Parity bits	0	RECBE 5	RECBE 4
	0	Parity bits	0	RECBE 3	RECBE 2
	0	Parity bits	0	RECBE 1	RECBE 0

DAQ The 2-bit data from the RECBEs is the initial input to the COTTRI system. Ring buffers store the 2-bit data by applying a 120 MHz clock coming from Aurora

so that offline analysis can reconstruct all the trigger-related processes. When a trigger signal is asserted, this data is read from the ring buffers, and sent to a DAQ PC by using SiTCP. The data format is presented in Appendix A.2.2.

Clocking There are four clock sources in the firmware of the COTTRI FE: a 200 MHz oscillator, a 125 MHz oscillator, AUX lanes of a DP cable used for the communication with the COTTRI MB, and a 120 MHz user clock of Aurora. The clock line from the 200 MHz oscillator is a clock source of:

- 200 MHz for SiTCP, registers, and FPGA monitor systems,
- 80 MHz for initialization schemes of Aurora, and
- 40 MHz for reset-signal generators of Aurora.

The clock from the 125 MHz oscillator goes to a pair of FPGA pins dedicated to the GTX reference clock and is used as the GTX clock for SiTCP. The use of this on-board oscillator allows the COTTRI FE to perform as a stand-alone device in the trigger system, and the DAQ system can check its status even if the communication with other trigger-related boards fails. The COTTRI FE receives the 40 MHz clock from the COTTRI MB through AUX lanes of a DP cable, as seen in Figure A.3(b). This clock is synchronous with the timing of the data transfer between the FC7 and the COTTRI MB. This clock signal goes to Si5326 through Kintex7, and Si5326 converts it to a 120 MHz clock for GTXs communicating with both the COTTRI MB and the RECBEs. Aurora outputs a 120 MHz clock that is synchronous with the reference clock of the GTX, and this clock is called "user clock". The user clock is an input clock of PLLE2_BASE provided by Xilinx [47] to generate a stable 120 MHz clock for Aurora data processing and a 240 MHz clock for the trigger-related parts in the firmware.

4.3 COTTRI MB

The COTTRI MB board receives score data of each RECBE from the COTTRI FE boards and makes trigger decisions in the event classification.

4.3.1 Components

The photograph of the COTTRI MB is shown in Figure 4.5. The main components are ten DPs, an FPGA (Kintex7, xc7k355tffg901, Xilinx Inc.), a clock jitter cleaner (Si5326), two SFP+ ports, two oscillators, and regulators (LT8612). Each component has the following roles:

- Ten DPs are used for the communication with the COTTRI FEs to receive the CDC trigger data and send the shared clock and the status of the CyDet trigger system.
- Kintex7 works for digital data processing such as the event classification and data format for DAQ.
- Si5326, using the 40 MHz shared clock from the FC7, generates an accurate clock of 120 MHz for GTXs on Kintex7.

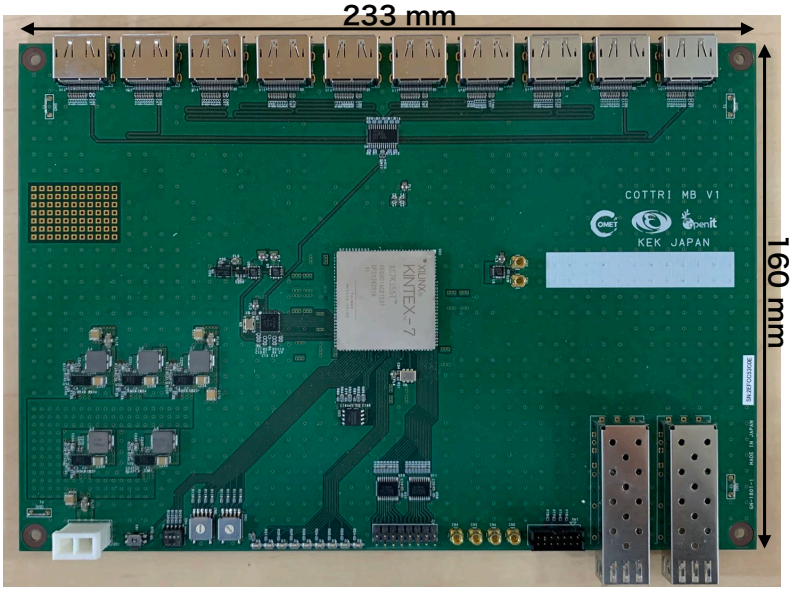

Figure 4.5: Photograph of the COTTRI MB board.

- Two SFP+ ports are used for the communication with the FC7 and a DAQ PC.
- One oscillator provides a 200 MHz clock for the system clock in the firmware. The other oscillator provides a 40 MHz clock to support the MGT link.
- Regulators supply the stable voltages to the electronics components. The input voltage is required to be over 5 V and is limited to 6.7 V due to the absolute maximum ratings of capacitors.

4.3.2 Firmware

All the functions on Kintex7 are summarised in Figure 4.6. The COTTRI-MB firmware has the same schemes like the one of the COTTRI FE, such as the system for the register, the system monitor, Aurora, and SiTCP.

COTTRI system The Aurora module receives the RECBE-score data from the COTTRI FEs every 100 ns. Then, it works at 2.4 Gbps/lane with a 120 MHz clock. Two GTX lanes are used for each data-transfer line to communicate with the COTTRI-FE, and the total transfer rate is 3.84 Gbps/COTTRI-FE given by Equation 4.1. The data validation system is the same as the COTTRI-FE firmware. Valid data of each COTTRI FE is given a "valid" flag. The score data is sequentially evaluated every clock cycle in parallel. Figure 4.7 shows the data flow in the current firmware. All the scores are summed up in two steps. When the number of "valid" flags exceeds a threshold value, the summed score is evaluated. Firstly, for data from each COTTRI FE, the number of signal-like hits are calculated. Secondary, the total number of signal-like hits is aggregated. If it exceeds a threshold value which is set on the register, the internal trigger is asserted. This trigger signal is sent to the FC7 as the CDC trigger. The current firmware does not include a function to

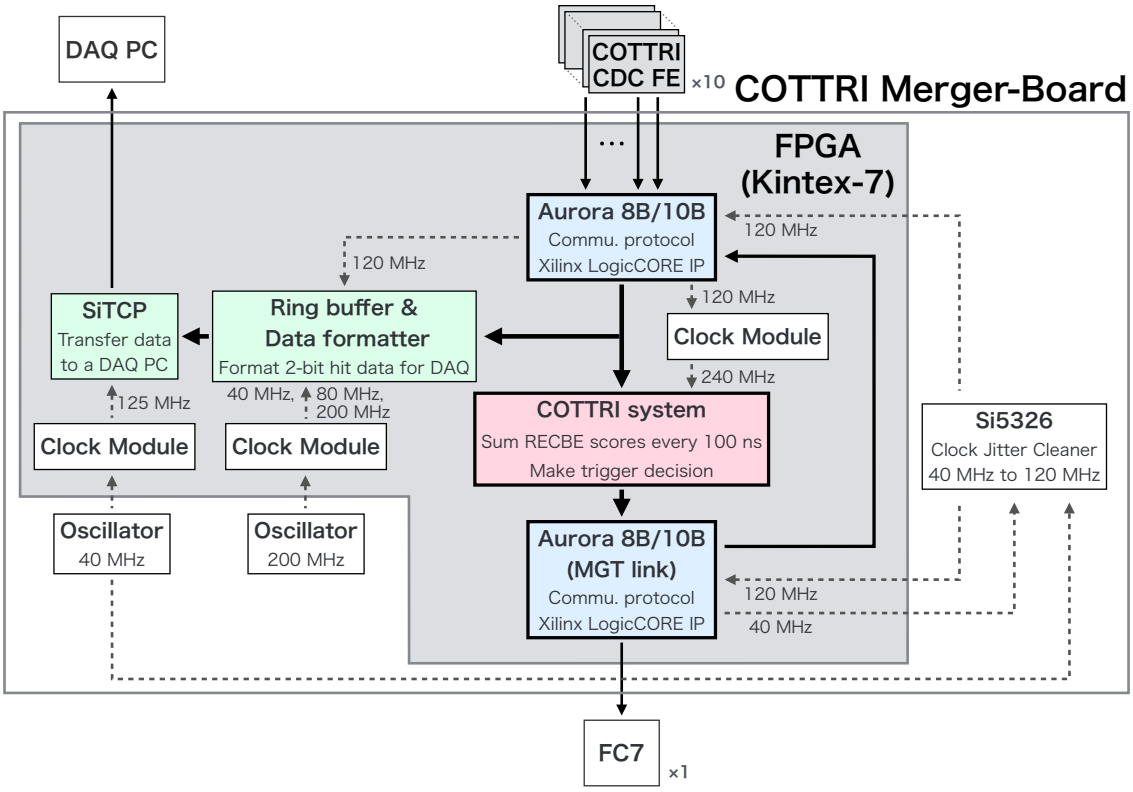

Figure 4.6: Block diagram of the COTTRI-MB firmware.

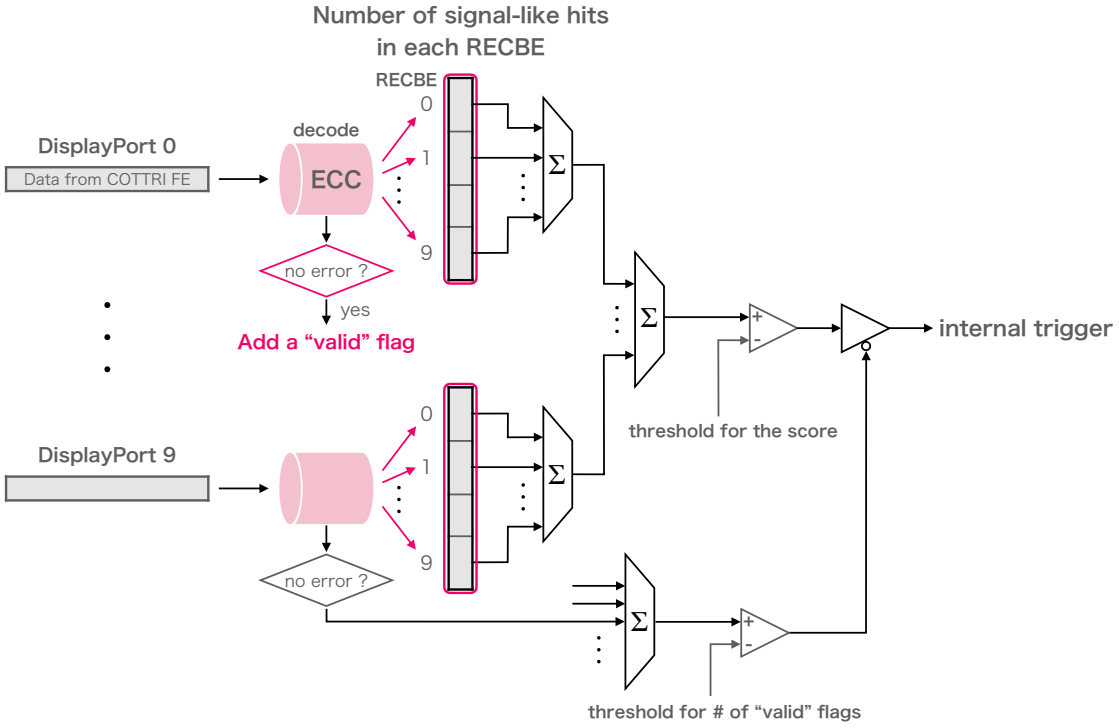

Figure 4.7: Block diagram of the COTTRI system on the COTTRI-MB firmware.

make the trigger decision for each CTH module as described in Section 3.2, and the total number of the CDC signal-like hits is calculated. This is because it is used for operation tests using not the entire readout area but a part of the readout area in the CDC. When all the readout components become ready, its trigger function will be implemented.

DAQ Ring buffers store the RECBE scores from the COTTRI FEs. The process of formatting event data is the same as the processes handled in the COTTRI-FE firmware. Data taking can be performed by using an internal trigger (CDC trigger) generated in the COTTRI MB or an external trigger from the FC7. The data format and the trigger modes are presented in Appendix A.3.1.

Clocking There are four clock sources in the COTTRI-MB firmware: a 200 MHz clock from the oscillator, a 40 MHz clock from the oscillator, a 120 MHz user clock of Aurora, and a clock generated by the MGT link. The roles of the 200 MHz clock and 120 MHz clock are the same as their roles in the COTTRI-FE firmware. The 40 MHz clock is converted to a 125 MHz clock that is used at the GTX clock for SiTCP.

The COTTRI MB receives the data from the FC7 at 120 MHz using the MGT link. Its header signal is periodic at 40 MHz because three clock cycles are needed to transfer the trigger data, as mentioned in Section 2.4. This periodic signal is useful to generate clocks for the COTTRI MB to construct the synchronised communication system. Si5326 converts this 40 MHz clock to an accurate 120 MHz clock for GTXs used by the communications with the FC7 and the COTTRI FE. Until the communication with the FC7 is stable, a 40 MHz clock from the on-board oscillator goes to Si5326 through FPGA. When the communication becomes stable, the clock going to Si5326 is switched to the 40 MHz clock from the MGT link immediately.

Chapter 5

Hardware performance of the trigger system

The operation test of the COTTRI system was performed. Its purpose is to measure the latency of the entire trigger system and confirm that the COTTRI system correctly works in a setup of the CDC cosmic-ray measurement. These results are summarised in this chapter.

5.1 Latency measurement

The latency from the trigger system needs to be short enough not to miss the signal data. As mentioned in Section 2.3.1, the buffer time of the RECBE is 8 μs, and the length of the event window is 1 μs. Then, all the trigger processes must be done within 7 μs at most. This processing time was measured in this operation test.

5.1.1 Experimental setup

In order to measure the trigger processing time, a loop-back system was set up with all the types of electronics related to the CDC trigger, as shown in Figure 5.1. This RECBE has an input connector. Its line connects with the ASD test pin to test the ASD and ADC performance. A test pulse from the function generator was input as a substitute for the CDC signal. The COTTRI system starts the trigger process at the timing of this test pulse to generate the trigger signal. By using an oscilloscope, the processing time was measured at three points, as shown in Figure 5.1: a pin header on the COTTRI FE to measure the timing of finishing the score calculation, a pin header on the COTTRI MB to measure the timing of generating the CDC trigger signal, and an RJ-45 socket on the RECBE to measure the timing of receiving the trigger signal from the FCT. The trigger of the oscilloscope was set to the test pulse timing.

5.1.2 Measurement result

Figure 5.2 illustrates the timing structure of the trigger system. The CDC trigger timing fluctuated within 100 ns because of the trigger decision at 10 MHz. This screenshot shows that it took 1.94 μs to 2.04 μs from taking the signal to receiving the trigger signal. As described in Section 4.2.2, the integration time of 400 ns was

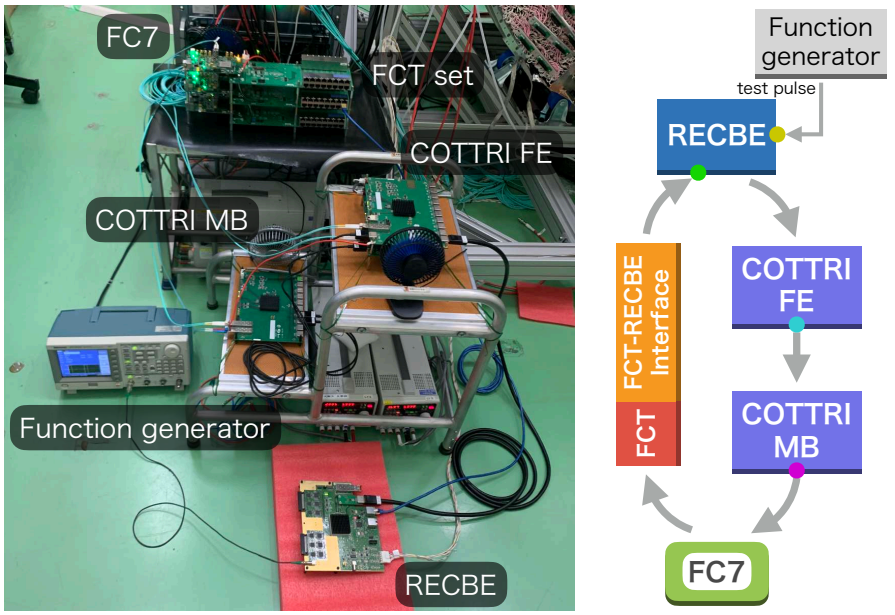

(a) Photograph (b) Block diagram

Figure 5.1: Photograph and block diagram of the setup for measuring the trigger processing time. In the panel (b), each colour circle is a point for the waveform measurement using an oscilloscope and a probe. Only for the test pulse, a LEMO cable was used instead of a probe.

adopted to consider the drift time distribution in the CDC cell. Furthermore, it takes 800 ns to receive the 32-bit trigger data at 40 MHz on the RECBE. Together, the maximum time for the full trigger processing is 3.24 μs. These values are summarised in Table 5.1. This value potentially changes for tens of nanoseconds after a power

Table 5.1: Latency of the trigger signal.

Processing time in the full trigger system	1.94 μs to 2.04 μs
Integration time for the drift time	0.4 μs
Time for receiving the trigger data on the RECBE	0.8 μs
Total	3.14 μs to 3.24 μs

cycle of the RECBEs because the Aurora communication starts with a different GT clock phase from the phase in the previous run. However, it was not changed over the duration of the same operation period. The trigger latency including this change satisfies the requirement.

5.2 Communication performance test

It is important to make sure that all of the functions in the COTTRI system properly work in a realistic measurement setup. To this end, an operation test was carried out using a part of the CDC readout region in the setup of a cosmic-ray measurement.

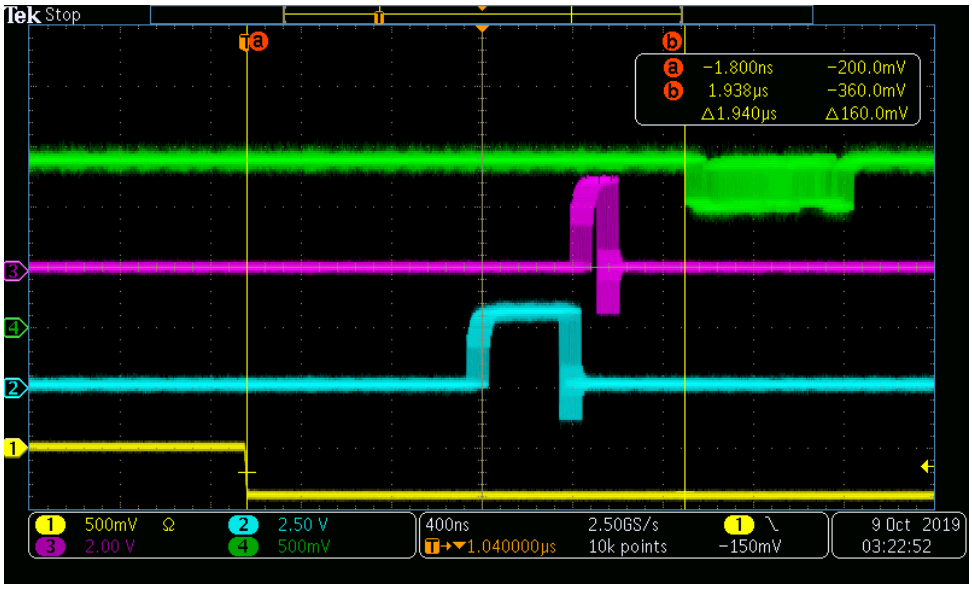

Figure 5.2: Screenshot of the oscilloscope showing the time structure of the trigger system. A persistence display mode was adopted for this screenshot. The yellow wave is a test pulse going to the RECBE. The oscilloscope trigger was set to this channel. The light blue wave shows the timing of finishing the score calculation on the COTTRI FE. The magenta wave shows the timing of the trigger signal generated on the COTTRI MB. The green wave is the waveform of the trigger signal at the RJ-45 on the RECBE. This trigger signal contains the 32-bit trigger number. The trigger decision was carried out every 100 ns, so all waves except for the yellow line fluctuate within 100 ns.

5.2.1 Experimental setup

To evaluate the CDC performance, the CDC cosmic-ray test was carried out on the 4th basement floor of the Fuji building in KEK [48]. Figure 5.3 shows a photograph of the test setup, and Figure 5.4 shows the trigger logic for this measurement. The cosmic-ray events were triggered by using two sets of a photomultiplier tube and a timing counter placed both at the centre and bottom of the CDC. In this test, all the types of electronics related to the CDC trigger were driven for taking the event data: an FC7, four FCTs, three FCT interface boards, two COTTRI FEs, a COTTRI MB, and 19 RECBEs. Since the FC7 receives a sinusoidal wave of 12 MHz from the J-PARC accelerator during the physics run, a pseudo signal of a similar sinusoidal wave from a function generator was used as an input to the FC7. Attaching a special adapter to one of the RECBEs allows it to take the trigger signal from PMTs via discriminators. A photograph of this adapter is shown in Figure 5.5. The RECBE related to the cosmic-ray trigger took coincidence between both timing counter signals to select cosmic-ray events and send the trigger signal to the FC7 via one of the FCTs. Its firmware was different from the firmware of the others and did not need the 120 MHz clock for the GTXs. One FCT set made of the FCT and the FCT interface board, connected with this trigger RECBE and was operated without an output clock of 120 MHz. Other two sets connected with the other 18 RECBEs via 3 m Ethernet cables. Using the MGT links, the FC7 communicated with the FCTs and the COTTRI MB via four 1 m and one 3 m optical cables, respectively.

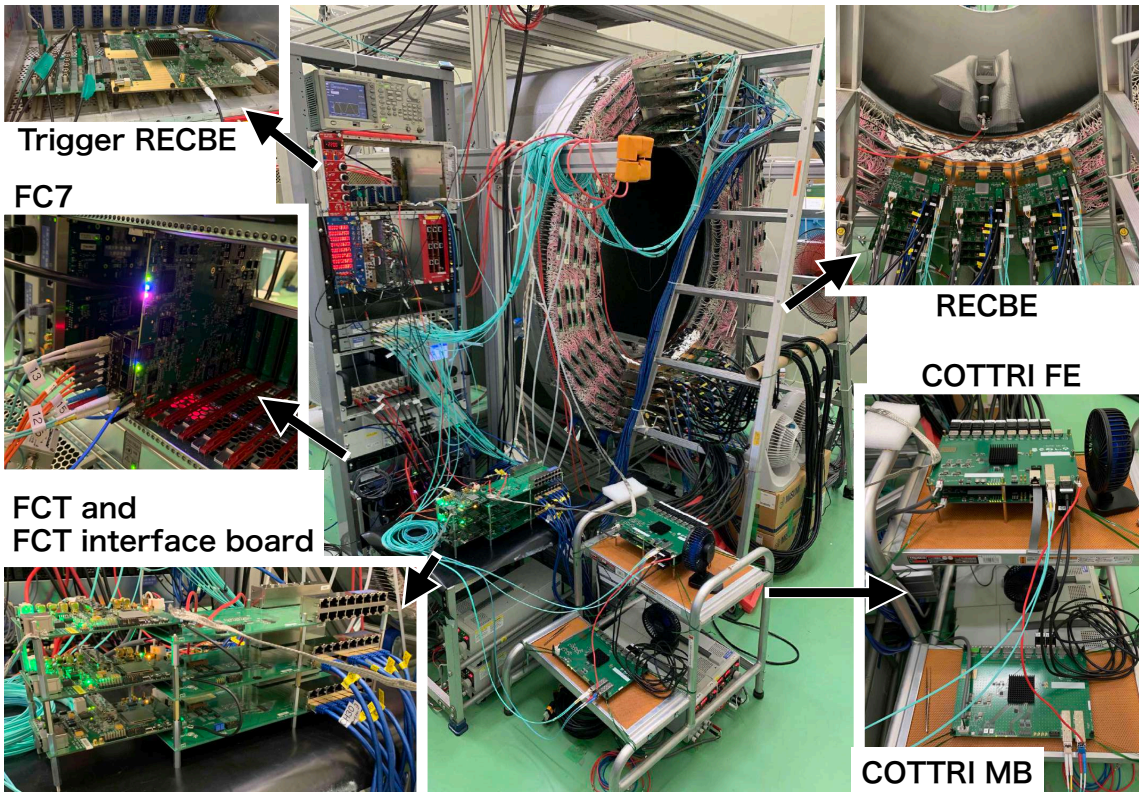

Figure 5.3: Photograph of a setup of the CDC cosmic-ray test. The function generator was put on top of the NIM crate. The RECBE dedicated to the timing counter signal was located second from the top in the NIM crate. The FC7 in the μTCA crate is on the bottom of the NIM crate and behind the FCTs. The trigger counters are at the centre and bottom of the CDC.

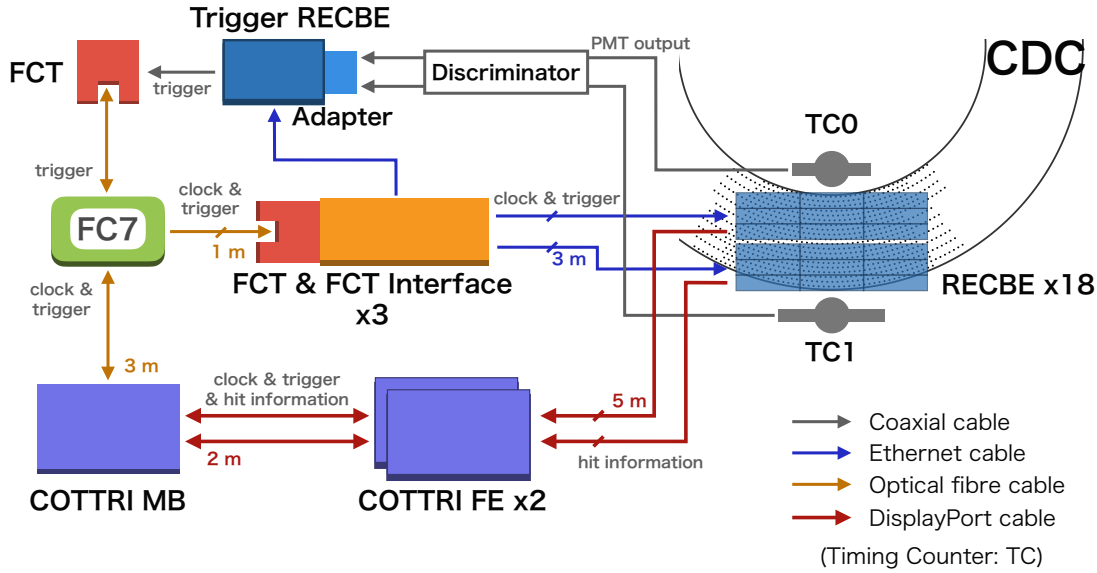

Figure 5.4: Trigger logic for the cosmic-ray measurement.

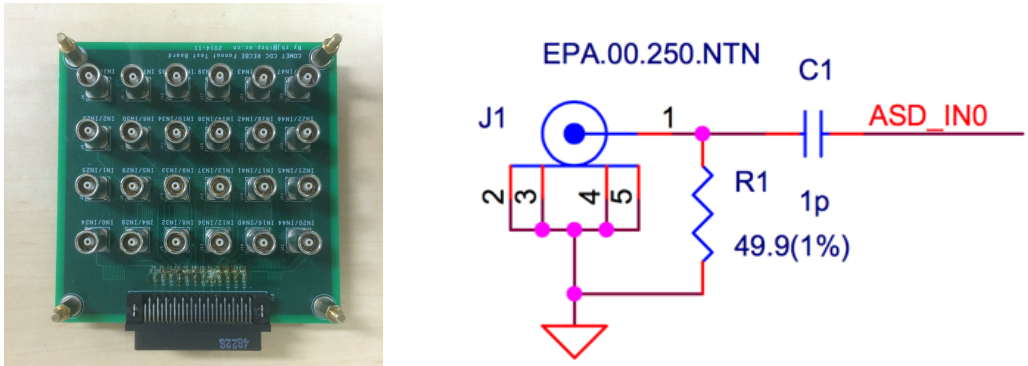

(a) (b)

Figure 5.5: Photograph of the adapter attached to the RECBE board for charge input. (a) and (b) are its photograph and circuit diagram, respectively.

The COTTRI MB transmitted the trigger-related data with two COTTRI FEs via 2 m DP cables. Each COTTRI FE received the CDC-hit data from nine RECBEs using 5 m DP cables.

The firmware discussed in Chapter 3 was implemented on both the COTTRI FE and MB to make the trigger decision. On the COTTRI FEs, an output of the LUT for each channel was:

- 6'b000000 if the 6-bit input was 6'bXX00XX or
- 6'b000001 if the 6-bit input was an other number,

where X indicates that either 0 or 1 was acceptable. Then, summing up the outputs for all the readout channels on the COTTRI MB was the same as counting the number of hit wires (hits) in the CDC. The three thresholds to convert ADC-sum to 2-bit data were 0, 700, and 1000 counts. The threshold for the trigger decision in the event classification was 14 hits. In this test, this threshold is equivalent to the one for the number of CDC hits. When the total number of hits exceeded the threshold, the COTTRI system made an internal trigger signal of 1 bit. After a trigger was fired, a veto window of 1 μs was also applied.

In this measurement, the data from the RECBEs, COTTRI FEs, and COTTRI MB was taken for each triggered event by using DAQ-Middleware (DAQMW) [49]. In the current DAQ system, the data from all the electronics cannot be taken by a DAQ PC. Therefore, a DAQ PC was utilised for an electronics type, and three DAQ PCs were operated. The raw mode of the RECBE DAQ was adopted to compare the RECBE data with the other board data. In an event, the RECBE recorded 32 data samples for each channel. The COTTRI FE and MB recorded 64 samples in the event window of 6.4 μs. Figure 5.6 shows an example of the online monitor for the COTTRI FEs.

Slow control and monitor system for the electronics was carried out by KiNOKO [50]. The errors in each Aurora communication line were monitored. This system also monitored values of FPGA temperature and voltage and controlled register values in each firmware. Figure 5.7 shows the online monitor of KiNOKO. This system monitored communication statuses with four parameters: single-bit errors (SBE), double bits errors (DBE), a value of a soft error counter (SEC), and

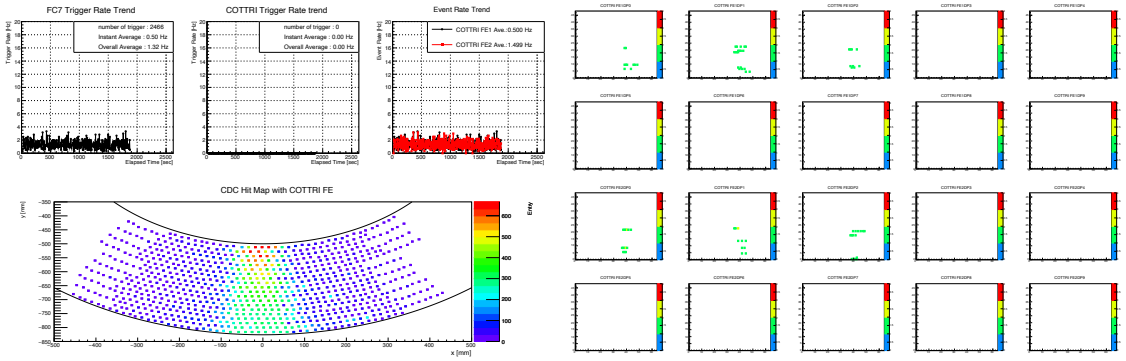

Figure 5.6: DAQ online monitors for the COTTRI FEs. The three left-top plots show the trigger rate and the acquired-event rate. The bottom left plot draws the CDC hit map using the COTTRI-FE data. The 20 small plots on the right side show the timing distribution of the CDC hits received by each DP and are updated every triggered event. On these timing plots, the horizontal axis represents sampling every 100 ns, the vertical axis represents the channel number of each RECBE, and the number of hits on each channel within 100 ns is represented by colouring each bin.

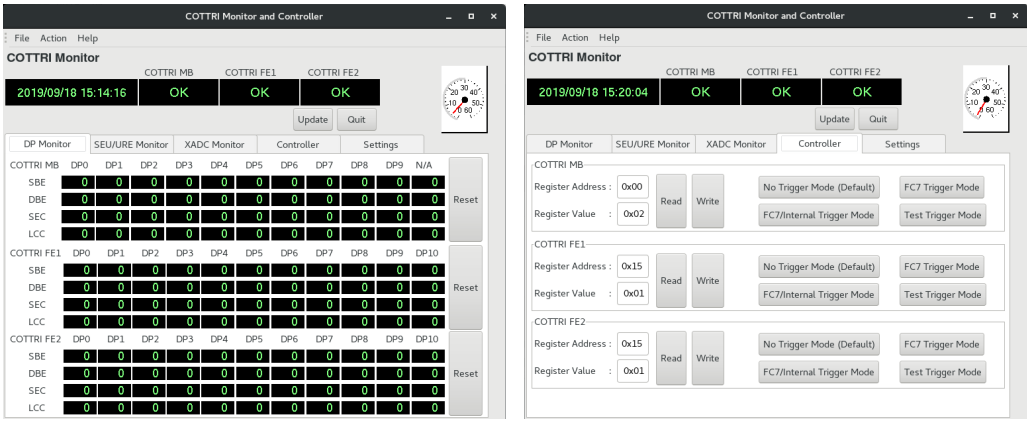

(a) communication errors (b) controller for registers

Figure 5.7: Monitor and controller for the COTTRI system. (a) is a monitor for the communication error. (b) is a controller to adjust register values. The other tab monitors the number of SEU and URE, the FPGA temperature on each board, and the input voltage for each FPGA.

a value of a lost connection counter (LCC). SBE and DBE are the numbers of errors detected by the ECC. SEC represents the number of both single-bit errors and multi-bit errors detected in the Aurora protocols. LCC represents the number of times the communication was lost. The operation test was carried out while the status of the communications and the electronics was checked.

5.2.2 Measurement

The cosmic-ray events were taken for 739 minutes. 60375 RECBE events, 60374 COTTRI-FE events, and 60348 COTTRI-MB events were taken in total. It was confirmed that the difference in these numbers was caused by the DAQ PCs and

their network. Here, only the events taken by all the DAQ PCs were used to evaluate the performance of the COTTRI system.

Communication check

First, the monitor data was checked. The SBE, DBE, SEC, and LCC on each board are shown in Figure 5.8 and Figure 5.9. On the COTTRI MB and two COTTRI FEs, no communication trouble was found during the measurement.

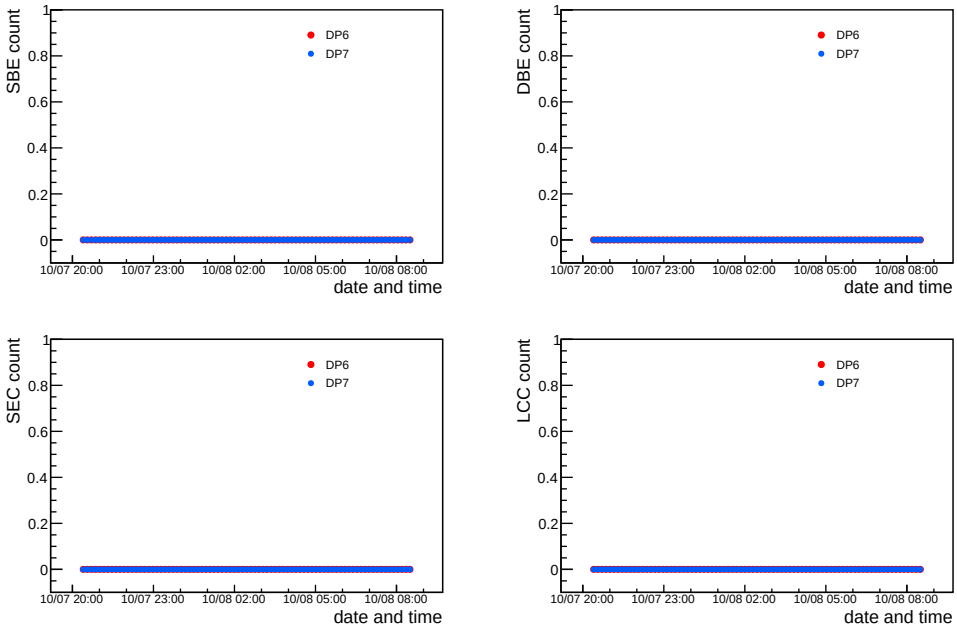

Figure 5.8: Communication quality of the COTTRI MB. DP6 and DP7 represent the COTTRI FEs communicated with the COTTRI MB..

Data compatibility between RECBE and COTTRI FE

The RECBE data of the raw mode contains ADC counts of each sample. The 32 samples of the RECBE data in the event window can construct ten samples of the 2-bit COTTRI-FE data by applying the thresholds, as described in Figure 4.2. In a cosmic-ray event, only the data of hit channels were analysed. These ten reconstructed samples were compared with the 2-bit data taken by the COTTRI FEs. Figure 5.10 shows an example of the comparison between the COTTRI-FE data and the reconstructed data. In this event, the 36th to 45th COTTRI-FE sample are fit with the reconstructed data. For this reason, the 36th sample of the COTTRI-FE data corresponds to the start timing of the event window on the RECBE. All other events are checked by applying the same way, and the data compatibility was confirmed, as shown in Figure 5.11. Six RECBE channels, 330 to 335, are not used to read the CDC signal out. The hits on those channels were caused by the cross-talk effect on an ASD. The zigzag shape of this distribution is understandable with the hit map in Figure 5.12. The RECBE channels of 0 to 287 were located at the centre of the readout region. Due to the small size of the timing counter on the

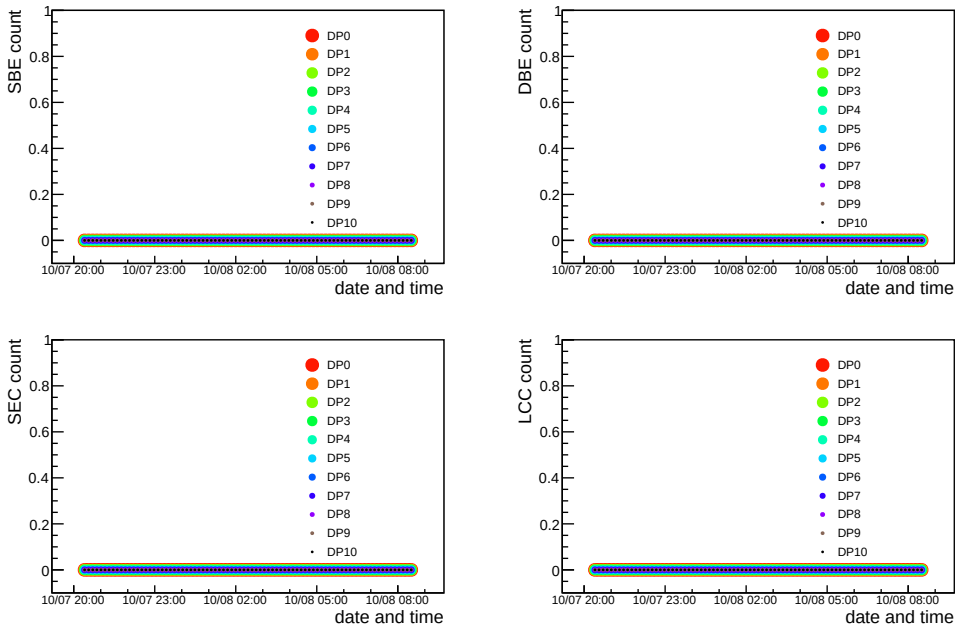

(a) COTTRI-FE 0

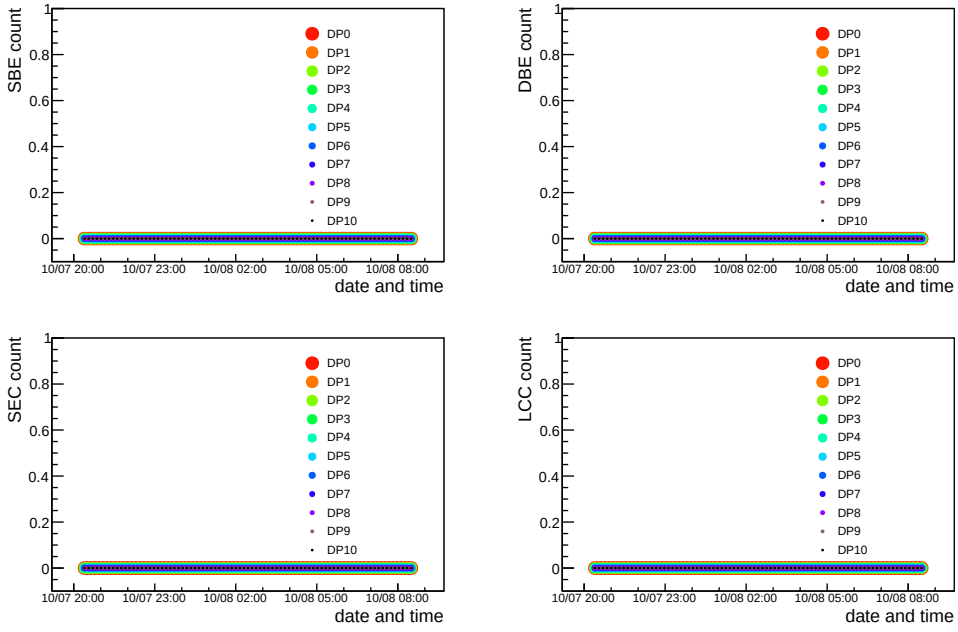

(b) COTTRI-FE 1

Figure 5.9: Communication quality of the COTTRI FEs. Each set of four plots is a COTTRI FE data. DP0 to DP9 were used to connect with the RECBEs, and DP10 was used to connect with the COTTRI MB.

CDC centre, these 288 channels had more hits than the other channels. The hit distribution in the others was asymmetric because the timing counters were off the centre of the CDC. An entry for each RECBE channel is in disagreement with the COTTRI-FE data. These mismatched-event numbers of all the channels are the same. All the distributed clocks are in sync with each other in the entire trigger system. However, if one focuses only on the RECBE board, the Aurora protocol is

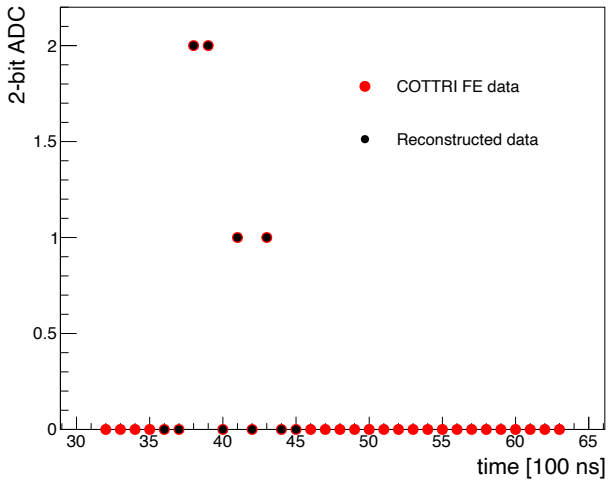

Figure 5.10: Example of the comparison between the waveform (red dots) from the COTTRI-FE data and the reproduced waveform (black dots) from the RECBE data.

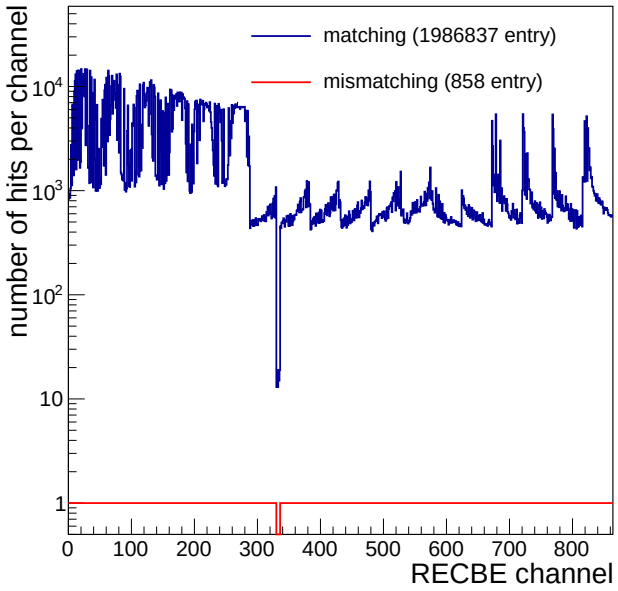

Figure 5.11: Data compatibility between the RECBE and the COTTRI FEs.

asynchronous to the ADC interface because it individually receives two clocks via the RJ-45 socket. No communication error in the communications, as discussed in Section 5.2.2, indicates that that event might be caused by some electric noise in the FCTs. Even if instability of the COTTRI system was the cause, this phenomena was rare enough for the sensitivity.

The communication accuracy was evaluated without the mismatched event. The transmitted data size is 2 bit/ch/sample $\times$ 10 sample in an entry, and the number of the matched entries is 1986837. Then, the error rate was estimated to be less than 2.5×10^{-8} /bit. It is not sensitive enough to estimate the error rate in the 150-day physics measurement, but this is the first time to operate the COTTRI system that

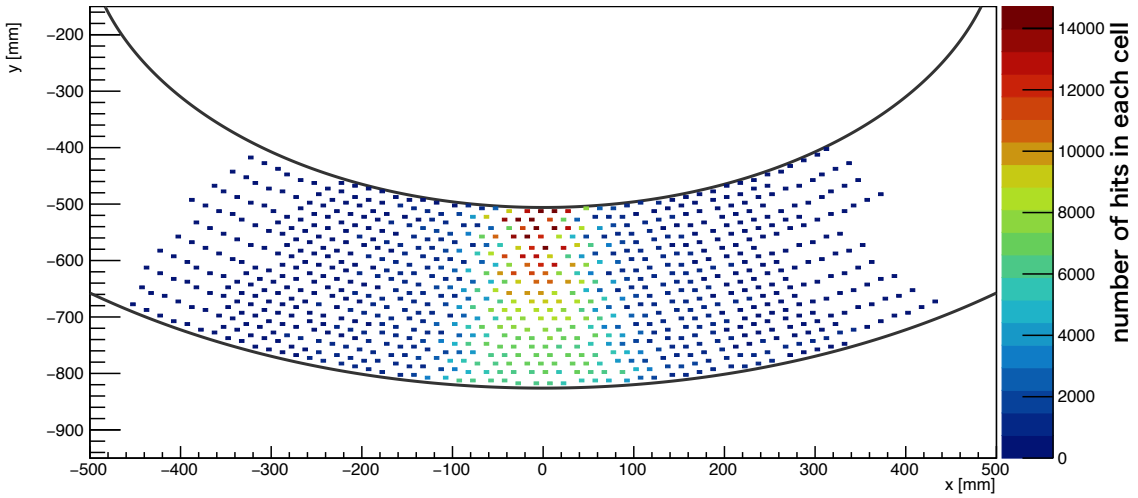

Figure 5.12: Hit map of the CDC in the cosmic-ray measurement.

triggers cosmic-ray events in the CDC setup. And, in communication tests without the CDC setup, the error rate has been measured with larger statistics and been found to be low enough for operation [51].

Data compatibility between COTTRI FE and COTTRI MB

The purpose of this analysis is to validate the data processing on the COTTRI FE and the communication between the COTTRI FE and MB. This validation was done by reconstructing the COTTRI-MB data from the COTTRI-FE data. Missed events were searched from all the data by checking the event number from the FC7. Five events on the COTTRI MB were not recorded in the COTTRI-FE DAQ PC, so 60343 events were analyzed below.

The COTTRI-FE data gives the time variation of the number of CDC hits having non-zero 2-bit data, as shown in Figure 5.13. Around 3.7 μs, the number of CDC hits increased in many events; this is the trigger timing of the timing counters. A huge electric noise might have happened for longer than 3.5 μs and made hits in almost all the wires at the same time bin. In each event, the number of CDC hits was integrated into 400 ns, and the time variation of the integrated number was compared with the COTTRI-MB data. In this measurement, the summation of the LUT outputs is equivalent to the number of CDC hits. It was transmitted from the COTTRI FEs to the COTTRI MB and taken by the DAQ system. The time variation of the number of CDC hits from the COTTRI-MB data was seen in Figure 5.14. In the COTTRI-MB data, the electric noise was seen; the number of CDC hits within the integration time became the total number of the CDC wires used in this measurement. Figure 5.14 has to be reproduced from the data in Figure 5.13, and it was confirmed. The time range for the comparison was set to be from 2.0 μs to 5.2 μs in Figure 5.14.

The data recorded on the COTTRI MB was reconstructed by using the COTTRI-FE data, which includes the 2-bit data in each cell. Figure 5.15 illustrates the way to reconstruct the COTTRI-MB data. Because of the time for transmitting data, the data timing of the COTTRI FE and MB is not the same. The COTTRI FE receives the external trigger signal from the FC7 via the COTTRI MB. The trigger timing

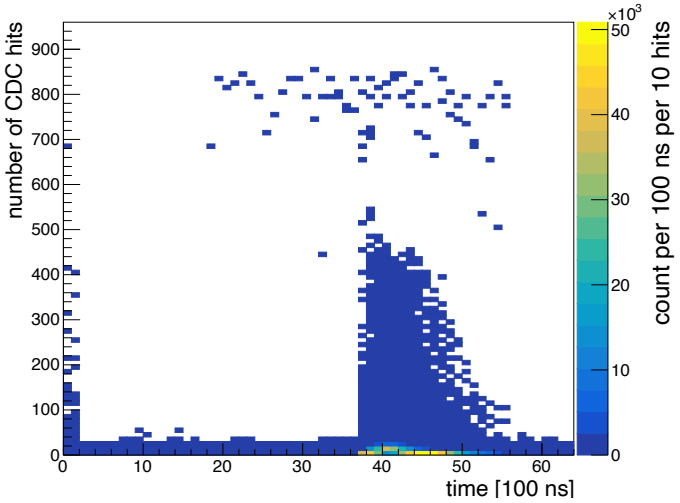

Figure 5.13: Time variation of the number of CDC hits within 100 ns. The plot is drawn by using the COTTRI-FE data. The first two samples had a timing issue in the firmware; they were not used for the analysis.

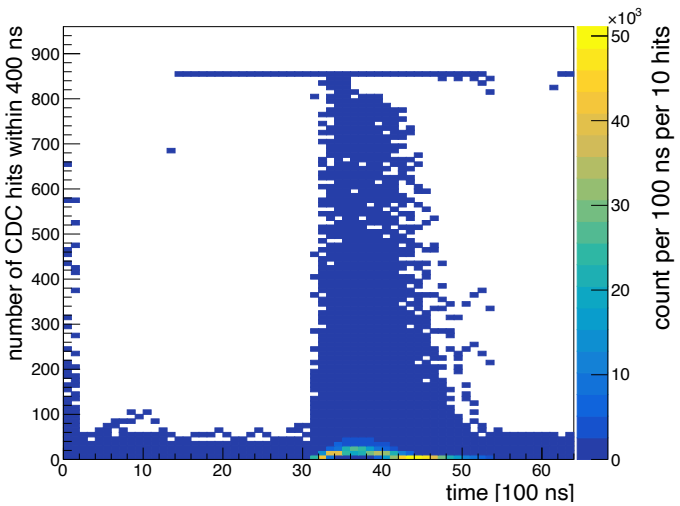

Figure 5.14: Time variation of the number of CDC hits within 400 ns. The plot is drawn by using the COTTRI-MB data, therefore, the integration time of 400 ns is considered. The first two samples had a timing issue in the firmware; they were not used for the analysis.

on the COTTRI FE is slightly delayed from the timing when a charged particle passes through the CDC more than the one on the COTTRI MB by an event. This timing gap was investigated while the correspondence between the reconstructed data and the COTTRI-MB data, as shown in Figure 5.16. All of the events on the COTTRI MB were successfully reconstructed. It was found that the timing gap was not constant and was 500 ns or 600 ns in this measurement. 276 events are no-hit events on both COTTRI FE and MB data, and all of them make no-data-timing-gap events. The existence of them is also seen below.

Although the statistics were not huge, the communication accuracy was also evaluated. The number of events is considered to be 60067, and the 276 events

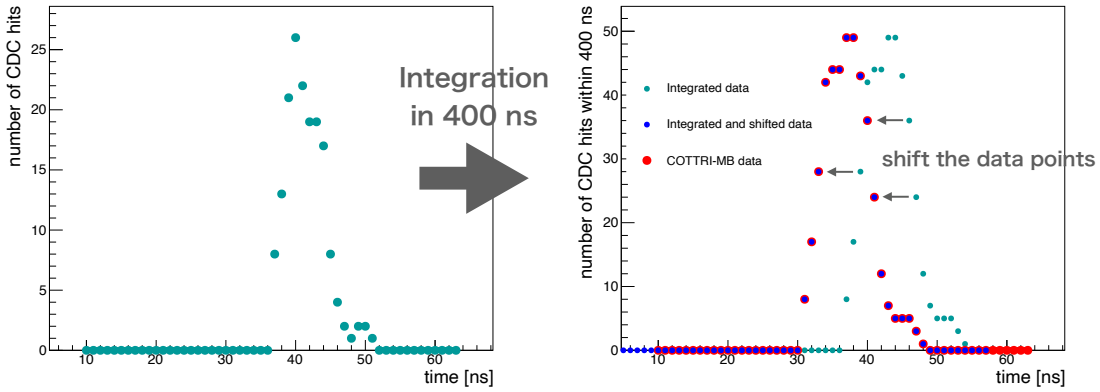

Figure 5.15: Way to reconstruct the COTTRI-MB data. (1) Counting the number of CDC hits in each sample (left). (2) Integrating the number of CDC hits in 400 ns (right: cyan circles). (3) Shifting the timing to consider the data transfer time between the COTTRI FE and MB. In this case, the timing gap is six samples, and the COTTRI-FE data is 600 ns earlier than the COTTRI-MB data.

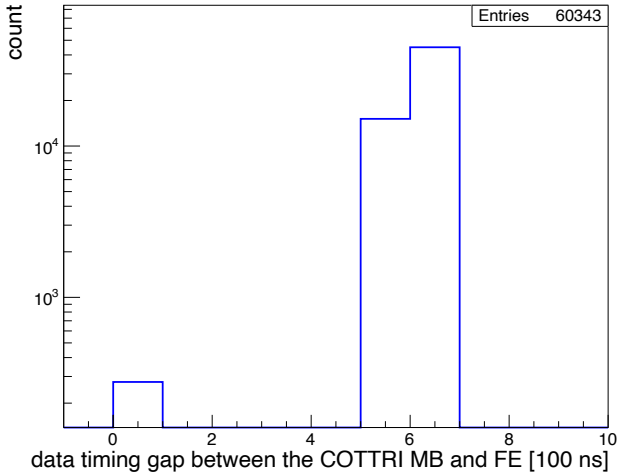

Figure 5.16: Timing gap between the COTTRI MB and FE data. This timing gap calculated by the event matching as explained in Figure 5.15. 276 events having no gap are no-CDC-hit events.

are excepted. The transmitted data size is 120 bit/sample for a COTTRI FE, 32 samples in an event are analyzed, and two COTTRI FEs communicated with the COTTRI MB. Then, the error rate was estimated to be less than 2.2×10^{-9} /bit. As with the communication between the COTTRI FE and the RECBE, the error rate has been measured with much larger statistics in the lab test and would not affect the experimental sensitivity [51].

Internal-trigger decision process

The header of the COTTRI-MB data contains the internal-trigger timing as 32-bit data from the shift register, as shown in Figure A.3. The internal trigger was

reconstructed from the COTTRI-MB data in offline analysis to confirm that the processes on the COTTRI MB worked for the internal-trigger decision properly.

The internal trigger on the COTTRI MB is generated by applying the event classification and sent to the FC7 as the CDC trigger. Then, the event classification was carried out by using the data from the COTTRI FEs. In the offline analysis, this classification process was reproduced, and the internal trigger was reconstructed. The threshold for the trigger decision in the event classification was set to be 14 as with the firmware setup. Validation of the internal-trigger decision process is performed by comparing the timing of the internal trigger in the COTTRI-MB data (online internal trigger) with the reconstructed one by event. For example, reconstructed trigger timing in the event in Figure 5.15 is at 3.2 μs in the COTTRI-MB data. The timing distributions of them are shown in Figure 5.17. The timing

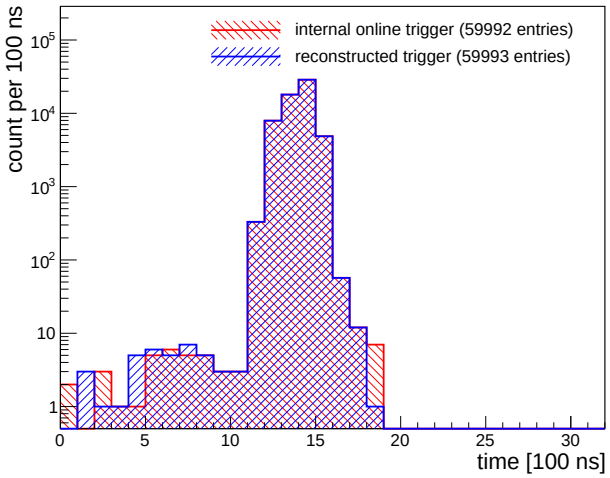

Figure 5.17: Comparison of the time variation between the online internal trigger and the reconstructed one. The online internal trigger is generated on the COTTRI MB, and the reconstructed trigger in the offline analysis is produced by using the data from the COTTRI FEs. Only the first trigger in an event is filled.

of the online internal trigger was recorded only for 3.2 μs while the COTTRI-MB data for the reconstruction was taken with the event window of 6.4 μs. So, the reconstructed distribution is fitted with one of the online internal triggers at a rising edge of 1.1 μs. They are a little different from each other. This was caused by a bug in the firmware of the COTTRI MB. The timing data of the internal trigger varies every 100 ns, as explained before. While event data is formatted for DAQ, that type of data should be stored in a register in order not to be changed. In the tested firmware, it was not actually like that, and the timing data could be changed for each taken event. Currently, this bug has been already fixed. In the analysis, all the mismatching events by this bug were removed from the analyzed events. The timing distribution after the modification is shown in Figure 5.18. The internal trigger was reconstructed well in the offline analysis; it was concluded that the data processing on the COTTRI MB was properly performed. From this fitting, it was found that the start timing of the internal-trigger data corresponded to 2 μs in Figure 5.14.

The RECBE data had no missed event in analysed events here, so the COTTRI-MB data was also compared with the RECBE data. It is difficult to reproduce the

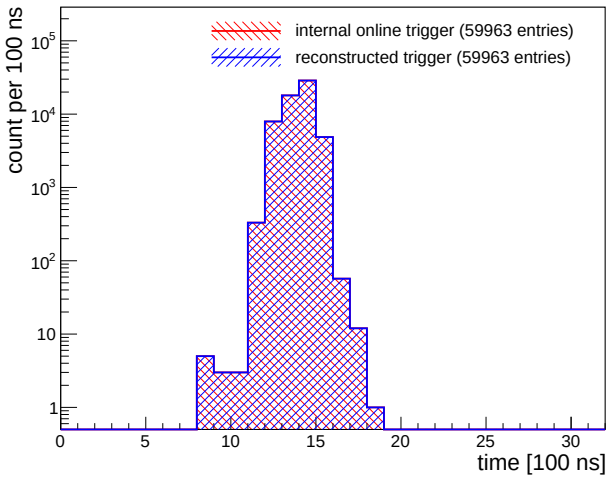

Figure 5.18: Comparison between the internal online trigger and the reconstructed trigger timing. The internal online trigger is generated by the COTTRI MB, and the reconstructed trigger is an offline trigger produced by using the data from the COTTRI FEs.

COTTRI-MB data from the RECBE data directly. By using the maximum number of the CDC hits, these data were compared with each other. The maximum number of the CDC hits was calculated by using the COTTRI-MB data, and its distribution is shown in Figure 5.19. There were 276 events with no CDC hit. This result is

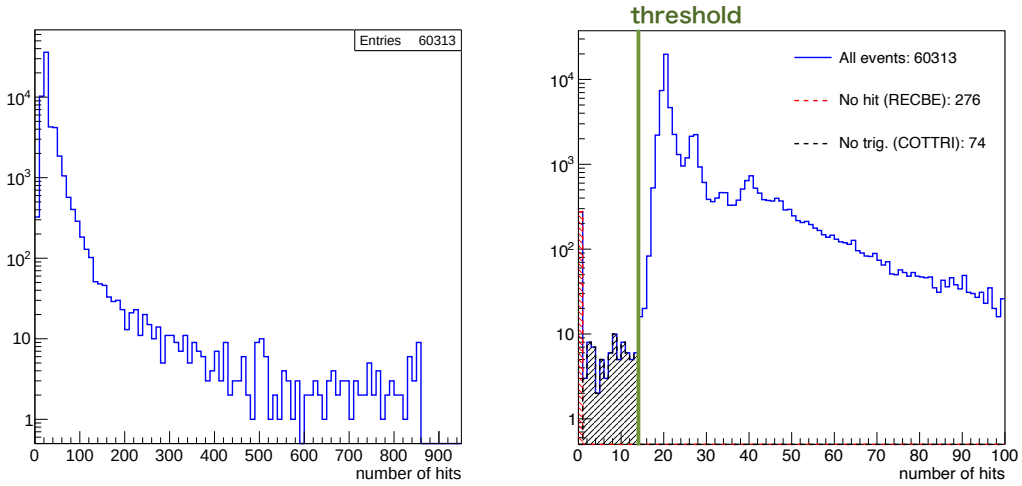

(a) (b)

Figure 5.19: Distribution of the maximum number of the CDC hits. (a) shows the full-range distribution of the CDC hits. (b) shows the comparison of the distribution between the COTTRI MB and RECBE data. No-hit events in the RECBE data are filled in the red dashed histogram. No-internal-trigger events in the COTTRI-MB data are filled in the black dashed histogram. The applied threshold of 14 hits for the event classification is the green line. The triggered events are separated well from the non-triggered events by the threshold.

consistent with the result in Figure 5.16. These events were caused by the accidental

coincidence of the timing counters. 74 events were not triggered by the COTTRI system. As a result, 59963 events remained. The threshold of 14 hits for the event classification correctly worked for making the trigger decision.

Chapter 6

COMET Phase-I Simulation

Simulation of the COMET Phase-I experiment was carried out to estimate the performance of the COTTRI system in the physics measurement. This chapter describes the simulation methods, the simulated data, and the CTH trigger acceptance.

6.1 ICEDUST framework

The Integrated COMET Experiment Data User Software Toolkit (ICEDUST) is a code for experimental data analysis, detector calibration, and simulation of both the Phase-I and Phase-II experiments. This software is based on the Geant4-based framework of ND280, which is the near detector for the T2K experiment [52]. Figure 6.1 shows the ICEDUST framework. The pion production target simulation can

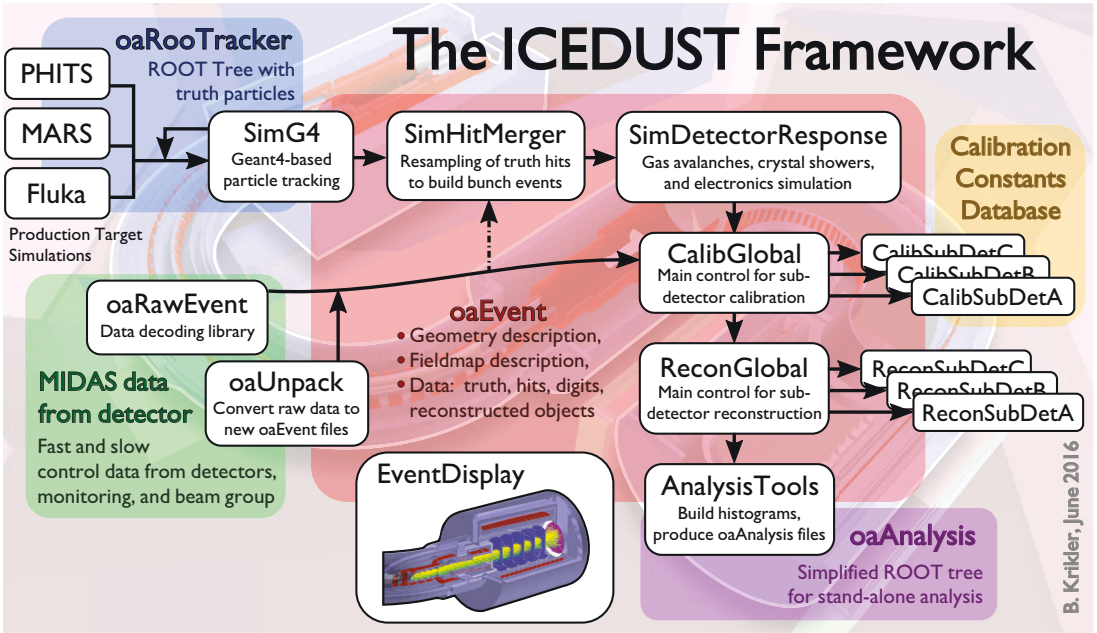

Figure 6.1: Diagram of the ICEDUST framework [19].

be done by Geant4 [53], PHITS [54], MARS [55], and Fluka [56] because the muon and pion yields at the production target are largely different for different software

code. The simulation works in this chapter was carried out by using three main packages: SimG4, SimHitMerger, and SimDetectorResponse.

1. **SimG4:** starts to simulate a particle with its initial parameters and records information of hits and tracks in a special data format, called oaEvent. Particle trajectories and detector hits are simulated in Geant4. The initial parameters are particle type, position, timing, momentum, and energy.

2. **SimHitMerger:** merges hits and tracks in oaEvent data to make a beam bunch and outputs in the same format.

3. **SimDetectorResponse:** simulates responses of the COMET detectors using the oaEvent data at the detector section.

CalibGlobal, ReconGlobal, and AnalysisTools calibrate and analyse data from the detectors and the simulation. Since MIDAS is adopted for the COMET DAQ system, ICEDUST converts a special data format for MIDAS to oaEvent in order to analyze it in the ICEDUST framework, and oaUnpack works for it.

ICEDUST provides a world that consists of all the equipment including the walls of the COMET experimental hall. The experimental hall clipped by the centre plane of the beamline is drawn in Figure 6.2.

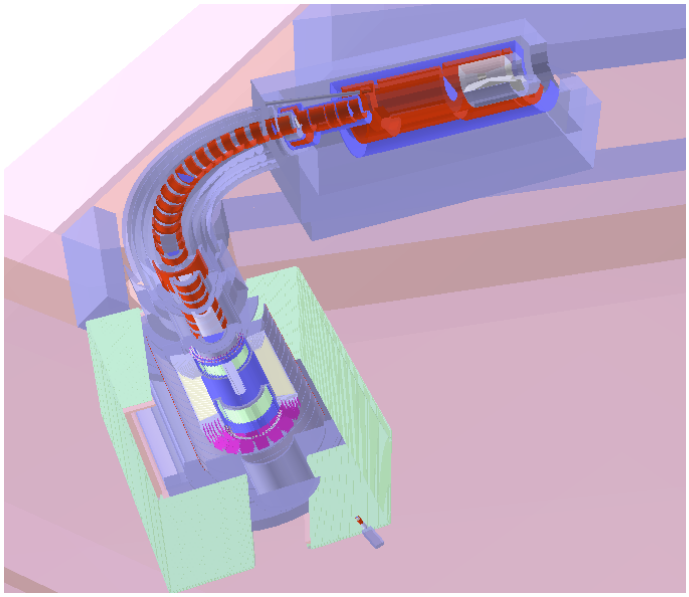

Figure 6.2: Simulated world of the COMET Phase-I experiment. The hall is clipped by the centre plane of the beam line.

6.1.1 Physics list

A physics list for the simulation has to be appropriate for the COMET Phase-I experiment. For the ICEDUST framework, the QGSP_BERT_HP list was selected from the Geant4 physics lists [53]. These lists cover physics processes below 10 GeV and passages of neutrons below 20 MeV. In the COMET experiment, the description of the DIO spectrum is significant because of the intrinsic physics background of the

DIO, as discussed in Section 2.1.1. The physics model in Geant4 does not correctly simulate the high-energy tail of it by default. To reproduce this, the energy of the DIO electrons is taken from its energy spectrum calculated by Czarnecki et al. [28], so far.

6.2 How to simulate bunches

The simulation starts from an 8-GeV proton on the production target in SimG4, and this is processed many times. In SimHitMerger, the timing of events from SimG4 are randomly shifted in the time width of the proton bunch, and these events are merged in a bunch. Then, particle trajectories in a bunch have a realistic timing structure. The time distribution of the tracks has a long tail beyond the bunch separation period of 1170 ns in the detector section due to the delayed background. The trajectories in the bunch tail create non-negligible background hits in the following bunches. In order to take into account this, one-bunch events are concatenated every 1170 ns for each to form "bunch-train" events. The last bunch in bunch-train holds particle trajectories and hits in tails of the other forward bunches.

The first step in SimG4 can start not only at the production target but also everywhere an event monitor is located. If the beam profile in a monitor is recorded in SimG4, the simulation starts at this monitor place, and resampling can be applied for the mass-production of the simulation data. For resampling, initial parameters of a start particle are decided by that of the beam profile, which is described by an 8D histogram of particle's parameters at a start point: three positions, timing, three-momentum, and energy information for each particle type. The number of particles is given by a frequency histogram, which records how many particles are in each event. Changing a random seed for every event makes it possible to generate unique events that are different from each other.

6.3 Background event simulation

In this study, the simulation starts at the beginning of the transport solenoid. The data equivalent to 1.92×10^9 proton-on-target (POT) was simulated by applying the resampling technique. A bunch event in the COMET Phase-I experiment consists of 1.6×10^7 POT; the total number of reproduced single bunches is 18435. The bunch-train events were generated by merging them.

6.3.1 Bunch parameters

To get more realistic data, the pulse beam structure was simulated with three parameters: the bunch period of 1170 ns, the bunch width of 100 ns, and the proton-beam intensity of 1.6×10^7 POT. The arrival time of the proton beam at the production target was defined to be $t = 0$. Single-proton events were merged by shifting the timing of each proton with a uniform distribution from -50 ns to +50 ns. The length of the bunch-train was determined by estimating how bunch tails contribute to the increase in background hits.

First, simulating single bunches was carried out, and the features of detector hits were checked. Figure 6.3 illustrates the CTH and CDC hit timing distributions. In

this figure, drift time in the CDC cell is not considered. In the CTH, the number of

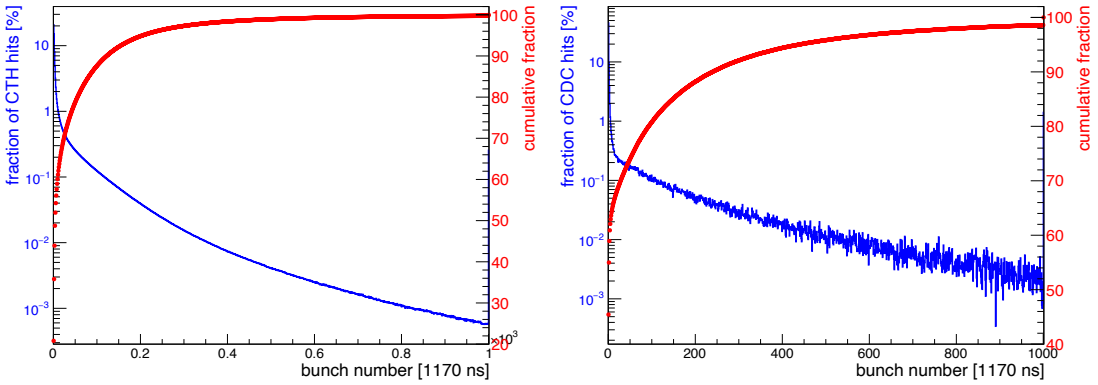

(a) CTH (b) CDC

Figure 6.3: (a) CTH and (b) CDC hit timing distribution for 1000 bunches. Here, each energy deposition of a particle is recorded as a hit. The x-axes are time from the proton-bunch timing, and 1 bin corresponds to the proton bunch separation period of 1170 ns. The largest bin in the histograms includes overflowed hits in the x-axis range. The blue histograms, corresponding to the left axes, show the fraction of hits normalised by the number of total hits. The read graphs, corresponding to the right axes, shows the cumulative fraction of the normalised number of hits from the proton-bunch timing.

hits in the first bunch timing is 20.8% of all the hits, and the number accumulated within 1000 bunches is 99.7% of all. In the case of the CDC, the number of first-bunch hits is 45.4%, and the number accumulated within 1000 bunches is 98.6%. These results show the background level at the detectors immediately increases after the start of the beam extraction and becomes several times larger than the one of the first bunch. What particles make the tail are shown in Figure 6.4. In the COMET experiment, a large amount of neutrons is produced, and they live long while reacting with other substances. Especially, the muon target, the downstream duct flange, and the wall of the experimental hall are big sources of neutrons close to the detector section. Scattering nuclei, these neutrons can indirectly create hits in the CTH. Scattered protons and other heavy particles dominantly make the tail hits. Gamma rays from neutron capture processes generate electrons at the CTH support structures, and they hit the counters. The tail of the CDC hits is mainly composed of electron hits. The electrons are generated by Compton scattering at the CDC end-plates and the CTH support structures. This means that neutrons are also parent particles to make CDC background hits over time.

From these results, the length of the bunch-train was decided to be 1000 bunches for this study. Considering the drift time in a CDC cell to calculate electric signal timing on a wire, hits in a bunch possibly contribute to the signals in the next bunch. For a targeted bunch, a time window of a saved event is set from -700 ns to 1600 ns. In this window, 0 ns is the proton-bunch timing of the target bunch. The bunch-train is produced by rotating a set of all the events to use single bunch events efficiently. Then, in order not to use data of an event several times for different bunch-train events, this set is shifted by two events for each. An image of the bunch-train simulation is drawn in Figure 6.5. Figure 6.6 shows the case where the

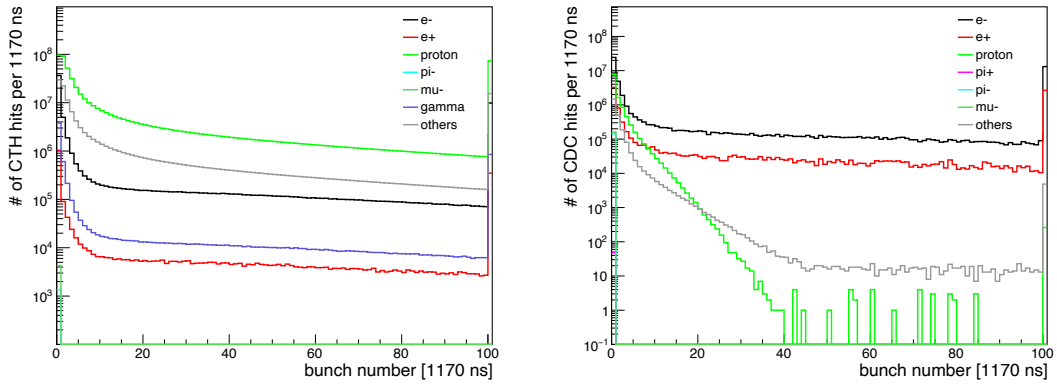

(a) (b)

Figure 6.4: (a) CTH and (b) CDC hit timing distribution of each particle type for 1000 bunches. Here, each energy deposition of a particle is recorded as a hit. 1 bin of the x-axis corresponds to the proton bunch separation period of 1170 ns. The largest bin in the histograms includes overflowed hits in the x-axis range. The correspondence between line colour and particle name is shown in the legend of each figure. The 'others' particle name refers to heavy particles, such as alpha, triton, and heavy ions.

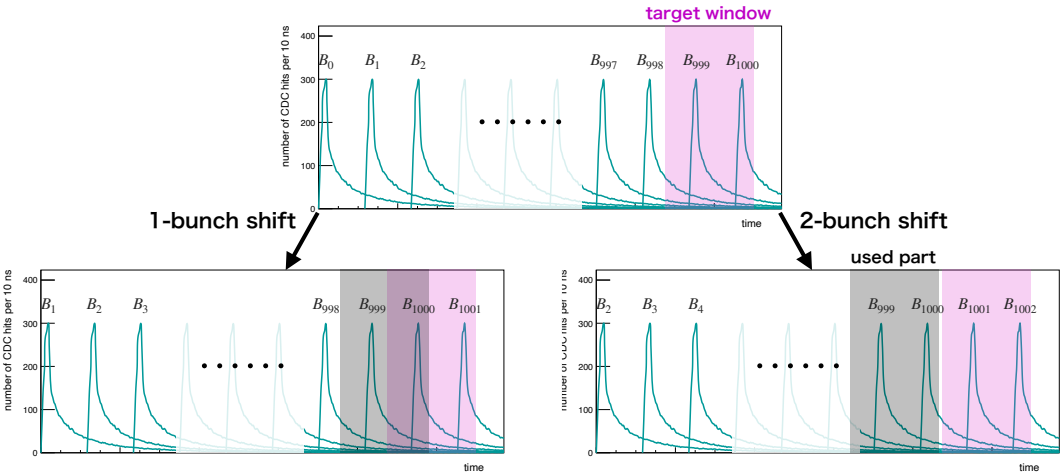

Figure 6.5: Image of the bunch-train simulation. The upper plot shows a set of 1000 events. The left and right lower plots show the event sets in the one-bunch and two-bunch shift cases, respectively. B_i is a bunch ID. Due to the long target window, the target window (magenta) and a used part (gray) overlap each other in the one-bunch shift case.

length of the bunch-train is ten bunches. As a result, 9215 bunch-train events were successfully produced. Figure 6.7 shows the difference in the hit timing distribution between before and after making a bunch-train.

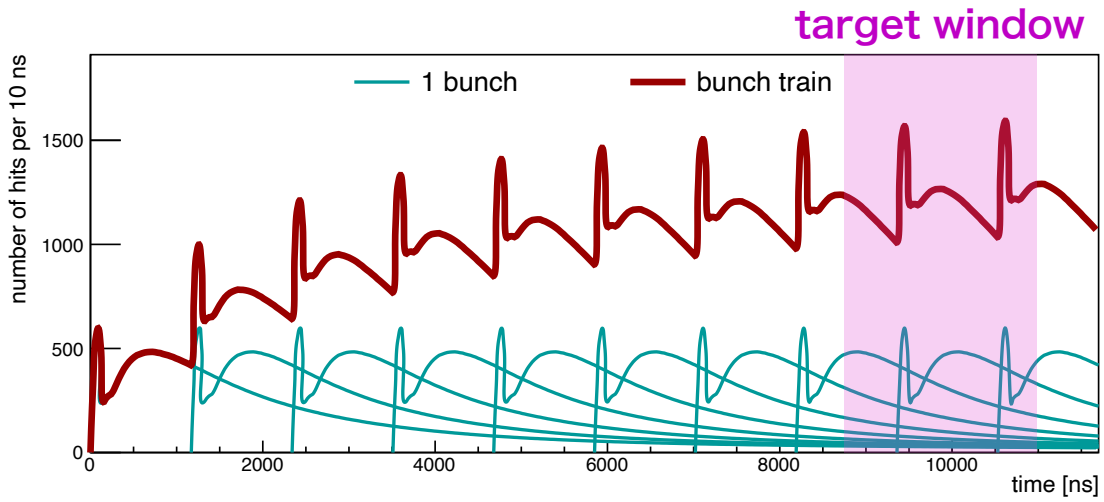

(a) CTH

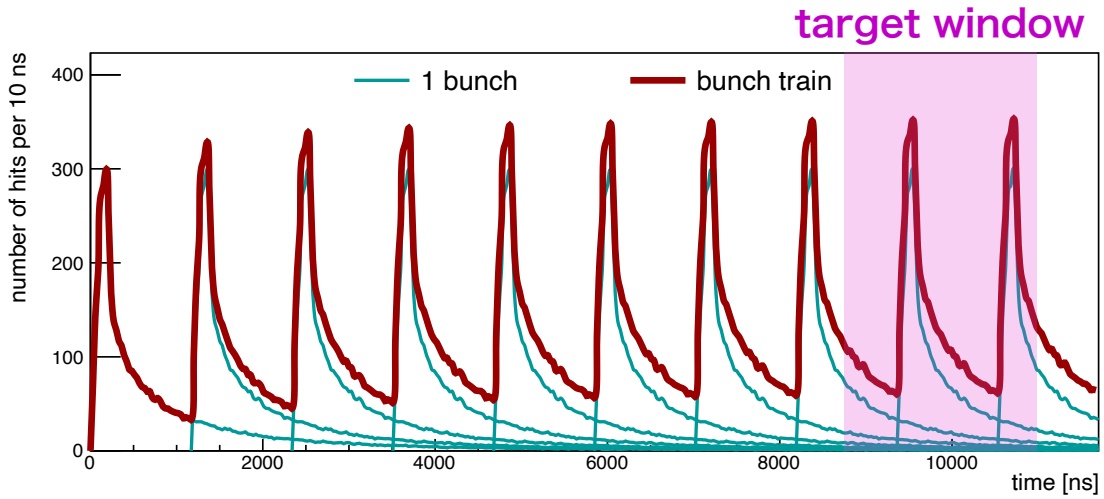

(b) CDC

Figure 6.6: Example of the bunch-train technique. The magenta area is a target window where hits are saved to analyse.

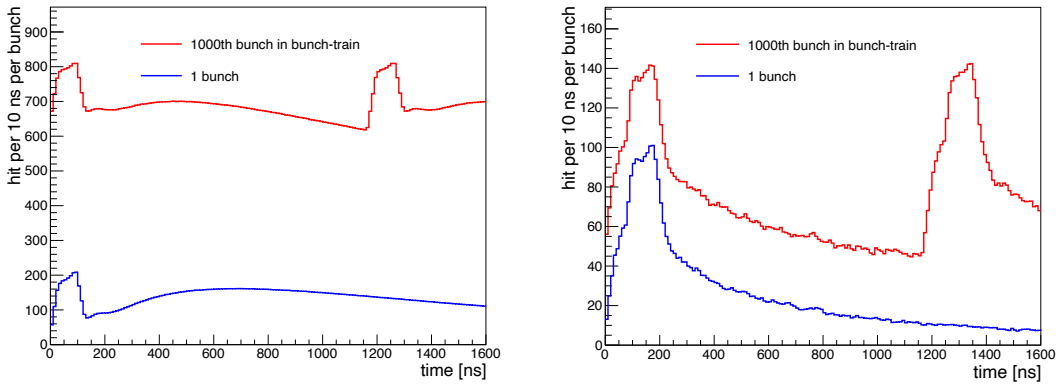

(a) CTH (b) CDC

Figure 6.7: Comparison of hit timing distribution between before and after applying bunch-train. Here, each energy deposition of a particle is recorded as a hit.

6.4 105-MeV signal electron simulation

The target physics process in the COMET experiment is the $\mu \to e$ conversion, which has never been observed. From this process, a mono-energetic electron of 105 MeV is emitted. Therefore, Geant4 doesn't provide this physics process, and the conversion electron is simulated separately from the background events. Simulating conversion-electron events start from the emission of 105-MeV electrons from the muon stopping disks. The start point of an electron is determined by the distribution of the muon stopping position at the disks, as shown in Figure 6.8. The muon lifetime of 864 ns

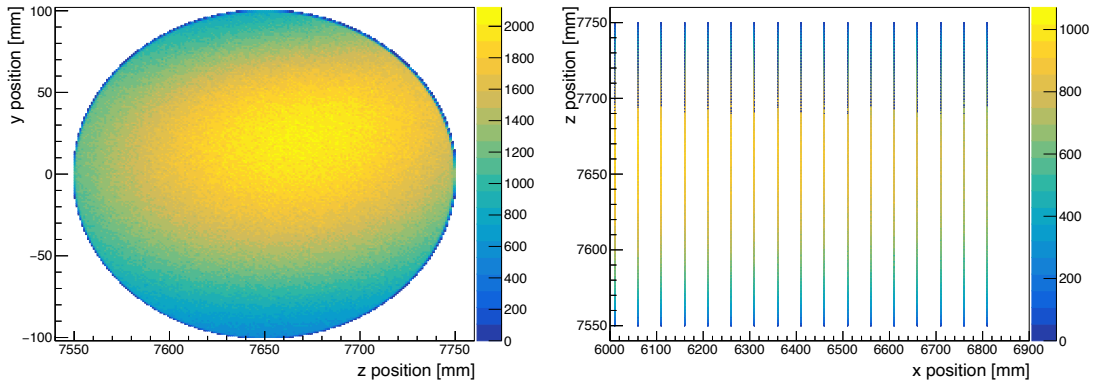

(a) Y-Z plane (b) Z-X plane

Figure 6.8: Distribution of the muon stopping position at the muon stopping target disks. In the plots, titles of the axes show the coordinates in the ICEDUST framework. The x-axis is the muon beam direction; the y-axis is the vertical direction to the floor; the z-axis is the horizontal direction to the floor.

in an aluminium atom gives the distribution of the electron-emission timing. By applying this and the bunch structure, 10^6 conversion electrons were simulated in the time window from 0 ns to 1170 ns. Figure 6.9 illustrates the incident timing of the conversion electrons to the CTH or the CDC. Main peaks are delayed from the

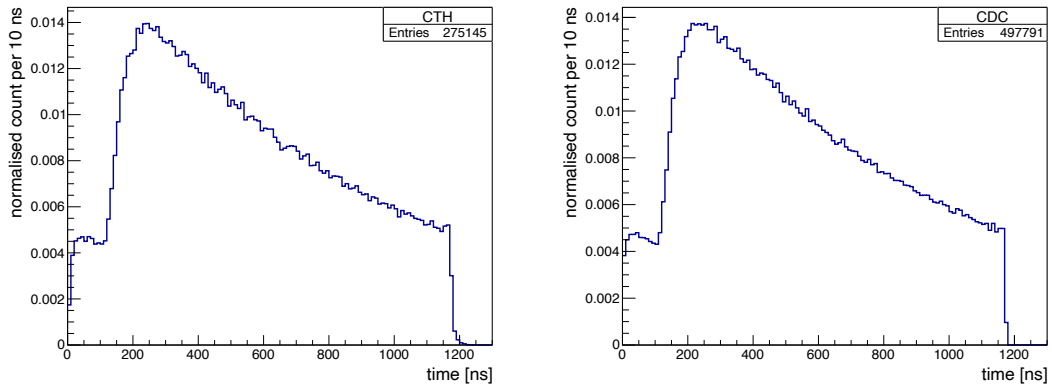

(a) CTH (b) CDC

Figure 6.9: Distribution of the incident timing of the conversion electrons to (a) the CTH or (b) the CDC. 10^6 conversion electrons were simulated, and the histogram shows events that the electrons reach to the CTH or the CDC.

proton bunch timing because of the transportation time from the pion production target to the muon stopping target. As described in Figure 2.7, no CTH module is placed in the centre of the CyDet, and the counter length is limited to be 30 cm; the CTH acceptance is smaller than the CDC acceptance. Figure 6.10 shows an example of the simulated signal track in the CyDet. This electron is emitted from the muon target and hits both the CDC and CTH.

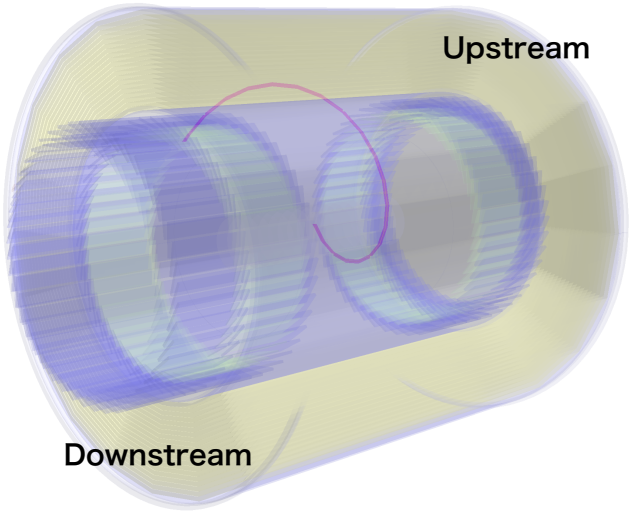

Figure 6.10: Example of the simulated signal track. The yellow region is the CDC. The green and blue boxes are the CTH counters. The magenta line is the trajectory of the 105-MeV electron.

6.5 CTH trigger acceptance

The central trigger system, the FC7, considers both the CTH and CDC trigger to take events of the 105-MeV electron. The main purpose of the CTH is to separate electron events from others with coincidence between scintillation and Cherenkov counters. The four-fold coincidence is applied to reduce the fake trigger rate of the CTH. Here, three sets of counters in the azimuthal direction were considered for the coincidence method. It is required that at least two scintillation counters and two Cherenkov counters ring for the CTH trigger. Figure 6.11 shows an example of the signal event triggered by the CTH. The CTH trigger acceptance for both signal and background events were estimated.

6.5.1 Parameters

The acceptance is determined by the following five key parameters:

- Start timing of the measurement in a bunch, t_{min}
- End timing of the measurement in a bunch, t_{max}
- Coincidence window for CTH hits, t_W

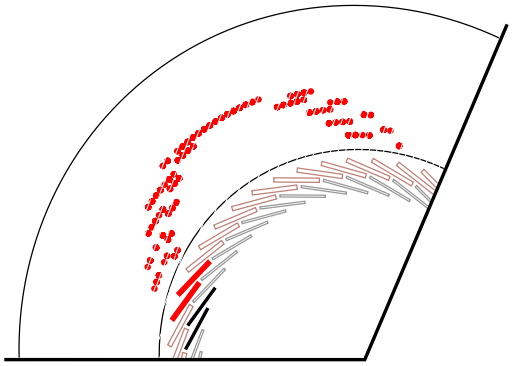

Figure 6.11: Example of the signal event triggered by the CTH. The red dots are signal hit wires of the CDC. The red and black boxes represent the Cherenkov counters and the scintillation counters. The signal track rings two Cherenkov counters and two scintillation counters (filled boxes).

- Energy threshold for hits on the scintillation counters, E_{th}
- Photon threshold for hits on the Cherenkov counters, P_{th}

A longer measurement window leads to larger acceptance and a large background level in a bunch. Therefore, t_{max} is the bunch period of 1170 ns. The coincidence window is better to be as small as possible to reduce accidental coincidence of background hits. To decide the coincidence window, clock frequency for the CTH trigger needs to be taken into account, too. The shared clock frequency is 40 MHz, and the CTH front-end electronics are operated at a 240 MHz clock, which is multiples of 40 MHz. As with the RECBE, the use of a 240 MHz clock allows performing hit time measurement at a clock system equivalent to a 960 MHz clock by applying four clocks out of phase. In this case, ADC chips on the electronics realistically work at 96 MHz; t_W is 10.4 ns at a minimum in the current design. Other parameters – t_{min}, E_{th}, and P_{th} – were optimised to get better signal acceptance.

6.5.2 Signal and Background hits

First, both the energy and photon thresholds were considered to keep the CTH trigger acceptance for the signal events as high as possible.

The number of Cherenkov photons, N, per unit radiator length, x, per unit wavelength, λ, is given by:

$$\frac{dN}{dxd\lambda} = \frac{2\pi\alpha q^2}{\lambda^2}\left(1 - \frac{1}{n^2\beta^2}\right), \tag{6.1}$$

where α is the fine-structure constant, q is the charge of an incident particle, and n is a refractive index. By defining the quantum efficiency of a photon sensor, $QE\,(\lambda)$, the number of detected photons per unit of the radiation length, dN/dx, is given by:

$$\frac{dN}{dx} = \int QE\,(\lambda)\frac{dN}{dxd\lambda}d\lambda = 2\pi\alpha q^2\left(1 - \frac{1}{n^2\beta^2}\right)\int \frac{QE\,(\lambda)}{\lambda^2}d\lambda. \tag{6.2}$$

α, q, and n are the constant values, and the integral part is also fixed by deciding a photon sensor; dN/dx depends only on β. A prototype module of the CTH was irradiated with a 105-MeV electron at Research Center for Electron Photon Science, Tohoku University [57]. As a result of this test, it was found that dN/dx was at least 40 photons/cm for the conversion electron [58]. Now, dN/dx for other β value can be calculated using this number. dN/dx depends on the incident angle of a charged particle, but it was not considered here. Furthermore, the efficiency of photon transport from a hit point to the surface of the photon sensor will be investigated in future work. Figure 6.12 shows the distributions of β and the number of Cherenkov photons for the 105-MeV electrons. β values for the electrons are high enough for

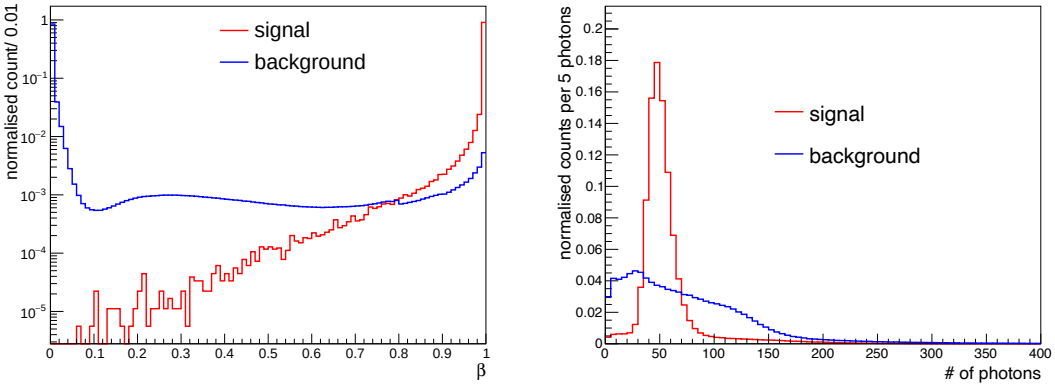

(a) β (b) Cherenkov photons

Figure 6.12: Distribution of β and number of Cherenkov photons for the 105-MeV electrons. Each histogram is normalised by its area.

the β threshold of 0.67. By using β and the track length, the average number of photons was calculated. The number of photons is given by a Poisson distribution whose mean value is this average number. The photon-number distribution of the conversion electron is sharper than one of the backgrounds that have a long tail in the direction of the number of photons.

Figure 6.13 shows the deposited energy distribution of the 105-MeV electrons on the scintillation counters. By using the scintillation efficiency of EJ-230, which is about 9700 photons/1-MeV e^- [38], the deposited energy can be converted to the average number of photons. The number of photons on scintillation counters is dedicated to the Poisson distribution as well as Cherenkov counters. However, due to the large scintillation efficiency, it is expected that the shape of the energy loss distribution is not changed by this function. Thereby, even if the absolute number after converting to the number of photons is not corrected, shifting a threshold value provides a similar signal-background separation with the one before the conversion. The use of the deposited energy, to estimate the CTH acceptance, was decided here. An energy threshold is applied to cut the background hits.

6.5.3 Signal and Background acceptance

With reference to the above distributions, E_{th} and P_{th} were decided to be 650 keV and 10 photons, respectively, to keep the CTH trigger acceptance for the signal events as high as possible. In this study, both four-fold coincidence of the CTH

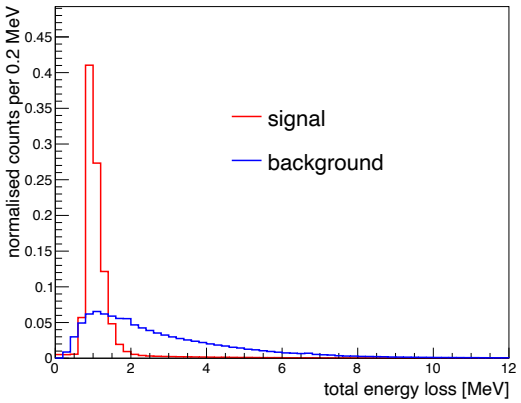

Figure 6.13: Distribution of the energy-loss on the scintillation counters. The red line is at 650 keV

counters and at least a CDC hit were required for the trigger. Figure 6.14 shows the measurement-window dependence of the CTH trigger acceptance for the 105-MeV electron event and the background trigger rate. The signal acceptance is 18.3%

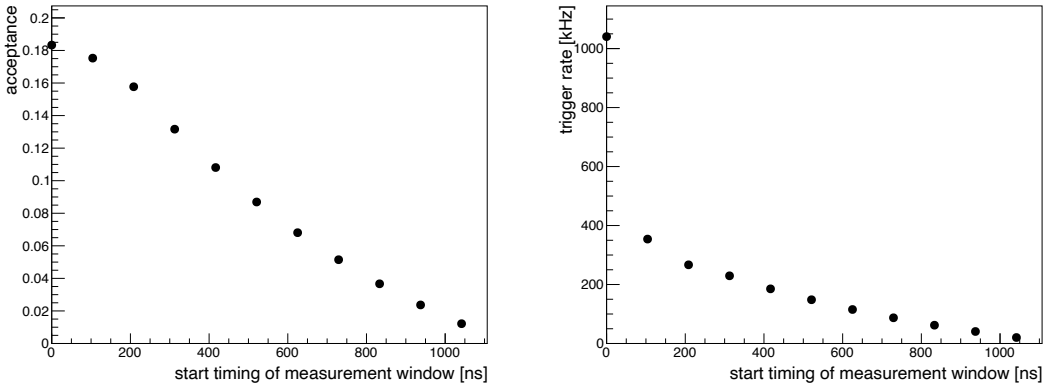

(a) Signal acceptance (b) Fake trigger rate

Figure 6.14: (a) CTH trigger acceptance for the signal events and (b) CTH background trigger rate. The x-axes are the start timing of the measurement, t_{min}. The acceptance and rate for each $t_{min} = 10\,t_W$ are calculated.

at maximum and decreases as t_{min} increases. As a result, the total geometrical acceptance of the CTH is 18.3%. This requires:

- the CTH hits of the conversion electron satisfy with the four-fold coincidence within $t_W = 10.4$ ns and
- the conversion electron creates at least one hit in the CDC.

By changing t_{min}, the CTH acceptance was calculated for each time window of measurement. Even if t_{min} is 937.5 ns, the background trigger rate is 41 kHz for the signal acceptance of 2.4%. This rate is unacceptable to operate the DAQ system stably, as discussed in Section 2.4.2. With the CDC-hit information, the COTTRI system improves the trigger performance and suppress this trigger rate.

The signal efficiency of the CTH online trigger discussed here is summarised in Table 6.1. The time window for the measurement is designed to be 700 ns to 1170 ns. The measurement-window efficiency was calculated to be 5.6% in total from the result in Figure 6.14.

Table 6.1: CTH online trigger efficiency.

Geometry	18.3%
Measurement window	30.6%
Total	5.6%

Chapter 7

Detector response simulation

The ICEDUST produces the hit-timing and deposited-energy data in the CDC. These data were converted to realistic data handled on the RECBEs in order to evaluate the performance of the online trigger system. The sequence from particle hits to data processing on the RECBE was simulated in the following three steps:

1. calculation of total ionization number,
2. calculation of induced signal charge, and
3. calculation of ADC counts.

The RECBE performance was measured in an experimental setup to decide a conversion factor from the signal charge to ADC counts. This chapter describes the RECBE performance and the processes for simulating the detector response.

7.1 Evaluation of the RECBE performance

Before the data simulation, the waveform recorded on the RECBE was tested in a lab. It is to obtain a function for converting the charges to the ADC counts.

7.1.1 Experimental setup

For the performance evaluation, the input charge needs to be clearly known and should be changeable to scan a wide input range. A function generator meets these requirements. The measurement setup using a function generator is drawn in Figure 7.1. The adapter board seen in Figure 5.5 was utilised, and its capacitor of 1 pF was replaced by 10 pF to inject a larger input charge. LEMO connectors were implemented on the RECBE board to input a clock signal and a trigger signal from the function generator in stand-alone operation. The data was taken by a DAQ PC through an optical media converter and a switching hub. A pulse-height setup of the function generator was changed from 50 mV to 10000 mV in 50 mV steps; the input charge was ideally set to be 0.5 pC to 10.0 pC in 0.5 pC steps. However, the input pulse was attenuated before reaching the capacitor on the RECBE. The pulse height on the capacitor was measured using an oscilloscope to evaluate this attenuation level. Figure 7.2 shows the relationship between the setup value of the function generator and the pulse height on the capacitor. As a fitting result, it was

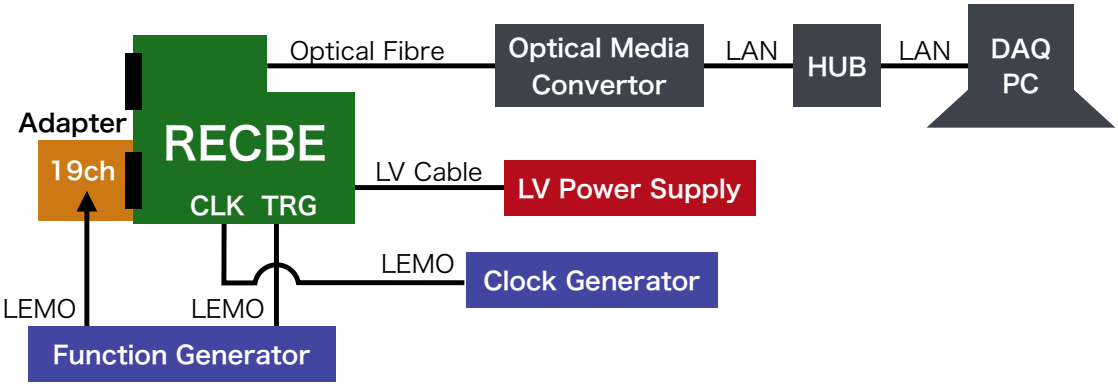

Figure 7.1: Experimental setup for charge-to-ADC calibration test.

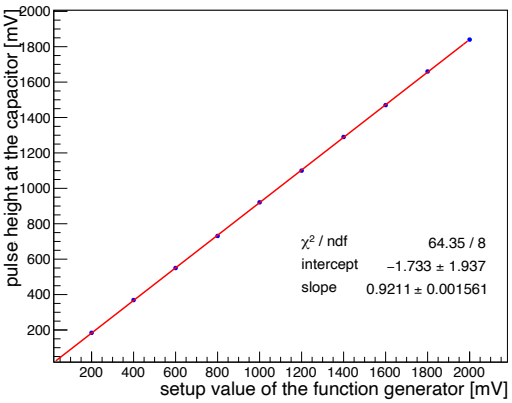

Figure 7.2: Input pulse height calibration on the adapter board. Data points (blue dots) are fit with a linear function (read line).

found that the relationship was given by:

$$\text{(Pulse height at the capacitor [mV])} = 0.92 \times \text{(Function generator setup [mV])} - 1.73. \tag{7.1}$$

Assuming that this relationship was conserved over 2000 mV of the setup values of the function, it was linearly extrapolated. Then, the test range of input pulses was 0.5 pC to 0.92 pC.

7.1.2 Waveform shaping

Figure 7.3 shows the waveform recorded by the RECBE. Due to the low sampling speed of 30 MSPS on the ADC chip, the waveform does not appear to be smooth. By using a function generator, the timing of the input signal can be synchronised with the trigger timing. The RECBE measures signal timing at 960 MHz; the recorded waveform can be smoothed by using this timing information if both signal and trigger lines come from the same function generator. The waveform after smoothing is shown in Figure 7.4. Several samples in the undershoot region look strange. However, only the samples over a baseline were considered. That strange undershoot did not affect the result of this measurement. The sampling rate in the offline

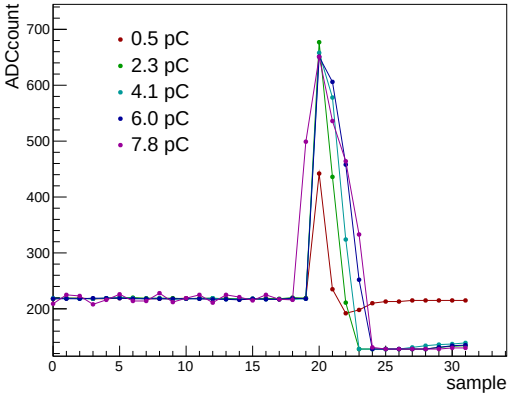

Figure 7.3: Example of waves recorded by the RECBE.

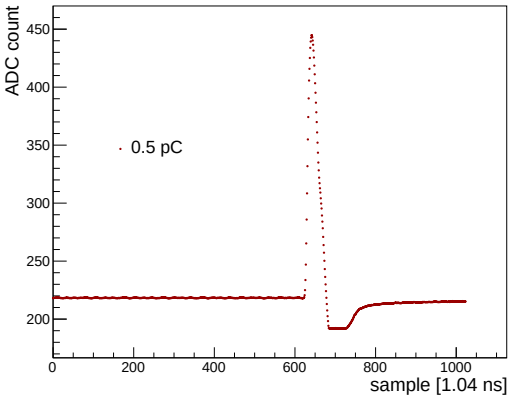

Figure 7.4: Example wave after the smoothing process.

analysis is artificially changed to 960 MSPS thanks to the timing information, and the smoothed waveform is composed of 1024 smoothed samples. The ADC counts of each smoothed sample were integrated over the baseline; a sum of ADC count, called "ADC-sum", was divided by 32 and converted to the number equivalent to the ADC-sum recorded at 30 MHz. That converted ADC-sum is not actually an exact average of the ADC-sum, but it is regarded as an "average" of the ADC-sum here.

7.1.3 Waveform analysis

The low ADC sampling speed also causes that the ADC-sum widely distributes. Also, the ASD amplification saturates if the input charge is too large [35]. So, the integrated-ADC distribution is non-trivial, as shown in Figure 7.5. This distorted distribution makes it difficult to determine the value of the ADC-sum for an input charge. A waveform simulation can solve this issue, but it is difficult due to the avalanche processes in a cell and the complicated behavior of the waveform shaping circuit. Here, it was decided to apply a uniform distribution between the maximum and minimum values of the ADC-sum for each input charge, as the first trial for this type of study in the COMET Phase-I experiment.

The smaller the input charge, the smaller the width of the ADC-sum distribution

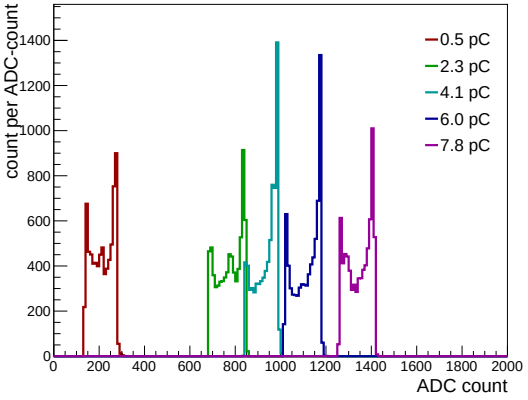

Figure 7.5: Distribution of integrated ADC counts.

should be. In order to consider this, the data of the past measurement [35] where the setup had been similar to this measurement was used. Figure 7.6 shows the average, minimum, and maximum ADC-sum for each input charge. For large input

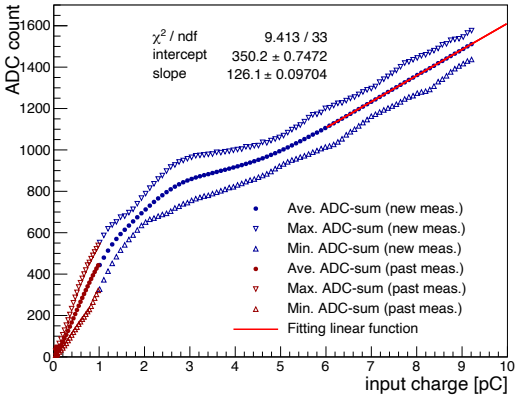

Figure 7.6: Average, minimum and maximum ADC-sum for each input charge.

charge over 9 pC, the relation with ADC-sum has to be extrapolated. The average of the ADC-sum seems to be increasing linearly over around 6 pC. This was fitted with a linear function, and then the conversion function is given by

$$\text{Average ADC} - \text{sum} = 350 \times (\text{Input charge; [pC]}) + 126. \tag{7.2}$$

The minimum and maximum ADC-sum fluctuated in this fitting region. Since the approximation should be as conservative as possible, the maximum width between the minimum and maximum ADC-sum is assumed to be the width between them for all the points. This maximum width was 188 ADC counts. To decide the relationship between the ADC-sum and the input charge, parameter spaces of the input charge were divided by three regions:

- below 1.0 pC, the minimum and maximum ADC-sum from the past measurement;
- from 1.0 pC to 6 pC, the minimum and maximum ADC-sum from the new measurement;

- over 6 pC, ADC − sum − 94 and ADC − sum + 94 for the minimum and maximum ADC-sum, respectively.

The conversion functions defined above are drawn in Figure 7.7. They are applied to

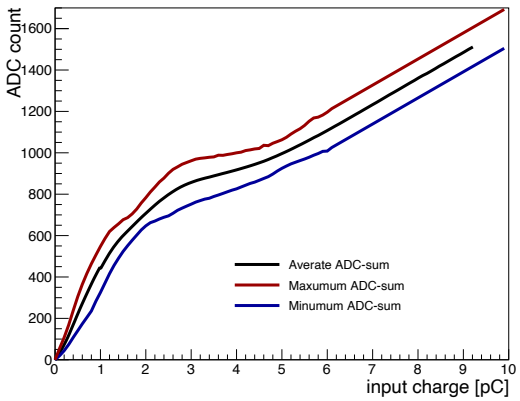

Figure 7.7: Functions for the conversion from input charge to ADC-sum.

determine the uniform distribution of the ADC-sum for each input charge. For each hit timing within 100 ns, the ADC-sum is varied and shared with the next 100 ns sometimes. Its effect is ignored here because the waveform was not considered, and there is no way to get that factor.

7.2 Detector response simulation

The initial inputs for the three steps are CDC-hit timing and deposited energy per a CDC cell given by the ICEDUST simulation, as shown in Figure 7.8 and Figure 7.9.
The simulated data has precise timing resolution, although real data is processed

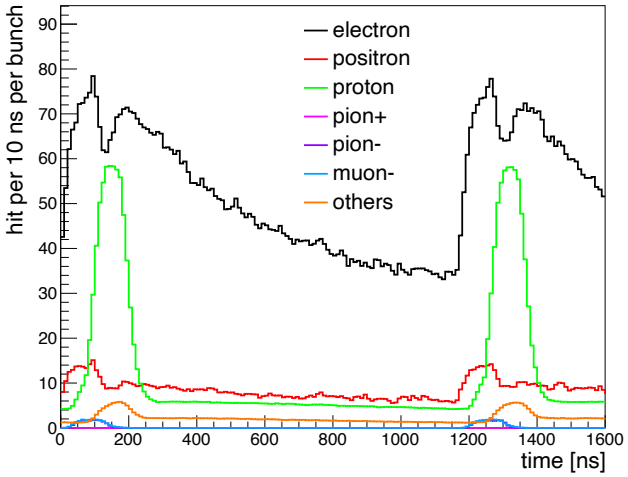

Figure 7.8: Hit timing distribution for each particle. The "others" include heavy particles, such as alpha, triton, and heavy ions.

at a restricted resolution of readout electronics. So, these inputs are progressively

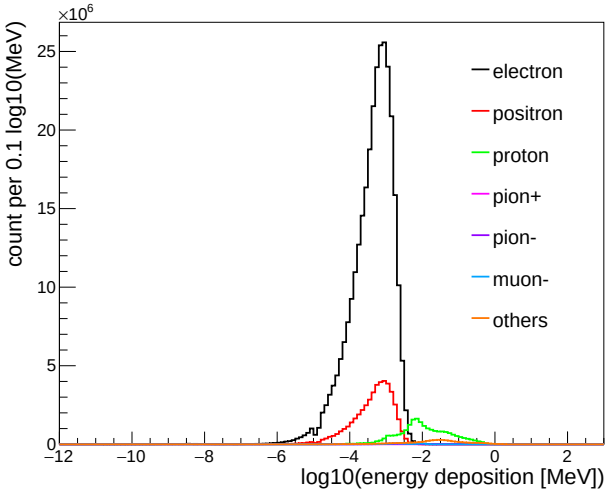

Figure 7.9: Energy deposition distribution of each CDC hit. The "others" include heavy particles, such as alpha, triton, and heavy ions.

converted at a realistic resolution, as shown below. The simulated signal events were merged with the background events to consider background contamination in signal hits.

7.2.1 Position-timing relationship

The CDC-hit timing provided by ICEDUST is not included drift time in a cell; drift time distribution for the filled gas of He$-i$C$_4$H$_{10}$ (90:10) needs to be considered. The details of the CDC performance is under investigation. At a cell corner, it is not easy to understand the drift time distribution due to the distortion of an electric field. In addition, the cross-section of a CDC cell in ICEDUST is a rectangle so far, although the stereo layer configuration can deform it. In this study, assuming that the cell cross-section is rectangular, the drift time distribution was calculated by using Garfield++, which is a tool to simulate features of gases in gas detectors [59]. Air pressure, temperature, and magnetic field in the CDC were set to be 1 atm, 293.15 K, and 1 T, respectively. The high voltage applied for sense wires was set to be HV=1800 V. Figure 7.10 illustrates the geometrical setup and the electric field. 10^6 primaries were randomly put on a readout cell. 930824 of all reached the readout sense wire, and the others did not reach the wire due to the electric field in the CDC cell and the simulation time cut of 2000 ns. The simulated drift time distribution is shown in Figure 7.11 as a 2-D histogram. From this figure, it was found that some primaries near the cell edge could not reach the sense wire. In that case, the drift time of those primaries was set to be the maximum drift time in the histogram.

7.2.2 Calculation of total ionization number

The RECBE handles ADC data every 100 ns in the COTTRI system. The total energy loss within 100 ns is calculated first. Figure 7.12 shows the total energy loss in a CDC cell within 100 ns. As explained in Chapter 3, the COTTRI system uses three continuous wires, a local and two neighbouring wires, in a layer for trigger

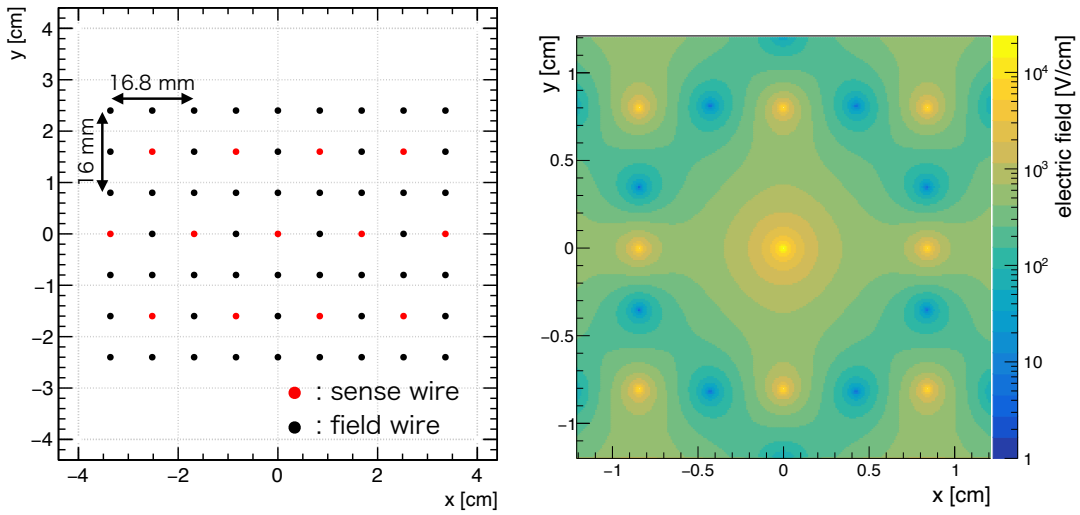

(a) Geometrical setup (b) Electric field

Figure 7.10: Cell configuration for the Garfield++ simulation. (a) shows the cell configuration, and (b) shows the electric field each position at 1800V.

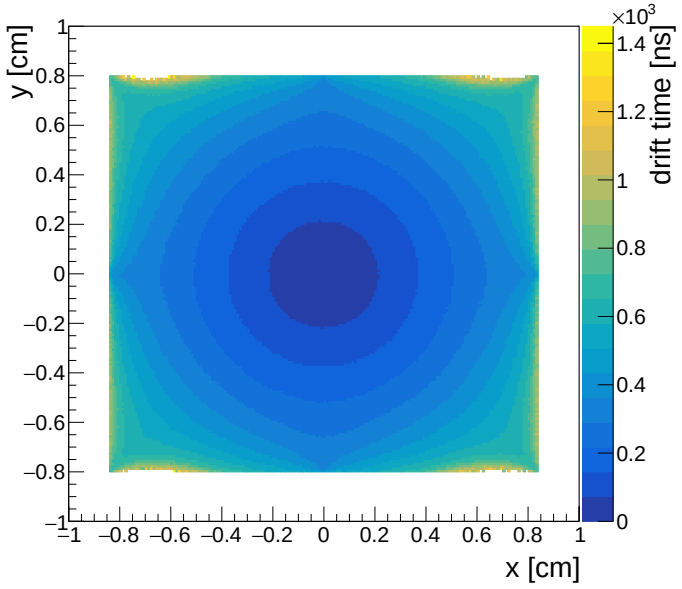

Figure 7.11: 2-D distribution of the drift time.

procedures. Thereby, the distribution of the total energy loss in neighbouring cells is also checked in Figure 7.13. As compared to the local cell, the fractions of proton and "others" hits are small in the neighbouring cells. This is because most of these heavy particles pass through the CDC from inside to outside. Electrons and positrons make cluster hits in the CDC, and therefore, a fraction of those hits in the neighbours is kept to be large. As a result, the large deposited energy of proton or other hits in the neighbours is suppressed, and the deposit energy distribution of background hits is more similar to the one of signal hits than the case of local hits. Based on this energy information, the number of total ionization was calculated.

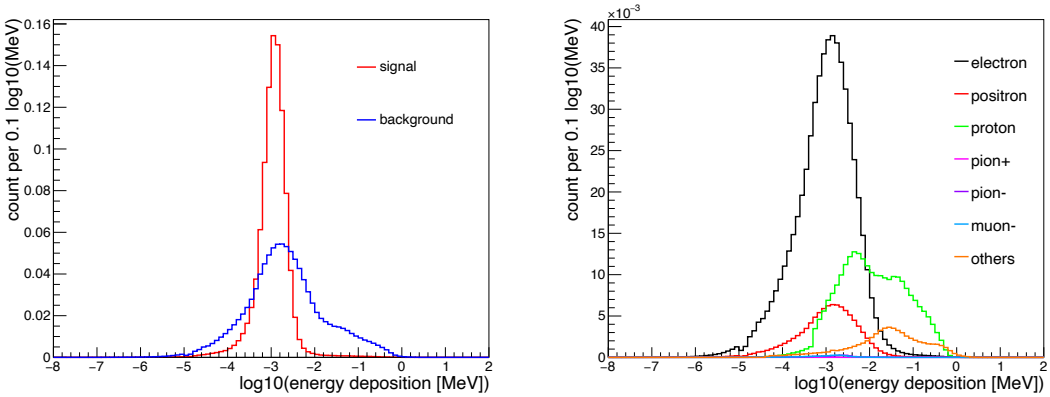

(a) (b)

Figure 7.12: Energy deposition distribution in the local cell within 100 ns. In panel (a), signal and background distributions are compared. Both histograms are normalised by the areas. In panel (b), the distribution is compared by particles. Particles that hit the earliest with a width of 100 ns are labeled. All the histograms are normalised by the total area of all. The "others" include heavy particles, such as alpha, triton, and heavy ions.

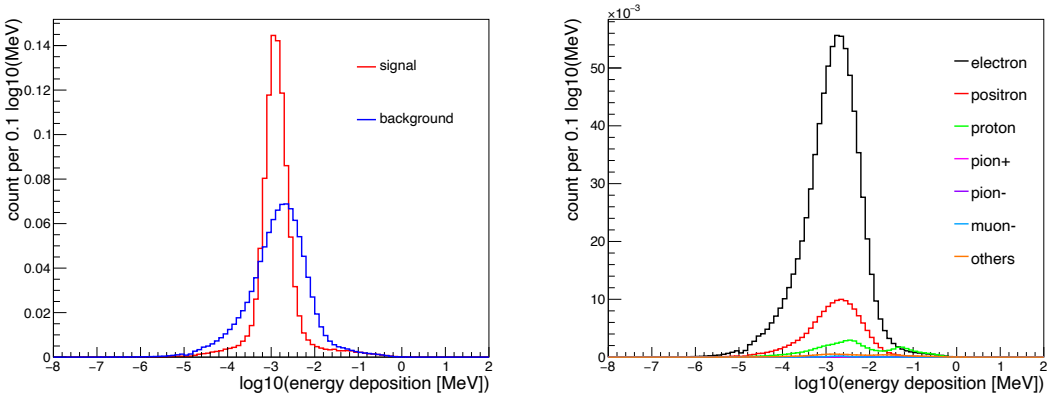

(a) (b)

Figure 7.13: Energy deposition distribution in the neighbouring cells within 100 ns. The histogram is only filled with non-zero values of the deposited energy in the neighbouring cell if the local wire has a hit. In panel (a), signal and background distributions are compared. Both histograms are normalised by the areas. In panel (b), the distribution is compared by particles. Particles that hit the earliest with a width of 100 ns are labeled. All the histograms are normalised by the total area of all. The "others" include heavy particles, such as alpha, triton, and heavy ions.

The number of total ionization per unit length dN_t/dx is given by:

$$\frac{dN_t}{dx} = \frac{1}{W_m}\left(\frac{dE}{dx}\right)_m = \frac{p_h}{W_h}\left(\frac{dE}{dx}\right)_h + \frac{p_i}{W_i}\left(\frac{dE}{dx}\right)_i \tag{7.3}$$

where suffix m, h and i represent the mixed gas, helium gas, and isobutane gas, respectively; dE/dx is energy loss for minimum ionizing particles in a CDC cell; W is average energy for the production of an electron-ion pair; p is the percentage of each gas component [60]. For the helium gas, $(dE/dx)_h$ is $0.32\,\mathrm{keV}\cdot\mathrm{cm}^{-1}$, W_h is

41.3 eV, and p_h is 90% [7]. For the isobutane gas, $(dE/dx)_i$ is 5.67 keV $\cdot$ cm^{-1}, W_h is 26 eV, and p_h is 10% [7]. Then, W_m is 29.7 eV. This value was applied to the calculation of the mean value of the total ionization number in this study. In this way, the energy loss in Figure 7.12 was converted to the number of total ionization, as shown in Figure 7.14.

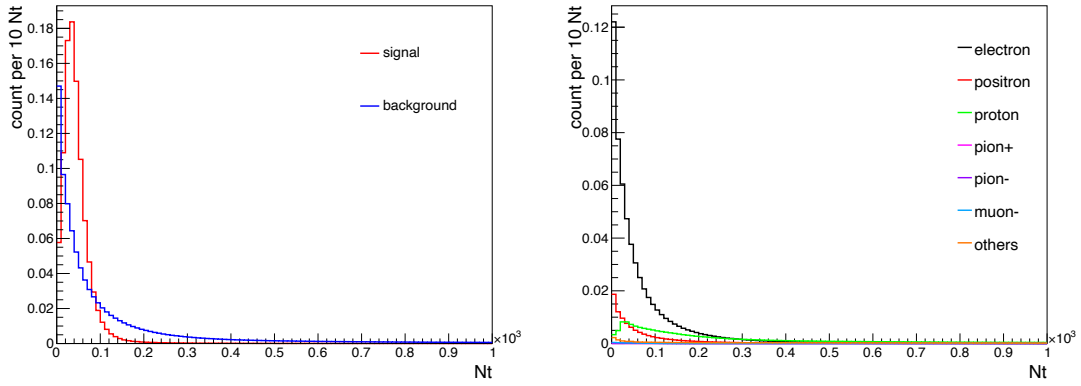

(a) (b)

Figure 7.14: Distribution of the total ionization number. In panel (a), signal and background distributions are compared. Both histograms are normalised by the areas. In panel (b), the distributions are shown for different particles. Particles that hit the earliest with a width of 100 ns are labeled. All the histograms are normalised by the total area of all. The "others" include heavy particles, such as alpha, triton, and heavy ions.

7.2.3 Calculation of induced signal charge

Ionised electrons in a cell move to a sense wire while feeling an electric field created by applying high voltage. When getting close to the wire, those electrons cause avalanche amplification and make induced current on the wire. It is difficult to represent this sequence of phenomena by the simulation because ions created near the sense wire affect the induced current; the experimental result of gas gain distribution was adopted for converting the total-ionization number to induced current. An experiment has been performed to evaluate the performance of the CDC using a CDC prototype chamber in July 2015 [61]. The 1-GeV/c electron beam at LEPS of SPring-8 [62] was injected into the prototype chamber. In the experimental data analysis, the gas gain was calculated from the charge information recorded by the RECBE and simulated number of the total ionization. (The measurement result will be published soon.) Thus, it includes complicated processes. So, this experimental result is used to calculate the induced current on a wire. Figure 7.15 shows the gas gain distribution measured in the experiment.

The signal charge was calculated from the number of total ionization by:

$$(\text{Signal charge}) = N_t \times (\text{Gas gain}) \times (\text{Elementary charge})\,. \tag{7.4}$$

The most probable value of the measured gas gain distribution is chosen as the gas gain here. The signal charge distribution is represented in Figure 7.16.

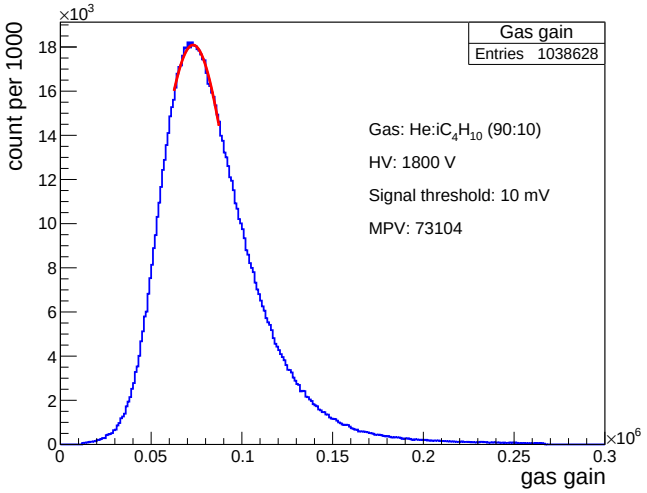

Figure 7.15: Gas gain distribution of the CDC prototype chamber.

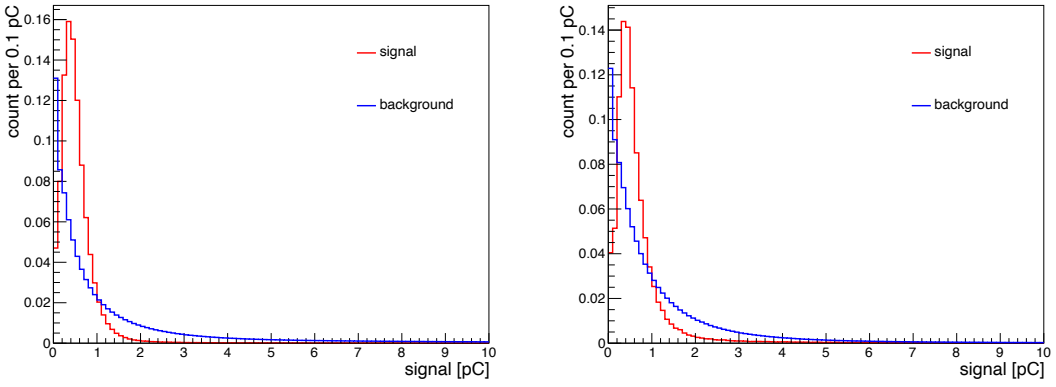

(a) (b)

Figure 7.16: Distribution of the signal charge at the local (a) and neighbouring (b) wires. In panel (b), only non-zero values are filled in the histograms.

7.2.4 Calculation of ADC count

At last, an induced signal charge is detected on the RECBE and converted to ADC counts through the ASD and ADC chips; this conversion depends on the performance of the RECBE, as described in Section 7.1. By applying the functions in Figure 7.7, the ADC counts were calculated from the induced charge. Figure 7.17 shows the ADC-sum distribution.

A large input charge makes too large of an ADC-sum that cannot be accepted by a dynamic range of the ADC-sum within 100 ns. According to the past research [35], an ADC count in a sample saturates at about 450, which corresponds to 880 mV. It is caused by the pulse-height saturation of the ASD analogue output. Then, the maximum of ADC counts integrated into three samples is 1350. Therefore, a large ADC-sum over 1350 must make a tail in the next ADC sample. It was decided that if ADC-sum is over 1350 ADC counts, after subtracting the maximum counts the remaining counts are summed up in the next ADC sample. The RECBE does not record timing data while pulse height is decreasing, so the tail is not regarded as a

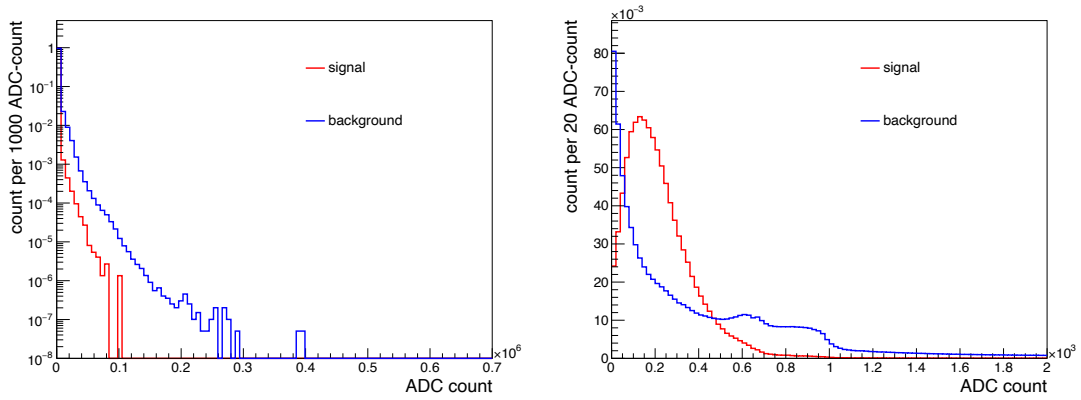

(a) (b)

Figure 7.17: ADC-sum distribution in the full range (a) and the distribution focused on 0 to 2000 ADC-count (b).

hit by itself, and other hits are required to make a hit in the next sample that is contaminated by the tail. Here, the waveform of the ASD analogue output is not considered. Figure 7.18 shows the ADC-sum distribution considered the dynamic range of the ADC-sum. Finally, the ADC-sum processed in the COTTRI system is reproduced.

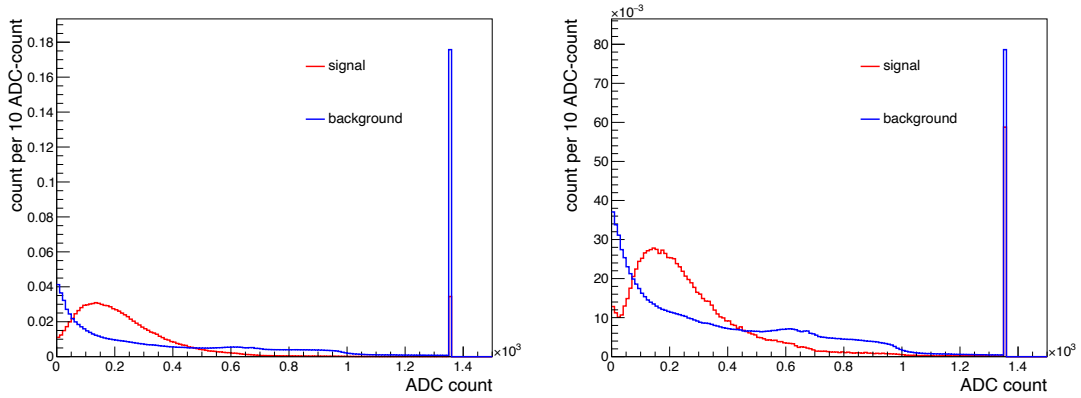

(a) Local wires (b) Neighbouring wires

Figure 7.18: ADC-sum distribution considered the dynamic range of the ADC-sum at the local (a) and neighbouring (b) wires in 100 ns. In panel (b), only non-zero values are filled in the histograms.

Chapter 8

Evaluation of trigger performance

The performance of the online trigger system was estimated by using the simulation data from ICEDUST before the physics measurement starts. This chapter describes the methodology of the COTTRI system for online signal-event recognition.

8.1 Data handling

The hit classification is carried out by using GBDTs and the input features prepared in Chapter 7. The event classifier makes a trigger decision based on GBDT outputs. The performance of them correlates with parameters such as the timing of the measurement window and threshold for ADC counts.

8.1.1 Parameters

Each hit is handled by applying a pre-selection with six parameters.

Pre-processing of hit

- ADC cut for large ADC-sum samples, q_{th}
  - According to Figure 7.18, the ADC-sum of the conversion electron dominantly distributes around 150 ADC counts, but on the other hand, the ADC-sum of the backgrounds distributes even larger ADC counts than it. So, the ADC cut is applied in order to filter the large background ADC-sum.

- Thresholds for the ADC conversion, q^0_{div}, q^1_{div}, and q^2_{div}
  - ADC-sum is converted to 2-bit data, as discussed in Section 4.1.1.

Hit classification in the COTTRI FE

- Integration time for the drift time, t_I
  - A charged particle passing through the CDC causes ionization processes in a short time. However, the timing when a signal of that particle is detected spreads widely due to the position-time relation in a CDC cell. In the COTTRI system, the integration time should be set long enough not to miss conversion electron hits.

Global classification in the COTTRI MB

- Start timing of the measurement in a bunch, t_{min}
  - As discussed in Section 6.5.1.
- End timing of the measurement in a bunch, t_{max}
  - As discussed in Section 6.5.1.

Figure 8.1 and 8.2 illustrate the definition of each parameter. A measurement

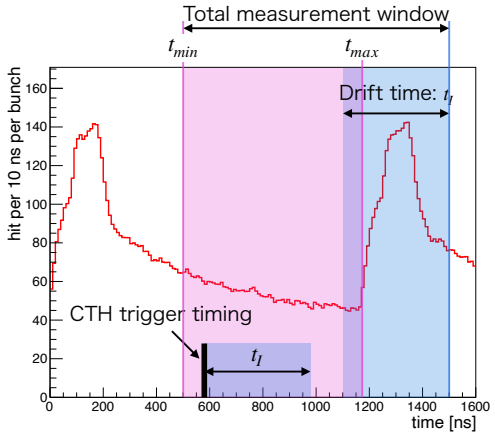

Figure 8.1: Timing parameters in the COTTRI system. t_{min} and t_{max} are the start and end timing of measurement for the CTH trigger. t_I is the integration time for the drift time.

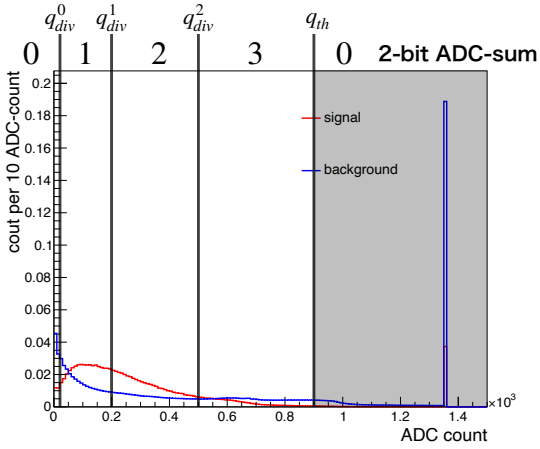

Figure 8.2: Parameters for the ADC data in the COTTRI system. q_{th} and q^i_{div} are thresholds for the ADC cut and the ADC conversion to the 2-bit ADC-sum, respectively, and applied to the summation of three ADC samples on the RECBE.

window in a bunch significantly affects the signal and background acceptance in the physics measurement. Figure 8.3 shows the time variation of CDC hits for $t_I = 400\,\text{ns}$. Compared to Figure 7.8, the first peak corresponding to the beam-related background is delayed by the effect of drift time. For considering this effect, the end timing of the classification period in a bunch is $t_{max}+t_I$. This end timing has

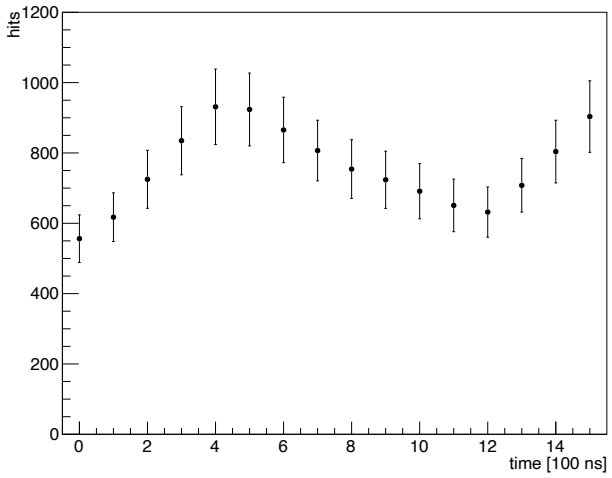

Figure 8.3: Time variation of CDC hits. The horizontal axis is the end of the integration time at each timing. This is the case of $t_I = 400\,\text{ns}$. The error bars represent the root mean square of the hit number distribution in each time bin. A point at 0 ns includes the number of CDC hits in the former bunch.

to be set late enough not to miss the conversion-electron hits, but the backgrounds in the next bunch can deteriorate the classification quality if it is too late. The performance of the ADC cut was also evaluated in Figure 8.4. For example, to

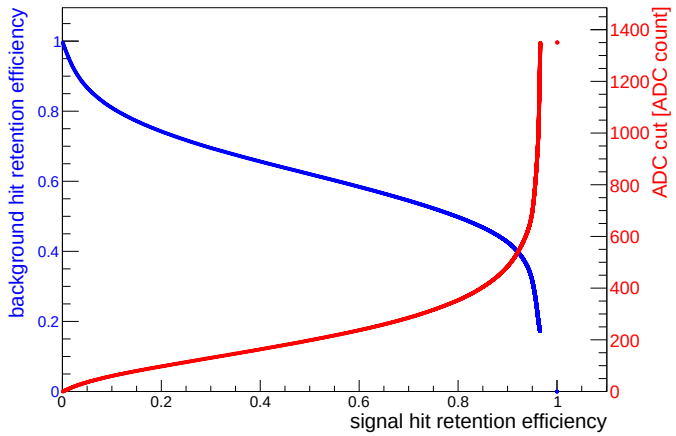

Figure 8.4: Performance of the ADC cut. Comparison between the background-hit retention efficiency and the signal-hit retention efficiency (blue points), The signal efficiency against the ADC cut (red points). This is the case that the measurement windows is 500 ns to 1200 ns.

keep 90% signal-hit efficiency, $q_{th} = 485$, and then the rejection efficiency of the background hits is 57%.

An effect of each parameter can be simply evaluated, but a combination of parameters makes it difficult to evaluate the performance. The GBDT performance is much more complicated than it. Here, to optimise the classification performance, each parameter is scanned in the following sets:

t_{min} : 100 ns to 800 ns every 100 ns

$t_{max} + t_I$: 1300 ns to 1500 ns every 100 ns

q_{th} : 600, 900

(q^1_{div}, q^2_{div}) : (300, 400), (300, 500), (300, 600), (300, 700),(400, 500), (400, 600), (400, 700), (500, 600), (500, 700), (600, 700)

t_I : 300 ns, 400 ns, or 500 ns

The signal events were merged with the background events in each measurement window of (t_{min}, 1170 ns). q^0_{div} is fixed to be 6 ADC counts, which corresponds to a desirable TDC-threshold value of about 10 mV for the TDC cut. t_{max} for the CTH is fixed to be 1170 ns. Then, t_{max} of 1400 and 1500 with $t_I = 300$ provides no motivation for the evaluation because the coincidence between the CDC and CTH trigger with a 100 ns gate is required. So, only feasible combination between t_{max} and t_I was considered: $(t_{max}, t_I) = (1300, 300)$, $(1300, 400)$, $(1300, 500)$, $(1400, 400)$, $(1400, 500)$, and $(1500, 500)$.

8.1.2 Pre-processing of hit

The input features for the hit classification are the radial positions of the CDC hits and the deposited energy in a CDC cell. The case where the measurement window is from 500 ns to 1400 ns is considered in this section.

Radial position

Figure 8.5 shows the radial position distributions. Since the conversion electron

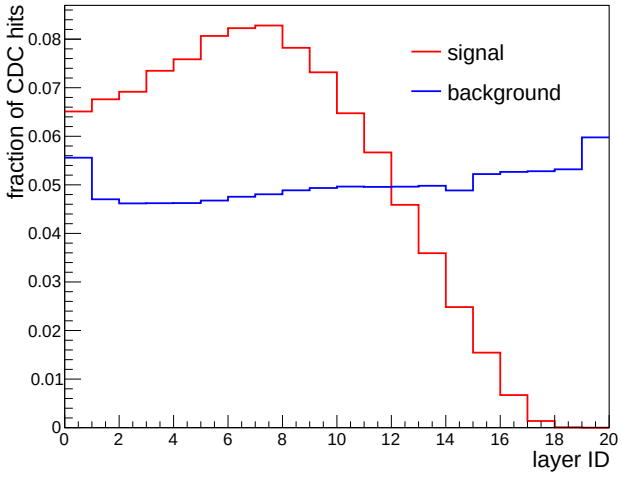

Figure 8.5: Radial position distribution of the CDC hits. The layer ID of 0 is the innermost layer.

of 105 MeV makes a helical track in the 1-T magnetic field, it is difficult for the conversion electron to have hits in the outer layers of the CDC. On the other hand, the background hits are distributed flat. In the innermost and outermost layers, there are more hits than the other layers due to particle reactions at the inner and

outer walls. From the radial position distribution, the hit number of the conversion electrons is negligibly small on the three outermost layers. So, the COTTRI FEs do not connect the RECBEs in that readout section of the CDC, as discussed in Section 3.3. The guard layers are set to eliminate space charge originated from ionization from the CDC wall.

Deposited energy

By applying the parameters, the 2-bit ADC-sum is created for GBDTs. The COTTRI system handles only the 2-bit ADC-sum, but the raw ADC-sum which is not compressed and the 1-bit ADC-sum which is applied only q_{th} are also evaluated. In this chapter, a case of a parameter set is introduced as an example unless otherwise noted: $t_{min} = 500$, $t_{max} = 1400$, $q_{th} = 900$, $(q^0_{div}, q^1_{div}, q^2_{div}) = (6, 100, 500)$, and $t_I = 400$.

First, the ADC-sum is filtered by the ADC cut and compressed into a 2-bit ADC-sum on the RECBE. Figure 8.6 represents the distribution of the ADC-sum compressed into 2 bits on local and neighbouring wires. The COTTRI FEs integrate

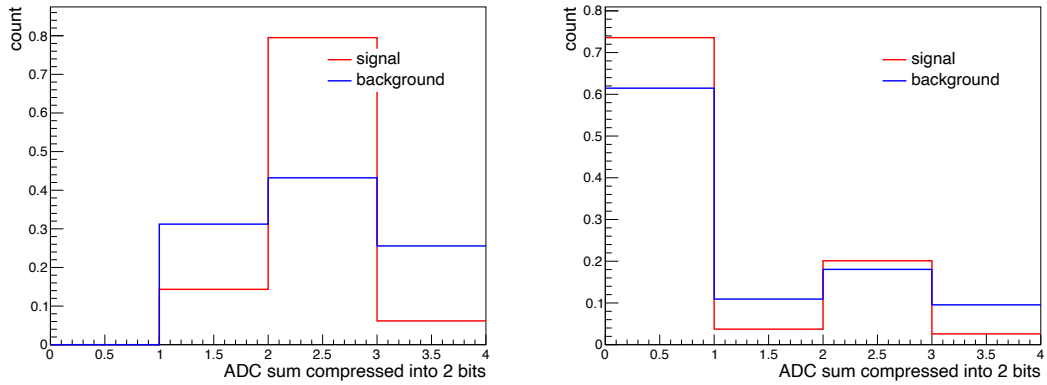

(a) (b)

Figure 8.6: Distribution of the 2-bit ADC-sum after the compression of the ADC sum on the local (a) and neighbouring (b) wires. q_{th} for the ADC cut is set to 900 ADC counts. To compress the ADC-sum, $(q^0_{div}, q^1_{div}, q^2_{div})$ is set (6, 100, 500).

the 2-bit ADC-sum for each wire within the integration time of t_I.

Second, on the COTTRI FEs, multi-hit samples are filtered to mainly reduce background hits by low-energy electrons, as discussed in Section 3.3. Because of those electrons, the number of background his in the integration time is larger than the one of the signal hits, as shown in Figure 8.7. Although a conversion electron typically makes a hit in the cell in the integration time, multi-turn tracks of the conversion electron and accidental coincidence hits can help in making multiple hits. By filtering multi-hit samples, 37% of the background hits are rejected, while 86% of the signal hits are accepted. The distribution of the 2-bit ADC-sum after this filter is shown in Figure 8.8. In comparison with Figure 8.6, this filter makes the ratio of 0 ADC-sum on the neighbouring wires large. As intended, the distribution of the backgrounds is changed more than the one of the conversion electron. The multi-hit filter works for making a larger difference between signal and background data. The

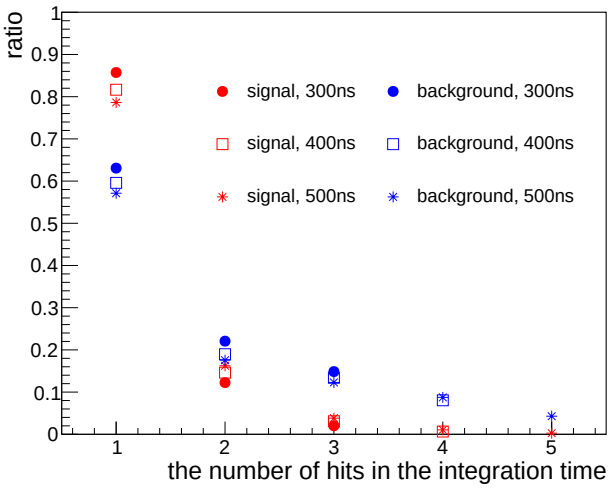

Figure 8.7: Ratio of the number of hits in the integration time. Each marker style is applied for data points of the integration time of 300 ns, 400 ns, or 500 ns.

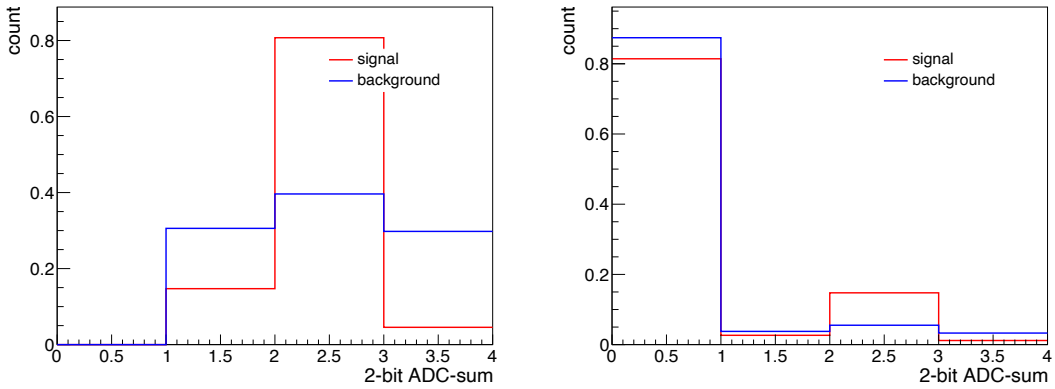

(a) (b)

Figure 8.8: Distribution of the 2-bit ADC-sum on the local (a) and neighbouring (b) wires after filtering multi-hit samples.

distribution of the 2-bit ADC-sum on the local wire is basically not changed. The hit classification is performed by using these data.

To compare the hit classification performance with the 2-bit ADC-sum, the raw and 1-bit ADC-sum are prepared by applying the above processes: the raw ADC-sum in Figure 8.9 and the 1-bit ADC-sum on the neighbouring wires in Figure 8.10.

The hit classification is applied only for hit wires, so the 1-bit ADC-sum of the classified local wire must be 1.

8.2 Hit classification

The GBDT-based hit classification was performed by using the Toolkit for Multivariate Data Analysis with ROOT (TMVA), which provides not only classical but also machine learning techniques for classification and regression [63]. Half of the total simulated events, corresponding to 4608 bunches, were used to evaluate the

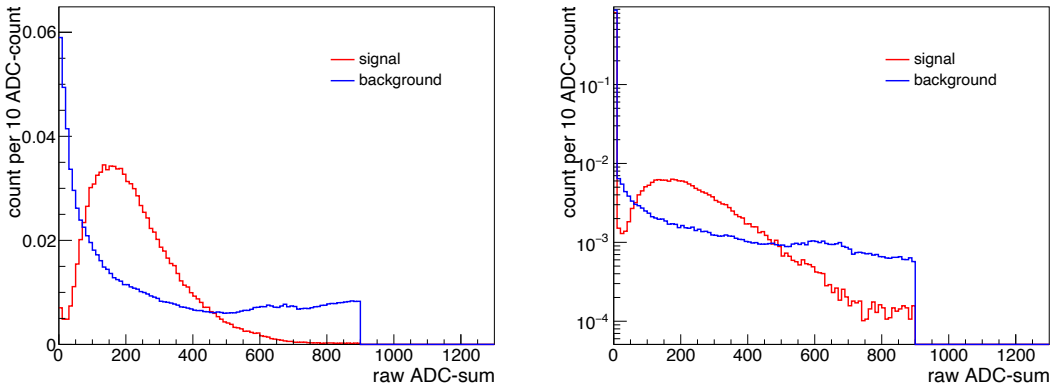

Figure 8.9: Distribution of the raw ADC-sum on the local (a) and neighbouring (b) wires after filtering multi-hit samples.

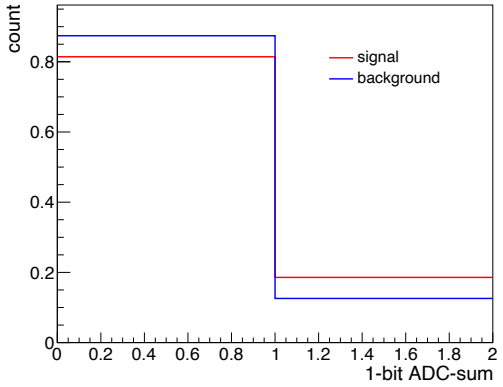

Figure 8.10: Distribution of the 1-bit ADC-sum on the neighbouring wires after filtering multi-hit samples. q_{th} for the ADC cut is set 900 ADC counts, the TDC threshold is 6 ADC counts.

hit classification.

8.2.1 Gradient boosted decision tree

A decision tree consists of nodes, which in turn are split into the next nodes, as drawn in Figure 8.11. Each node classifies input datum using a true or false question. So, the larger the number of nodes, the finer the data is classified, but the more calculation steps are needed. This disadvantage is solved by applying the gradient boosted technique, which calculates many small trees in parallel and combines their weak predictions $f_i(\mathbf{x})$ with weighting factors α_i. The predictive power of the tree combination $F(\mathbf{x})$ is given by:

$$F(\mathbf{x}) = \sum_{i=1}^{M} \alpha_i f_i(\mathbf{x}) . \tag{8.1}$$

The weighting factors are determined by the classification error rate of the small trees. Figure 8.12 shows the schematic view of a boosted decision tree. This decision

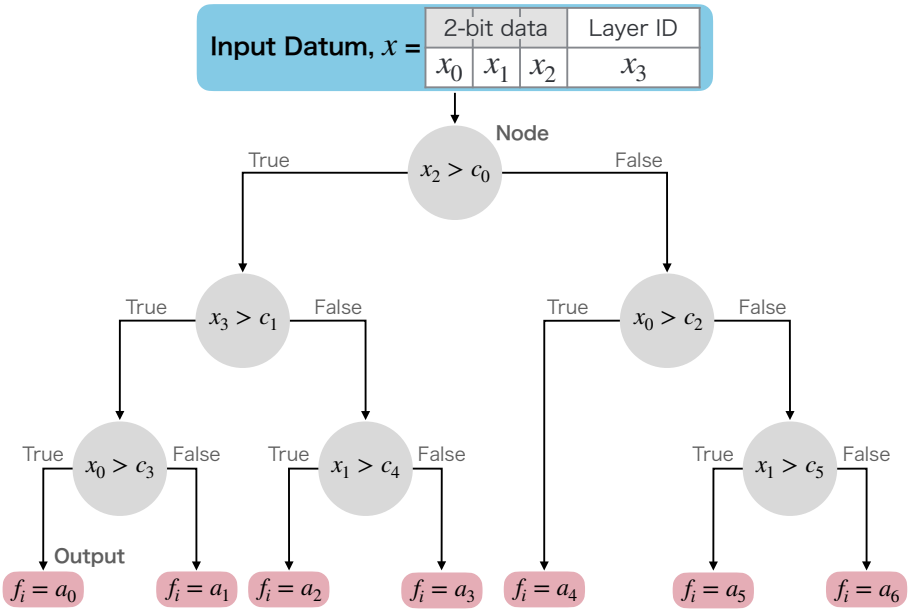

Figure 8.11: Schematic view of a decision tree. The input datum, $\mathbf{x}$ is represented as a blue block, and the output is drawn in red. Gray circles show the splitting nodes. x_i is the split data, c_i is a threshold value in each node, and $y = a_i$ is an output value of the tree. The maximum depth of this tree is three. If the split data size is too small or the signal-background separation is good enough, no more splitting node is added.

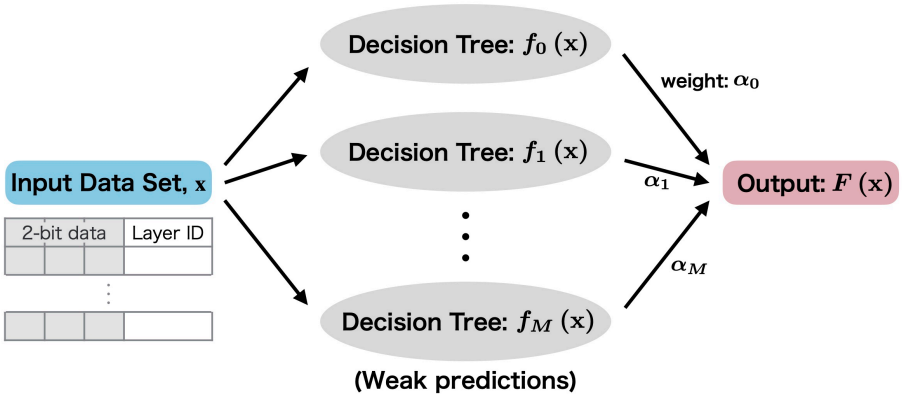

Figure 8.12: Schematic view of a boosted decision tree. The input datum $\mathbf{x}$ is represented as a blue block, and gray circles show the decision trees $f_i(\mathbf{x})$ weighted by a parameter α_i. The output $F(\mathbf{x})$ given by Equation 8.1 is drawn in red.

tree collaborating with the gradient boosted technique is called GBDT.

Here, training and testing parameters were set as the follows:

- training and testing data
  - Half of the total hits in the 4608 simulated bunches were for training, and the other half was for testing. In the case of the parameter set introduced in the previous section, 152167 signal hits and 1110280 background hits were applied for each training or testing.

- tree structure
  - 1000 trees were created for one training. In a node, 5% of the total training hits were required to continue the calculation. To find optimal cut in each node, the grid number of the discriminating variables was 20. The depth of each tree was allowed to be five at most.
- tree update
  - 50% of the training samples were randomly picked up for a new tree. At the end of a training step, an error was calculated to be true signal-hit ratio minus predicted signal-hit ratio in outputs of each tree. To suppress over-training, the errors were multiplied by a learning rate of 0.1 and used to update weight parameters α_i for the next step.
- GBDT output
  - Each GBDT provided a score from 0 to 1 for input datum. This score is large for a signal-like hit and small for a background-like hit.

These parameters were not optimised while the timing parameters and thresholds are optimised as discussed in Section 8.1.1. After training, the performance of the GBDT classification was evaluated using the testing data set.

8.2.2 Classification performance

The distributions of the input features for GBDTs are Figure 8.5 and Figure 8.8. The GBDT score distributions for the testing data are shown in Figure 8.13. No CDC hit whose GBDT score is 1 means that there is no unique pattern of the input features for the signal hits against the background-hit features. In the case of 2-bit ADC-sum, the number of possible patterns of the input features is $2^6 \times 16 = 1024$ where 2-bit ADC-sums for the local and neighbouring wires make $2^{2\cdot3}$ patterns, and the number of the CDC layers related with the classification is 16. So, the GBDT can work, but the score distribution is jaggy rather than smooth. From these results, receiver operating characteristic (ROC) curves are drawn in Figure 8.14. As expected from the distributions of the GBDT scores, the raw ADC-sum shows the best performance of the three ADC-sum types. The difference of classification performance between the 2-bit and 1-bit ADC-sum indicates that not only applying the ADC cut but using the compressed ADC-sum improves the quality of the hit classification.

The linear correlation coefficient is useful to evaluate the relationship of the input-feature combination because it gives the strength of the linear relationship between two variables. The correlation matrices whose elements are the coefficients are drawn in Figure 8.15. The layer ID makes more differences in the correlation coefficient between the signal and background features than other input features. For the signal hits, the correlation coefficient between the layer ID and the local feature is smaller than the one between the layer ID and the neighbouring features. Since the background hits are distributed almost flat on all the layers, the layer ID has less correlation with the ADC sum of the backgrounds. In all the cases, it was found that the neighbouring features provide the largest correlation coefficients with other features. According to these correlation matrices, the layer ID contributes the most to the classification quality.

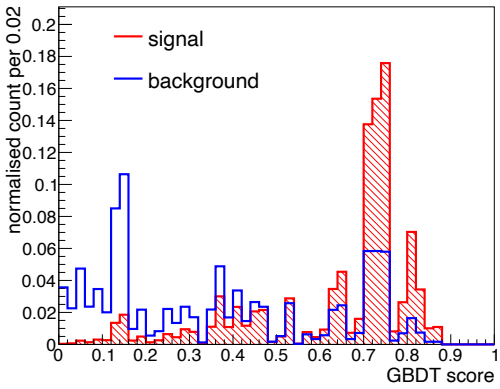

(a) 2-bit ADC-sum

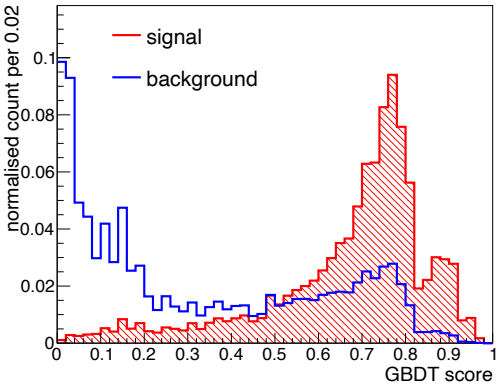

(b) raw ADC-sum

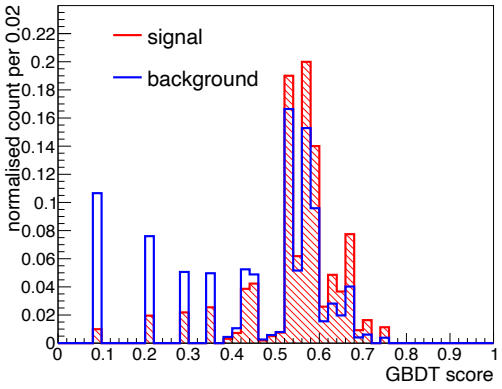

(c) 1-bit ADC-sum

Figure 8.13: Distribution of the GBDT outputs for 2-bit, raw, and 1-bit ADC-sums. The parameters are set as the follows: $t_{min} = 500$, $t_{max} = 1400$, $q_{th} = 900$, $(q^0_{div},\ q^1_{div},\ q^2_{div}) = (6,\ 100,\ 500)$, and $t_I = 400$.

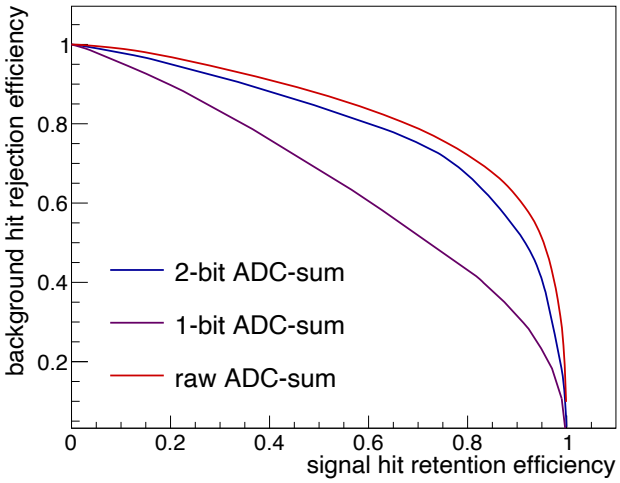

Figure 8.14: Receiver operating characteristic curves of the hit classification.

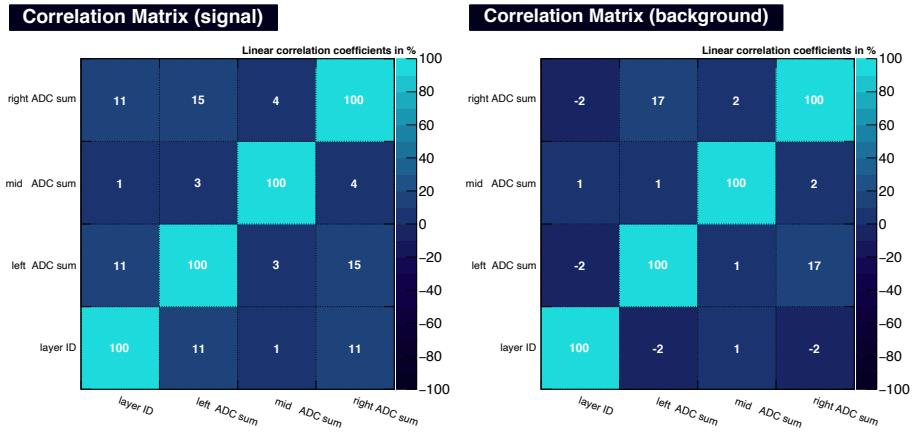

(a) 2-bit ADC-sum

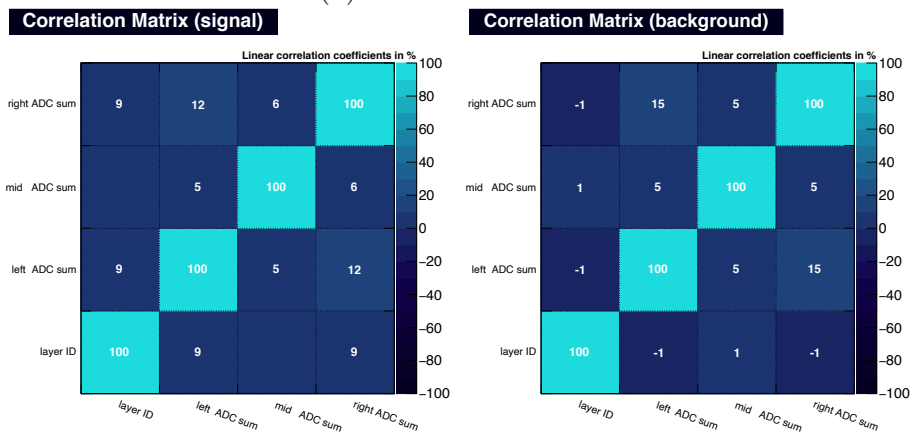

(b) raw ADC-sum

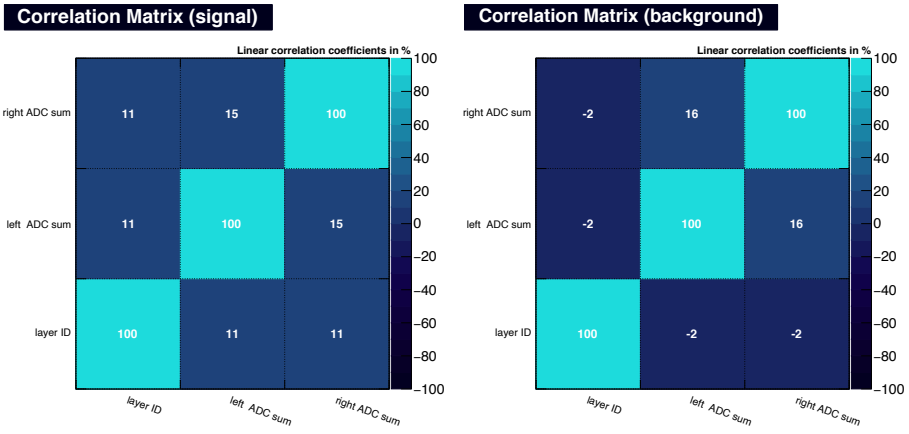

(c) 1-bit ADC-sum

Figure 8.15: Correlation matrix of the GBDT input features. In these plots, "mid ADC sum" represents the ADC sum on the local wire; "right ADC sum" and "left ADC sum" represent the ADC sums on the neighbouring wires. For the 1-bit ADC-sum, since the value of the local feature does not vary, it is not considered. The parameters are set as follows: $t_{min} = 500$, $t_{max} = 1400$, $q_{th} = 900$, $(q^0_{div},\ q^1_{div},\ q^2_{div}) = (6,\ 100,\ 500)$, and $t_I = 400$.

8.3 Event classification

The event classification is performed by counting the number of CDC hits whose GBDT score exceeds the threshold. The COTTRI FEs apply that threshold on

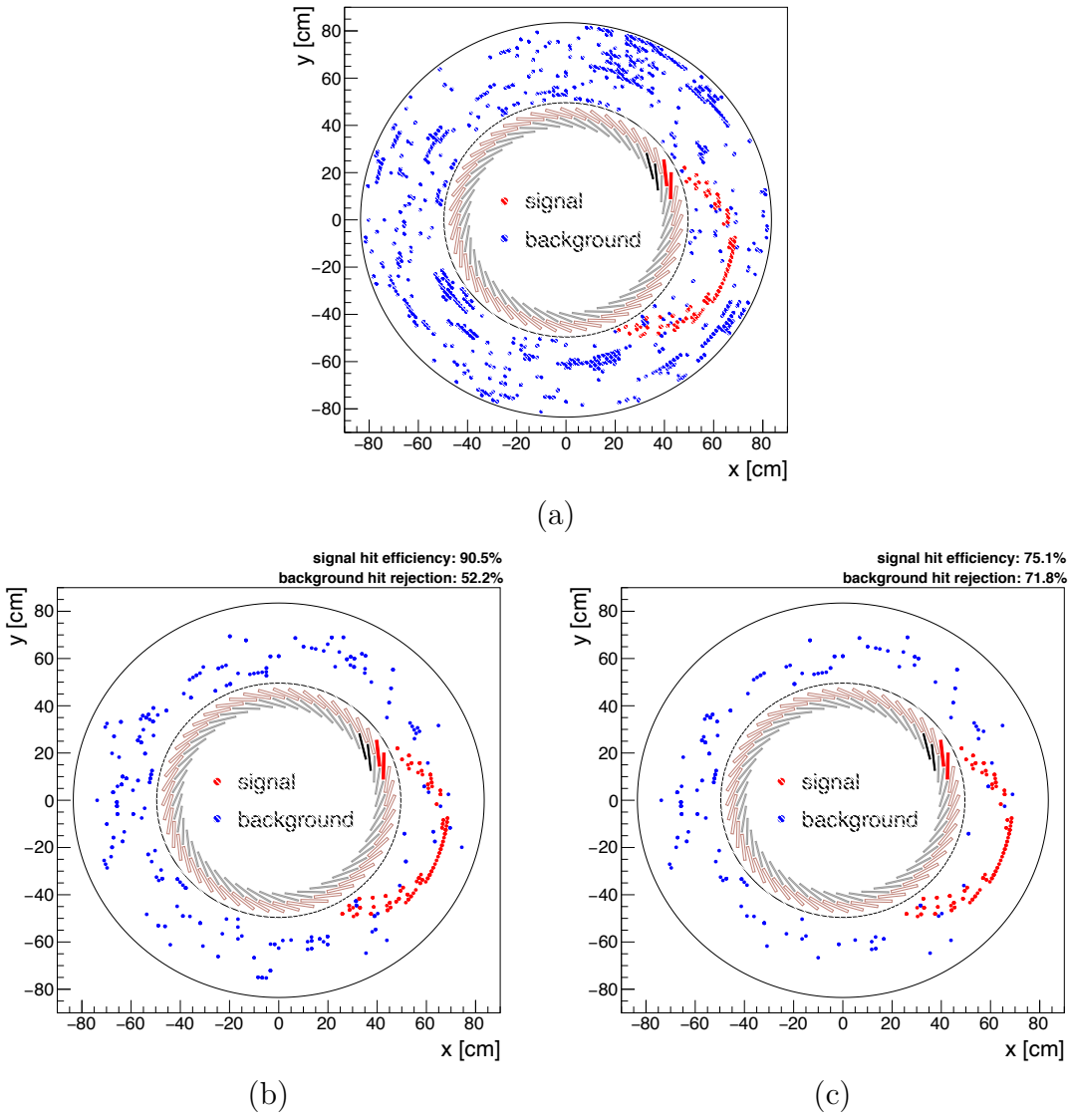

Figure 8.16: CDC event display in the integration time of 400 ns.

each hit score and counts the number of remaining hits in each RECBE. The COTTRI MB collects them and makes a CDC-trigger decision in the CDC active section for each CTH module. So, this threshold is one of the key parameters to optimise COTTRI performance. From the GBDT-score distribution, the threshold is uniquely determined for a signal-hit acceptance. Here, varying the signal-hit acceptance from 25% to 95% at a 5% interval, the classification quality was scanned on this parameter space. As shown in Figure 8.13, since the GBDT scores distribute discretely in the case of a 2-bit or 1-bit ADC-sum, that interval is not necessarily 5%. Figure 8.17 shows the relationship between signal-hit acceptance and the GBDT-score thresholds.

8.3.1 COTTRI-FE boundary

Each COTTRI FE performs the hit classification by handling the data from eight or nine RECBEs, then some of the neighbouring features are missed due to a boundary

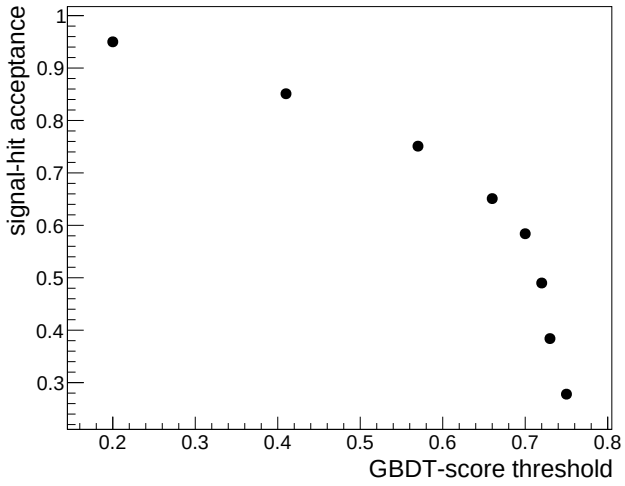

Figure 8.17: Relationship between the signal-hit acceptance and the GBDT-score thresholds.

of the readout area on each COTTRI FE. Those neighbouring features were assumed to be a signal-like number here. In the case of the parameter set in Section 8.1.2, the assumed numbers were 2 for the 2-bit ADC-sum, 1 for the 1-bit ADC-sum, and 150 for the raw ADC-sum. Although the numbers for the first two cases were clearly decided, the number for the last case was not because of the continuous distribution at the resolution of a single-precision floating-point number. That number was determined without optimization.

8.3.2 CDC geometrical cut

A conversion electron does not leave hits in the entire readout area but in a part of the readout area. Furthermore, in a 1-T magnetic field, the helical trajectories of the conversion electrons must be in the same direction on the readout plane. Even though the stereo layer configuration provides distorted hit patterns on the plane perpendicular to the CDC axis, a CDC geometrical cut can be applied by using the CTH-hit position and constraining an active section of the CDC. The size of this section was decided with reference to the maximum central angle which is defined by a set of the conversion-electron hits in the CDC and CTH as illustrated in Figure 8.18. The central angle of the signal trajectories ranges from 0° to around 110°, and it can be shown in Figure 8.19. To consider the whole signal hit region in the trigger algorithm, the active section of the CDC consists of six RECBEs on two innermost layers and seven RECBEs on the other layers corresponding to the central angles of 135° and 140°, respectively. Each active section is adopted for the three CTH modules, so 16 sections are defined. Figure 8.20 explains two examples of the sections for the CDC geometrical cut.

8.3.3 CTH fake trigger

In the evaluation of the COTTRI performance, the number of applied events should be as large as possible to keep the uncertainty of the classification performance low. The signal events, where conversion-electron tracks satisfy with the CTH trigger

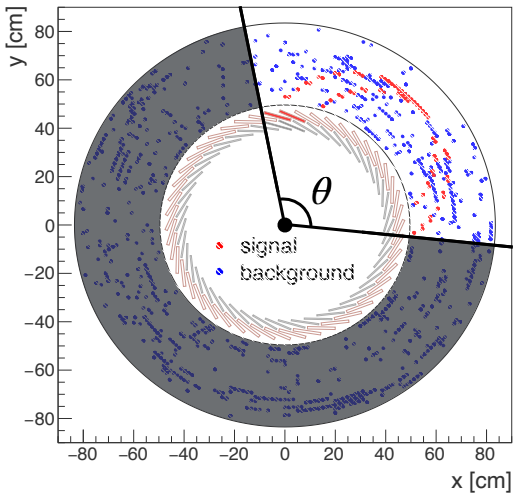

Figure 8.18: Illustration of the maximum central angle defined by a set of the conversion-electron hits in the CDC and CTH at the endplate of the readout side.

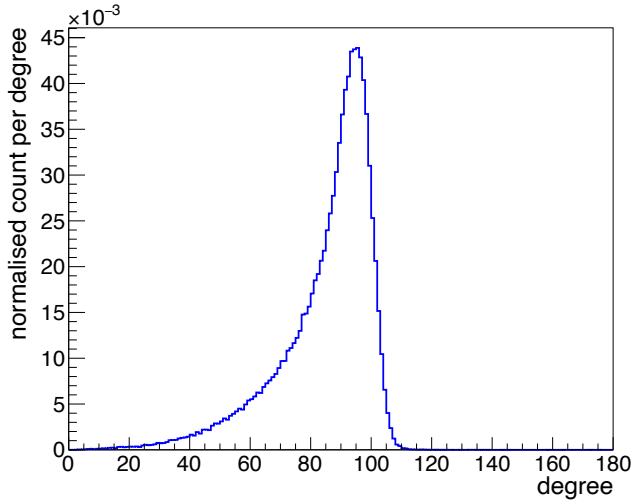

Figure 8.19: Central angle distribution of the conversion-electron trajectories.

requirements, are selected. On the other hand, the CTH fake-trigger rate is suppressed by the four-fold coincidence technique; many background events have no CTH fake trigger. Even if the measurement window is (200 ns, 1170 ns), it is less than 300 kHz according to Figure 6.14. It means that less than 35% of the MC produced background events is triggered by taking the four-fold coincidence. Thus, most of the simulated events contain a fake trigger. To use the simulated event efficiently, the modules and timing of the CTH fake trigger were randomly selected to follow the trigger timing distribution based on Figure 6.14 (b). This method would not significantly change the evaluation results because the CTH hits causing fake triggers have less correlation with the CDC hit pattern. Figure 8.21 shows an example of the distributions of the simulated trigger timing and modules.

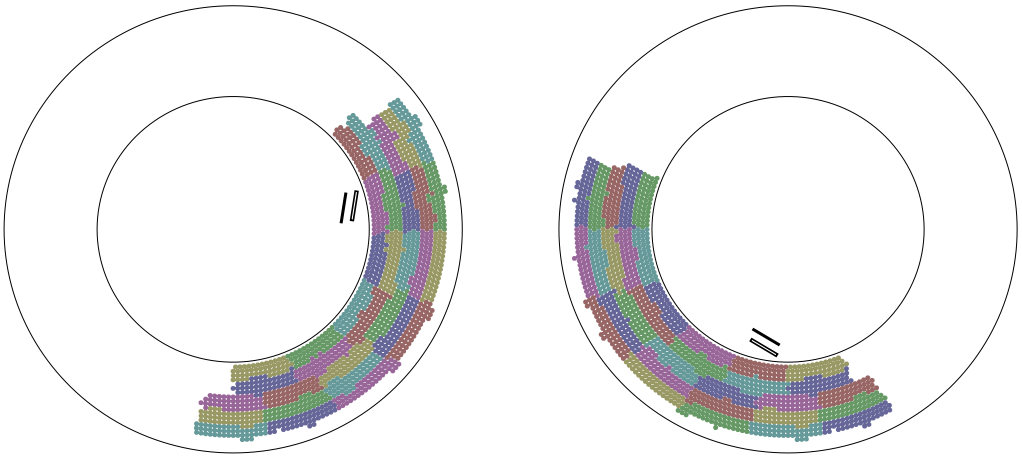

(a) (b)

Figure 8.20: Example of the CDC geometrical cut. The CTH counters in each panel are signal-hit counters.

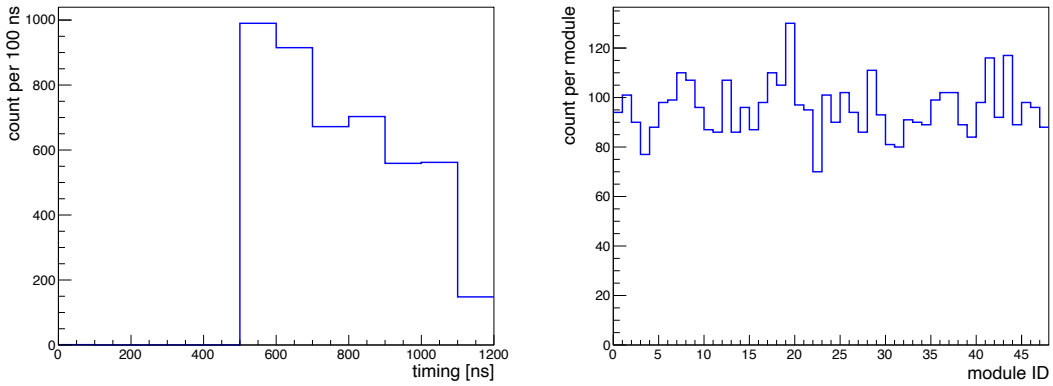

(a) Trigger timing (b) Trigger module

Figure 8.21: Distribution of the simulated fake trigger timing (a) and modules (b). 48 CTH modules are placed on each side of the upstream and downstream. However, the projection of both sides onto the CDC readout plane is only considered; module ID on the horizontal axis is 0 to 47.

8.3.4 Trigger performance

The COTTRI system has to be adjusted to optimise signal-event retention efficiency against required background-event rejection efficiency. Here, they are given by:

$$\text{Signal-event retention efficiency} = \frac{\text{N (triggered signal event)}}{\text{N (MC produced signal event)}} \tag{8.2}$$

and

$$\text{Background-event rejection efficiency} = \frac{\text{N (not-triggered background event)}}{\text{N (MC produced background event)}}. \tag{8.3}$$

The t_{min} dependence of the required background-event rejection efficiency was first seen. This was calculated from the CTH fake trigger rate in Section 6.5.3 by applying

a safety factor of two. The calculation result in Figure 8.22 indicates that the background-event rejection efficiency is required to be about 70% at least to suppress the trigger rate enough for the stable DAQ operation.

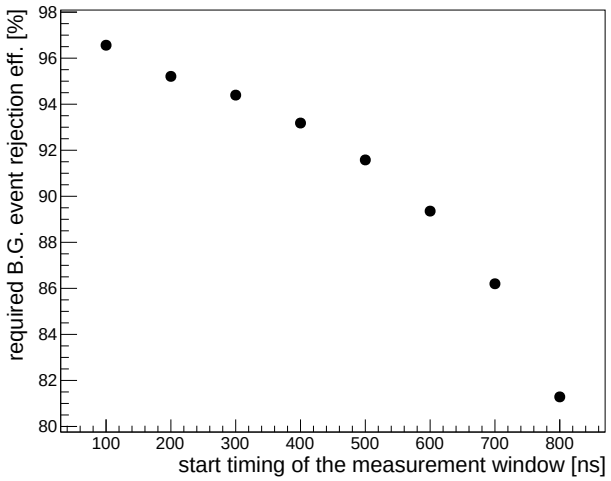

Figure 8.22: Requirement of the background-event rejection efficiency.

The number of the CDC hits whose GBDT scores exceed a threshold was counted in each event. As examples, the distributions of the total hits for the cases of 95.0% and 65.0% signal-hit efficiency are shown in Figure 8.23. The lower the signal-hit

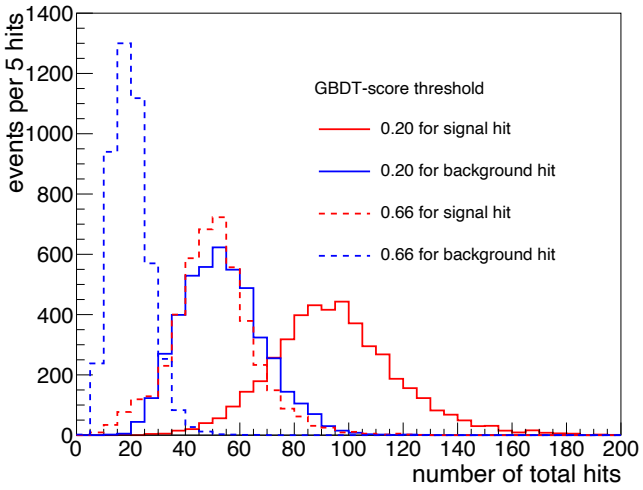

Figure 8.23: Distribution of the total number of hits in the signal and background events. Two cases are shown here: GBDT-score thresholds of 0.2 (solid line) and 0.66 (dashed line). The former corresponds to 95.0% signal-hit acceptance with 40.7% background-hit rejection efficiency. The latter corresponds to 65.0% signal-hit acceptance with 77.8% background-hit rejection efficiency.

efficiency applied, the larger the background-hit rejection efficiency becomes, and the smaller the distribution width becomes due to the tiny fluctuation of the accepted-hit numbers. The mean value of the total number of hits in signal events is larger than the one in background events because the signal events contain a baseline of

the number of background hits, too. From the number ratio between the signal and background events, the ROC curve of the event classification was calculated as represented in Figure 8.24. Even though the CDC geometrical cut is applied, the

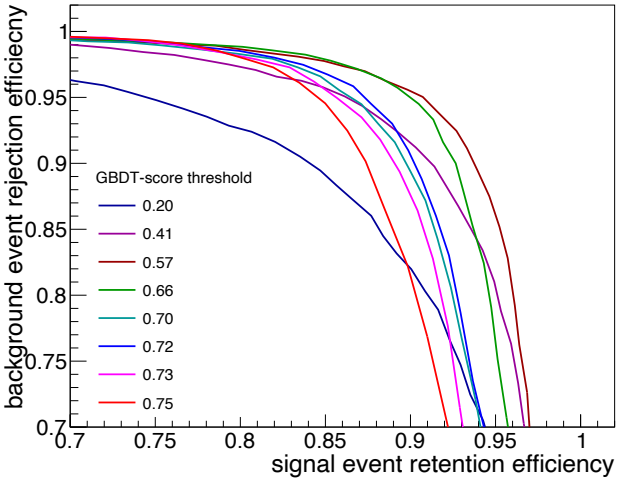

Figure 8.24: ROC curves for GBDT-score thresholds in the event classification.

number of background hits is too many against the number of signal hits. For the signal-event acceptance, when it is high, the background-event rejection efficiency becomes lower, and it is not enough to reach the best performance of the event classification. On the other hand, when the efficiency of signal hits is too small, the classification performance becomes worse. Thus, there is a trade-off between the signal-hit acceptance and the performance of the event classification. In the case of Figure 8.24, the best signal-event acceptance is given by the signal-hit acceptance of 75.1%, while the background-hit rejection efficiency is 71.8%.

Parameter scan

Based on the procedures and results discussed above, the parameter scan was performed. The target parameters are defined in Section 8.1.1. As shown in Figure 8.24, signal-hit acceptance is one of the parameters to optimise the performance of the event classification. The required signal-hit acceptance is changed from 25% to 95% at a 5% interval.

Figure 8.25 summarises the signal-event trigger efficiency, which is required to achieve the DAQ trigger rate of 13 kHz including the safety factor of two. q_{th} of 900 for 2-bit and raw ADC-sum gives better signal-event trigger efficiency than q_{th} of 600 in almost all the parameter sets. (q^1_{div}, q^2_{div}) of (100,400) or (100, 500) is the best combination.The CDC-trigger efficiency is increased by shifting the start timing later because the background level in a bunch period decays in the time direction. Required background-hit rejection efficiency decreases as well, resulting in a larger signal-background ratio at the end of a bunch period than the one at the beginning of a bunch period. In comparison between the results of 2-bit and raw ADC-sum, the signal-event trigger efficiency is similar to each other at the bunch end while the 2-bit ADC-sum provides better efficiency than the raw ADC-sum at the beginning of a proton-bunch period. In the current design of the COMET Phase-I experiment,

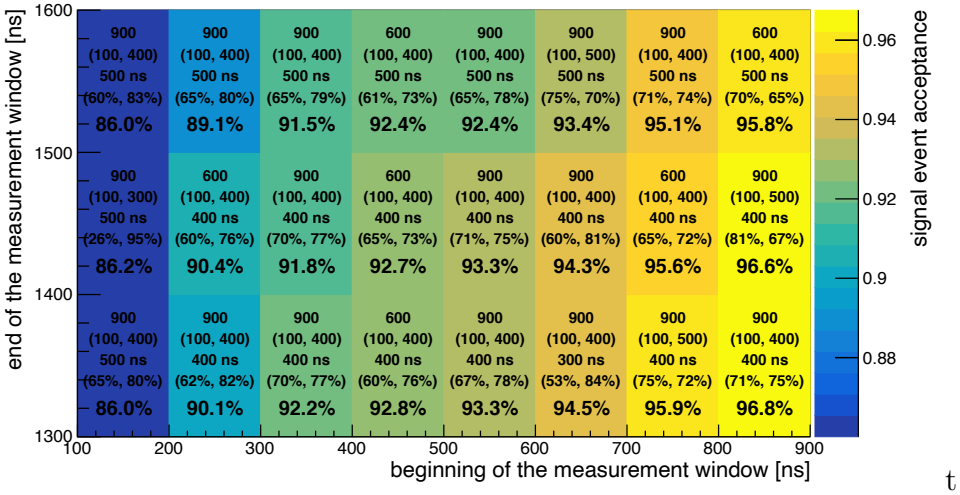

(a) 2-bit ADC-sum

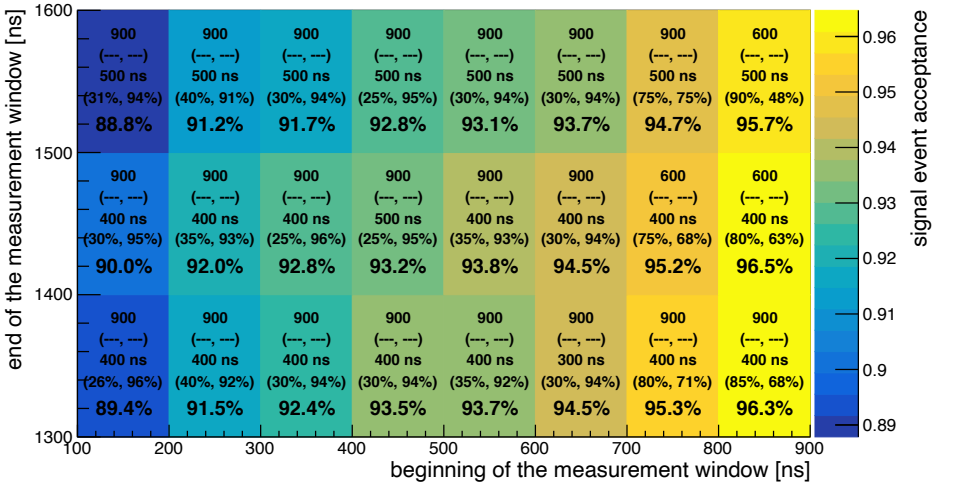

(b) raw ADC-sum

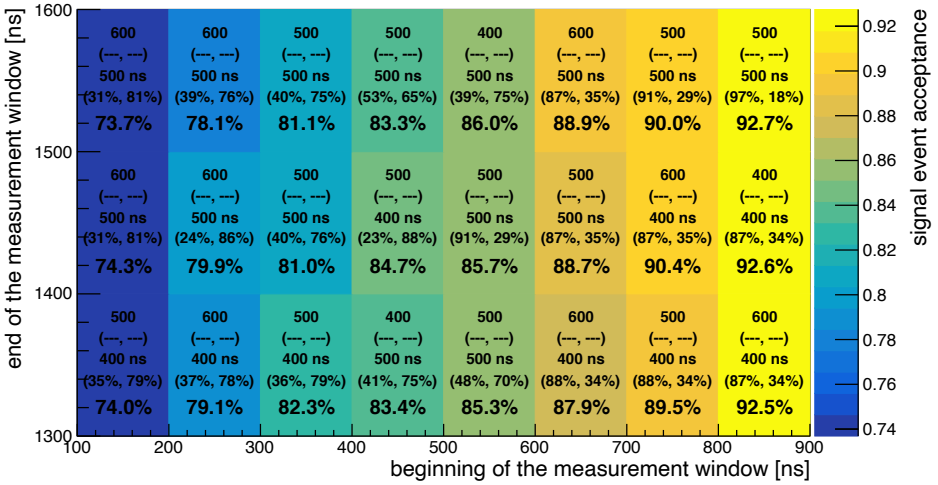

(c) 1-bit ADC-sum

Figure 8.25: Best performance of the event classification. Text in each bin represents q_{th}, (q^1_{div}, q^2_{div}), t_I, (signal-hit efficiency, background-hit rejection efficiency), and signal-event efficiency. "-" is a non-assigned parameter.

the measurement window starts from 700 ns. Then, the signal-event acceptance is expected to be 95.9% at most, while the trigger rate is kept to be 13 kHz. To obtain this performance, the parameter setup is $q_{th} = 900$, $(q^1_{div},\ q^2_{div}) = (100,\ 500)$, $t_I = 400$ ns, and signal-hit acceptance of 75%.

Uncertainty from the random trigger

As discussed in Section 8.3.3, the CTH fake trigger is randomly chosen here. Uncertainty from this random trigger has to be evaluated. The number of possible timing-module sets depends on the length of the measurement window. The longer the measurement window is, the larger the uncertainty is expected to be. Then, the measurement window from 100 ns to 1400 ns is suitable to evaluate the uncertainty conservatively. For the parameter set of $(q^1_{div},\ q^2_{div}) = (100,\ 500)$ and $t_I = 400$, the event classification was carried out 1000 times with a different random seed for each. The result values of the signal-event acceptance fluctuate, as shown in Figure 8.26. In this study, it was decided to consider values of mean and root mean square of

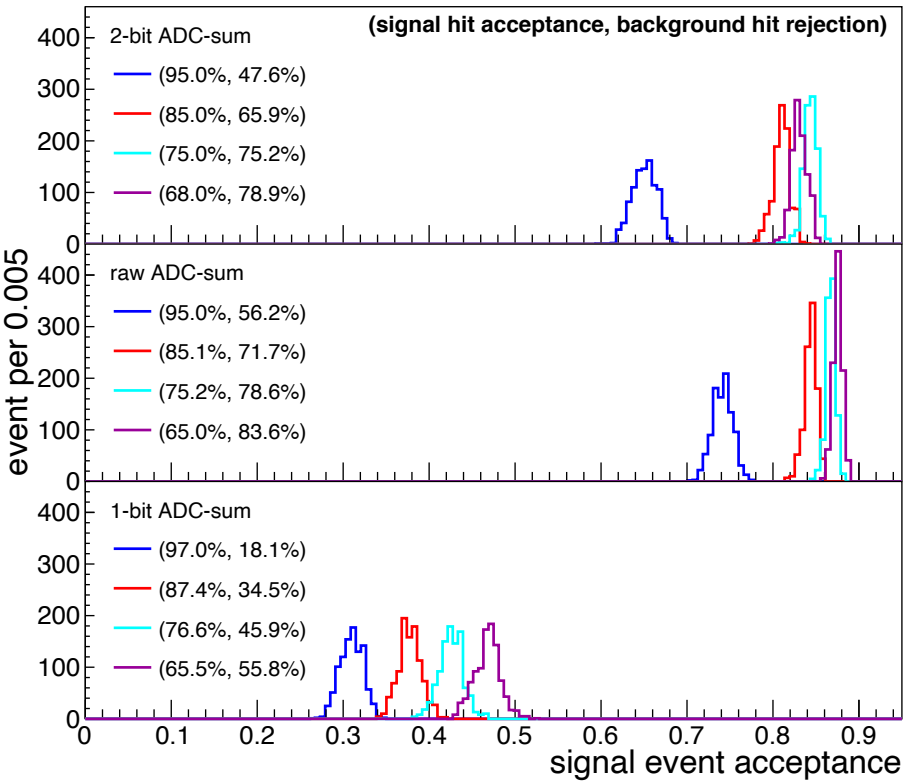

Figure 8.26: Distribution of the signal-event acceptance. Signal-event acceptance depends on signal-hit acceptance. For each ADC-sum type, four cases of the hit classification grades are selected as examples.

each distribution as the signal-event acceptance and that uncertainty, respectively. Figure 8.27 shows the relation between the uncertainty and the signal-event acceptance. From the figure, a negative correlation is observed. Near the maximum value of the signal-event acceptance, its uncertainty is less than around 0.6%.

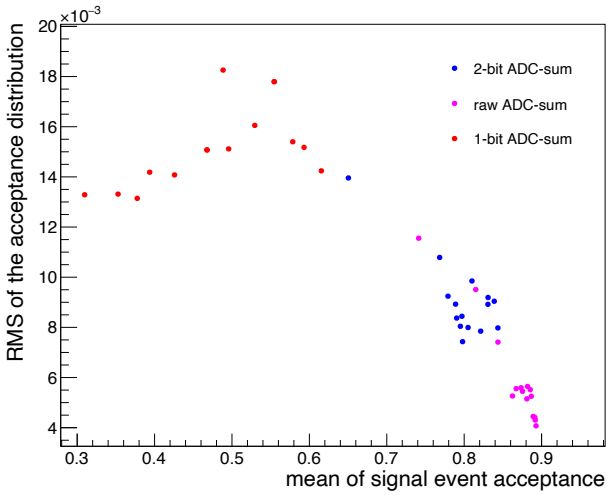

Figure 8.27: Relationship between the signal-event acceptance and its uncertainty.

8.4 Summary

In this chapter, the performance of the COTTRI system is discussed. The COTTRI system consists of a GBDT-based hit classification and an event classification. The classification starts from two input features of CDC hits: the radial position of each CDC wire and the ADC-sum corresponding to the deposited energy on each cell. First, to handle these features in the online trigger system, they were customised by applying the following parameters: the measurement window in a bunch period, the integration time for considering the drift time, the threshold for the ADC cut, two sets of the thresholds for data compression, and filtering multi-hit samples. The GBDTs whose inputs are those customised features showed two things. One is that the use of a 2-bit ADC-sum gives a much better quality hit classification than the use of a 1-bit ADC-sum. The other one is that the radial wire position is the parameter that most affects the hit-classification performance. Before the event classification, the CDC geometrical cut is dedicated to reducing the background hits. The required trigger rate for the COMET DAQ system is 13 kHz including a safety factor of two. The event classification was evaluated in terms of the signal-event acceptance against this requirement. As a result of the event classification, the COTTRI system provides a signal-event acceptance of 86.0% to 96.8% for any measurement window while satisfying the trigger requirement.

Chapter 9

Discussion

This chapter describes the impact of this study on the COMET Phase-I experiment and what has to be done before the physics measurement.

9.1 Impact on the COMET Phase-I experiment

It has been shown that the simulated performance of the COTTRI system meets the required trigger rate of 13 kHz with a safety factor of two. From this result, the total signal acceptance and the single event sensitivity in the physics measurement are estimated.

9.1.1 Signal acceptance

The online trigger acceptance is discussed, so far. The signal acceptance is determined by both the online trigger acceptance and offline analysis efficiency. The offline analysis stage consists of the track quality cuts, track finding, and applying the momentum window. Here, high-quality tracks are selected by applying the following:

- the track must reach the 5-th sense layer. This requirement is to set the minimum transverse momentum in order to get good tracks.
- number of hits must be larger than 30 hits for fitting.

The efficiency of the track quality cuts is calculated by using triggered events in Section 8.4. For example, it is 94.6% for the measurement window of 700 ns to 1170 ns. To estimate the total signal acceptance, the acceptance of the track finding and the momentum window are set to the target design values of 99% and 93%, respectively. The total signal acceptance is a product of these components and is 4.2%. They are summarised in Table 9.1.

According to the online trigger performance, the measurement window of the online trigger can be larger enough so as to make room to improve the total acceptance by altering the measurement window in the offline analysis. If the measurement window of 500 ns to 1170 ns is adopted, the total signal acceptance increases to 6.7% from 4.2% with the following breakdown of contribution changes:

- Measurement window: from 30.6% to 49.8%,

Table 9.1: Factors contributing to the signal event sensitivity.

Event selection	Value	Comment
Geometry	18.3%	Discussed in Section 6.5.3
Measurement window	30.6%	700 ns $< t <$ 1170 ns, Discussed in Section 6.5.3
Online event selection	95.9%	Discussed in Section 8.4
DAQ efficiency	90%	Target design value [27]
Track finding	99%	Target design value [27]
Track-quality cut	94.6%	
Momentum window	93%	103.6 MeV/c $< P_e <$ 106.0 MeV/c, Target design value [27]
Total	4.2%	

- Online event selection: from 95.9% to 93.3%, and
- Track-quality cut: from 94.6% to 95.7%.

This improvement to the acceptance is brought about by a large increase in the measurement-window acceptance and less deterioration of the online event selection efficiency.

9.1.2 Single event sensitivity

The single event sensitivity is calculated by:

$$B\left(\mu^- + \mathrm{Al} \to \mathrm{e}^- + \mathrm{Al}\right) = \frac{1}{t_{run} \cdot R_\mu \cdot f_{cap} \cdot f_{gnd} \cdot A_{\mu-e}}, \tag{9.1}$$

where t_{run} is the total running time of the measurement, R_μ is the muon stopping rate at the aluminium target disks, f_{cap} is the muon capture rate by aluminium nuclei, f_{gnd} is the ratio of the final state being the ground state of an aluminium nucleus, and $A_{\mu-e}$ is the signal acceptance. The muon stopping rate is given by the proton beam intensity and the number of stopping muons per proton on the target. For the 8 GeV, 3.2 kW proton beam, 2.5×10^{12} protons per second impinge on the graphite target. 4.7×10^{-4} muons per POT stop on the aluminium target disks [27]. The experiment focuses on muons captured by nuclei because the $\mu \to e$ conversion process by interaction with an atomic nucleus is considered. The final state of the $\mu \to e$ conversion has to be the ground state of an aluminium nucleus because the momentum window of signal detection is set for the conversion electron that does not lose additional energy except for the nuclear recoil energy and the nuclear binding energy. Table 9.2 is the list of factors contributing to the signal event sensitivity for the target design values. Then, the single event sensitivity is 2.8×10^{-15}. The background level for a single-event-sensitivity of 3×10^{-15} was estimated to be 0.032 events by other studies in the COMET collaboration [27]. In this estimation, the background induced by cosmic rays is the main background and estimated to be < 0.01. Since the COTTRI system gives a chance to expand the measurement window, the signal event sensitivity in a longer measurement window was also estimated. If the beginning of the measurement window is 500 ns, the single

Table 9.2: Factors contributing to the signal event sensitivity for the target design values.

Factor	Value	Comment
t_{run}	150 days	Design value
R_μ	$1.2 \times 10^9\ \mu$/s	Design value
f_{cap}	0.61	Reference [27]
f_{gnd}	0.9	Reference [64]
$A_{\mu-e}$	0.042	Discussed in Section 9.1.1

event sensitivity becomes 1.7×10^{-15}. Then, the cosmic-ray background is < 0.014 because it is just proportional to the detection live time. It is still small enough for one-event detection. However, the increase in beam-related backgrounds has to be checked carefully.

9.2 Future work

The basic hardware logic of the COTTRI system has been constructed. Its performance has been also estimated by using the simulation data. Before the physics measurement, three significant tasks have to be completed: producing and updating the trigger system, calibration of the GBDTs, and the background measurement.

9.2.1 Updating the trigger system

First, eight more COTTRI FE boards must be produced for the operation of the full trigger system because only two COTTRI FE boards were produced and tested. As described in Chapter 3, the electronics related to the COTTRI system and the basic parts of its firmware have been developed and tested. However, the current firmware of the COTTRI MB does not include the function of the CDC geometrical cut. The current implemented function counts the number of CDC hits whose GBDT scores exceed a threshold, makes the trigger decision, and sends the CDC trigger signal to the FC7, so far. This part has to be modified to sum the CDC hits up in each sector of the CDC geometrical cuts and send its summation. The COTTRI MB can send 96-bit data to the FC7 at 40 MHz, and therefore, 384-bit data can be transmitted within 100 ns. If the data size for each sector is decided to be 16 bits, the data for all 16 sectors can be sent every 100 ns. This data format allows the COTTRI system to use not only the number of CDC hits but the summation of 6-bit GBDT scores for the trigger decision. In each sector of the geometrical cut, there are 33 RECBEs $\times$ 48 wires/RECBE = 1584 wires. According to Figure 8.3, it can be assumed that the maximum number of CDC hits every 100 ns in a sector of the geometrical cut is less than 1000. Then, the 16-bit data size is large enough for the summation of GBDT scores.

The COTTRI system for the CTH is being designed and developed. The FC7 firmware also has to be modified to make the trigger signal with a coincidence between the CTH and CDC trigger. It will be updated as soon as the CTH electronics are fixed.

9.2.2 Calibration

The GBDTs must be calibrated by the real data measured in the calibration run, where the background level is also measured. The raw mode of the RECBE will be applied to take the full-channel data including information of both waveform and timing. As mentioned in Chapter 5, the data handled in the COTTRI system is reproducible in an offline analysis using that data. In the calibration run, the reproduced data can be used to simulate realistic data processing in the COTTRI system. The simulated data from this processing is merged with the $\mu \to e$ conversion event from the Monte Carlo simulation to optimise the GBDTs. These optimization processes will be applied before and during the physics measurement, and the classification performance should be gradually improved.

9.2.3 Background measurement

A combination between the fake trigger and the beam-related backgrounds, such as pion and muon decays, could result in misidentification of a background track as an electron track from the $\mu \to e$ conversion. It is serious because those backgrounds can produce signal-like electrons, as mentioned in Section 2.1.1. Therefore, the long measurement window is not necessarily desirable in the physics measurement, and it must be optimised. To this end, the beam measurement is planned to evaluate the beam-related backgrounds using a detector system, which consists of straw tube trackers and calorimeters [27]. This measurement will be performed with a suppressed proton-beam power because that detector system is located on the muon beam axis in the detector solenoid, and an unacceptable hit rate is expected with the design beam power of 8 GeV, 3.2 kW. Since background estimation in a rare-decay search has to be checked carefully, to this end, the background measurement with the design power is essential. The COTTRI system allows the CyDet to take the event data with this beam power without setting the measurement window while controlling the signal-event acceptance with some GBDT optimization. By combining the CyDet background measurement with the beam measurement, the beam-related background level in any timing can be evaluated. Especially, estimation of the pion contamination in the beam and muon in-flight-decay rate is useful to calibrate the timing and length of the measurement window. Change of the measurement window has a large impact on signal acceptance, as explained in Section 9.1.1. So, this gives a chance to get a better single-event sensitivity than the current estimation.

Chapter 10

Conclusion

The trigger system with online track recognition has been developed for $\mu \to e$ conversion search in the COMET Phase-I experiment. $\mu \to e$ conversion is one of the muon rare-decay processes, which violate lepton flavour for each generation, and has never been observed yet. To reach the greatest sensitivity, a highly intense muon beam is employed at the J-PARC. Initially, it resulted in an unacceptably high trigger rate, even though a four-fold coincidence is required for the CTH trigger. For stable DAQ operation, it must be suppressed less than 26 kHz. The COTTRI system solves this issue using both the CTH and CDC hit information. In this system, the CDC self-trigger is individually constructed, and a coincidence between the CTH and CDC trigger reduces the trigger rate further. Since the source of the fake trigger in the CTH is not the same as the background source in the CDC, it should powerfully improve the situation. In addition to the trigger-rate issue, the total processing time of the trigger system is required to be less than 7 μs because the buffering time on the RECBE is 8 μs, and the event window is 1 μs. The COTTRI system needs to satisfy this requirement, too.

The COTTRI system provides a distributed trigger architecture and consists of the hit classification together with the event classification stages. This system makes the trigger decision every 100 ns in the pipeline. The hit classification is carried out by applying GBDT-optimised LUTs with two types of input features, a radial position of the hit wire and deposited energy on the hit cell. The deposited-energy data not only on a local cell but also on neighbouring cells is used. The size of the input features is limited to be 6 bits due to the hardware size; local and neighbouring features are compressed into 2 bits for each. Each CDC hit is categorised as a signal-like hit or a background-like hit by applying a threshold for LUT outputs. LUTs convert from the input features to the outputs within a clock cycle, and therefore, the time to GBDT-based calculation can be skipped. On the event classification stage, the number of signal-like hits is counted in a sector of the CDC. The CDC trigger is generated by applying another threshold for this number.

Two electronics related to the COTTRI system, COTTRI FE and COTTRI MB, have been newly developed. The total processing time has been measured by setting up a trigger system with a function generator. The measured time is 3.24 μs, which met the requirement. In the CDC cosmic-ray test, the basic performance was also confirmed by using a part of the entire readout region. This was the first trial to test all the layers of the trigger system. The soundness of the COTTRI system was confirmed by reproducing recorded data from data on the previous stage in the

trigger system. As a result, data processing among the RECBEs, COTTRI FEs, and COTTRI MB was successfully done. Each communication was monitored to check communication errors, and all the communication lines had no error related to the connections during the 739-min run.

In the Monte Carlo study using ICEDUST, over 9000-bunch data in the COMET Phase-I experiment was simulated to estimate the performance of the COTTRI system. Half of the simulated data was used to optimise GBDTs, and the other half was used to estimate the quality of the event classification. For the required trigger rate of 13 kHz including a safety factor of two, the signal-event acceptance is expected to be 96% in the measurement window from 700 ns to 1170 ns. This means that the COTTRI system is used to suppress the trigger rate enough for the physics measurement. Then, it is concluded that the single event sensitivity of 2.8×10^{-15} is achievable with the design values in a 150 day-long physics measurement. If the beginning of the measurement window can be moved from 700 ns to 500 ns while keeping the performance of the offline analysis, the single event sensitivity is expected to be 1.7×10^{-15}. It can be concluded that the COTTRI system could solve the issue of the trigger rate in the COMET Phase-I experiment.

Appendix A

Hardware

A.1 RECBE

A.1.1 ASD

The ASD chip on the RECBE board consists of preamplifier, waveform shaping, an pulse height discrimination circuits as drawn in Figure A.1. An input signal

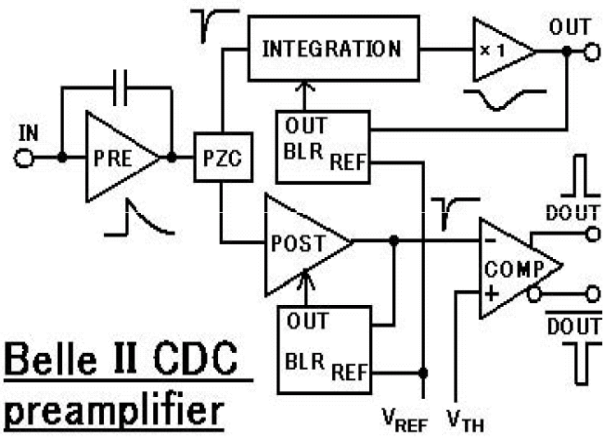

Figure A.1: Circuit diagram of the ASD chip [65].

is amplified with a gain of 1.1 mV/fC by the preamplifier. The amplified signal is converted to two output signals: an analogue signal through a waveform shaping circuit and a digital signal through a pulse height discrimination circuit. To get a high time resolution for the digital signal, the signal from the preamplifier is further amplified with a gain of approximately 7 mV/fC. A comparator receives a threshold from the DAC on the RECBE, discriminates whether the signal level is over a threshold value, and outputs the digital signal if it is higher.

A.1.2 Adapter

The RECBE has a connector to attach an optical module, HFBR-7934 from Avago[66], but this module has been discontinued. Due to the radiation issue, the use of an

optical module is avoided as much as possible. Therefore, we decided to use the DP cables and developed an adapter board to attach the DP with the onboard connector. The photograph of the adapter is shown in Figure A.2. Through this adapter,

(a) (b)

Figure A.2: Adapter attached the RECBE board for the trigger system. On the front side, (a), a DP is mounted. On the back side, (b), an HFBR-7934 is mounted to be attached to the RECBE.

the RECBE communicates with the COTTRI FE. Figure A.3 describes the pin assignments of DP on both the RECBE and COTTRI FE. In the trigger system, 2

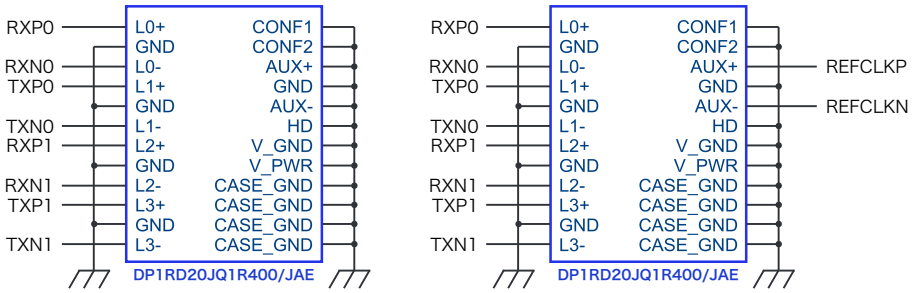

(a) (b)

Figure A.3: Pin assignments of DPs on the COTTRI FE. These DPs works for the communication with (a) the RECBEs and (b) the COTTRI MB.

TX lanes on the RECBE and 2 RX lanes on the COTTRI FE are used to transfer the trigger-related data.

A.1.3 Data format

The RECBE firmware has two data transfer modes for DAQ; raw and suppress modes. Table A.1 shows the data format for each DAQ mode. Header data is the same in both raw and suppress mode and is shown below:

- packet type (1 Byte) : data transfer mode
- board ID (1 Byte) : identification number of the RECBE
- sent number (2 Byte) : number of data transfers to a DAQ PC
- trigger time (2 Byte) : timing of a trigger signal

Table A.1: RECBE data format transferred to a DAQ PC.

(a) Raw mode

			15	14	13	12	11	10	9	8	7	6	5	4	3	2	1	0
Header			Packet Type								Board ID							
			Sent Number															
			0	Trigger Time														
			Data Length															
			Trigger Count Upper Bits															
			Trigger Count Lower Bits															
Event Data	Sample clock 0	ADC	ADC CH0															
			ADC CH1															
			...															
			ADC CH47															
		TDC	Hit Flag	TDC CH0														
			Hit Flag	TDC CH1														
			...															
			Hit Flag	TDC CH47														
	Sample clock 1	ADC	ADC CH0															
			ADC CH1															
			...															
			ADC CH47															
		TDC	Hit Flag	TDC CH0														
			Hit Flag	TDC CH1														
			...															
			Hit Flag	TDC CH47														
	Sample clock 2	ADC	ADC CH0															
	...	...	...															
	Sample clock $N_{ADC\ samples}$	TDC	Hit Flag	TDC CH47														

(b) Suppress mode

			15	14	13	12	11	10	9	8	7	6	5	4	3	2	1	0
Header			Packet Type								Board ID							
			Sent Number															
			0	Trigger Time														
			Data Length															
			Trigger Count Upper Bits															
			Trigger Count Lower Bits															
Event Data	Hit Channel Data 0	Header	Channel ID								Length							
			Count Over Threshold															
		ADC	Summed ADC Value															
		TDC	TDC Hit 0															
			(TDC Hit 1)															
	Hit Channel Data 1	Header	Channel ID								Length							
			Count Over Threshold															
		ADC	Summed ADC Value															
		TDC	TDC Hit 0															
			(TDC Hit 1)															
	Hit Channel Data 2	Header	Channel ID								Length							
	...	...	...															
	Hit Channel Data N_{CHdata}	TDC	(TDC Hit 1)															

- data length (2 Byte) : data length for an event except for the header
- trigger count (4 Byte) : identification number of a trigger signal

The event data is constructed from samples stored in ring buffers, which corresponds to waveform and timing information every 33.33 ns. Each sampling is composed of ADC and TDC values on all 48 channels. The raw mode includes 32 samples for a 1.07 μs event window. However, it may contain unnecessary data such as data of no-hit channel, and its data size is quite large; another mode with suppressed data size is required for the physics measurement to operate with a higher trigger rate. To this end, the suppress mode is also implemented in the firmware. In this mode,

the FPGA sends data only for channels having TDC values, and a unit of the event data is not sample data but channel data. An ADC baseline for each channel is set. When a waveform sample exceeds this baseline, the pulse-height difference between the sampling and this baseline is computed. All those differences are summed in the event window, and only the ADC sum is transmitted. This method allows for removing the undershoot effect to the ADC sum. At most two timing samples having smaller values are packed in the event data. If there are more than three timing samples in the event window, the hit flag of the second sample is assigned one. As described above, the length of both channel and event data is variable; each channel data has a header that contains information of channel number and the data length.

A.2 COTTRI FE

A.2.1 Regulator

Voltage regulators are used to convert input voltage to proper voltage for the other electronics components, so the selection of the regulators is significant. For the COTTRI FE, the required specifications of voltage regulators are:

- high power efficiency
  - all the RECBEs and all the COTTRI FEs are put in a box next to the downstream endplate of the CDC; the temperature of this box has to be low enough for the electronics operation.
- high radiation tolerance
  - as mentioned in Section 2.3.1, the radiation tolerance against total dosage of 1.0 kGy and 1 MeV equivalent neutron fluence of 1.0×10^{12} neutron/cm^2 is required during the 150-day physics measurement.
- high absolute maximum rating
  - an electronics component having a high absolute maximum rating prevents incorrect voltage settings from causing circuit damage and simplifies operation.

After the parts selection with the irradiation tests [37], it is found that the positive-switching regulator, LT8612 from Linear Technology, has enough radiation tolerance for the COMET Phase-I experiment. In addition, LT8612 has a wide input voltage range from 3.4 V to 42 V. 5 LT8612 chips are mounted on the COTTRI FE, and the operation voltage of the COTTRI FE is from 5 V to 23 V. This maximum input voltage is limited by absolute maximum ratings of the capacitors.

A.2.2 Data format

The COTTRI FE stores the 2-bit data from the RECBEs in ring buffers. For data acquisition, this data is packed in the data format described in Table A.2. Header data is composed of:

- magic words (2 Byte) : 8'hAAAA

Table A.2: COTTRI-FE data format transferred to a DAQ PC.

			15	14	13	12	11	10	9	8	7	6	5	4	3	2	1	0
Header			Magic word (16'h AAAA)															
			Trigger Mode								Board ID							
			Buffer Delay								Time Window							
			Trigger Count Upper Bits															
			Trigger Count Lower Bits															
			Reserved															
			Reserved															
			Magic word (16'h 5555)															
Event Data	Sample clock 0	2-bit data	CH7			CH6			CH5			CH4			CH3			CH2			CH1			CH0
			CH15			CH14			CH13			CH12			CH11			CH10			CH9			CH8
			...															
			CH479			CH478			CH477			CH476			CH475			CH474			CH473			CH472
	Sample clock 1	2-bit data	CH7			CH6			CH5			CH4			CH3			CH2			CH1			CH0
			CH15			CH14			CH13			CH12			CH11			CH10			CH9			CH8
			...															
			CH479			CH478			CH477			CH476			CH475			CH474			CH473			CH472
	...	...	...															
	Sample clock $N_{time\ window}$	2-bit data	...															

- board ID (1 Byte) : identification number of the COTTRI FE
- trigger mode (1 Byte) : type of the DAQ trigger
- window size (1 Byte) : time length of the taken data
- buffer delay (1 Byte) : time delay length of the taken data
- trigger count (4 Byte) : identification number of the trigger signal from the COTTRI MB
- Reserved (4 Byte)
- magic words (2 Byte) : 8'h5555

Setting two rotary switches on the board decides "board ID" and an IP address, (192.168.10.16+"board ID"). DAQ-related functions – formatting and sending the event data – start to work when a trigger signal is received from the COTTRI MB.

A.3 COTTRI MB

A.3.1 Data format

The data format of the COTTRI MB is shown in Table A.3. The header data structure for the COTTRI MB is the same as the one of the COTTRI FE. As in the case of the COTTRI FE, "board ID" in the header data is correlated with the IP address of the COTTRI MB. The COTTRI MB has one of 100 RECBEs, but the event data in a sample clock is the 12-bit scores of 90 RECBEs. This means that data from nine RECBEs for each COTTRI FE is taken by the DAQ system. The number of samples is determined by the value of the event window in the header. Two types of DAQ trigger mode are available: an external trigger mode and an internal trigger mode. In the case of the external trigger mode, the event data is formatted and transmitted when the trigger signal from the FC7 is received. The internal trigger mode works using only the internal trigger asserted by the COTTRI system in the

Table A.3: COTTRI-MB data format transferred to a DAQ PC.

			15	14	13	12	11	10	9	8	7	6	5	4	3	2	1	0
Header			Magic word (16'h AAAA)															
			Trigger Mode								Board ID							
			Buffer Delay								Time Window							
			Trigger Count Upper Bits															
			Trigger Count Lower Bits															
			Timing of Internal Trigger Upper Bits															
			Timing of Internal Trigger Lower Bits															
			Magic word (16'h 5555)															
Event Data	Sample clock 0	Score	RECBE 1 [3:0]				Score RECBE 0 [11:0]											
			RECBE 2 [7:0]								RECBE 1 [11:4]							
			RECBE 3 [11:0]												RECBE 2 [11:8]			
			...															
			RECBE 89 [11:0]												RECBE 88 [11:8]			
	Sample clock 1	Score	RECBE 1 [3:0]				Score RECBE 0 [11:0]											
			RECBE 2 [7:0]								RECBE 1 [11:4]							
			RECBE 3 [11:0]												RECBE 2 [11:8]			
			...															
			RECBE 89 [11:0]												RECBE 88 [11:8]			
	...	...	...															
	Sample clock $N_{time\ window}$	Score	...															

firmware. The timing of the internal trigger is recorded in a shift register that shifts the trigger flag every trigger-decision timing, as shown in Figure A.4. The length of the register is 32 bits equivalent to 3.2 μs.

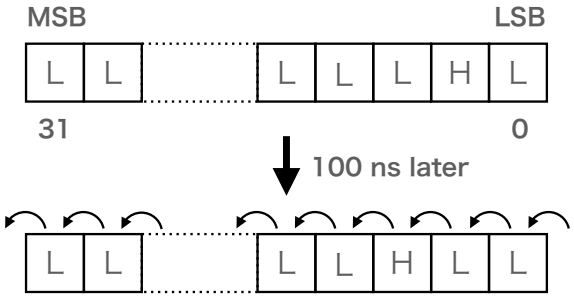

Figure A.4: Operation of the 32-bit shift register for the internal trigger. "H" (high) means that a trigger signal is generated. "L" (low) is no-trigger.

Bibliography

[1] Y. Nishina, M. Takeuchi, and T. Ichimiya. On the Nature of Cosmic-Ray Particles. *Phys. Rev.*, 52(884):1198–1199, 1937. DOI: 10.1103/PhysRev.51.884.

[2] Seth H. Neddermeyer and Carl D. Anderson. Note on the Nature of Cosmic-Ray Particles. *Phys. Rev.*, 51:884–886, 1937. DOI: 10.1103/PhysRev.51.884.

[3] J. C. Street and E. C. Stevenson. New Evidence for the Existence of a Particle of Mass Intermediate Between the Proton and Electron. *Phys. Rev.*, 52(9):1003–1004, 1937. DOI: 10.1103/PhysRev.52.1003.

[4] Hideki Yukawa. On the Interaction of Elementary Particles. I. *Proceedings of the Physico-Mathematical Society of Japan. 3rd Series*, 17:48–57, 1934. DOI: 10.11429/ppmsj1919.17.0_48.

[5] M. Conversi, E. Pancini, and O. Piccioni. On the Disintegration of Negative Mesons. *Phys. Rev.*, 71(3):209–210, 1947. DOI: 10.1103/PhysRev.71.209.

[6] E. Fermi, E. Teller, and V. Weisskopf. The Decay of Negative Mesotrons in Matter. *Phys. Rev.*, 71(5):314–315, 1947. DOI: 10.1103/PhysRev.71.314.

[7] M. Tanabashi et al. Review of Particle Physics. *Physical Review D*, 98(3):30001, 2018. DOI: 10.1103/PhysRevD.98.030001.

[8] G. W. Bennett et al. Final report of the E821 muon anomalous magnetic moment measurement at BNL. *Physical Review D - Particles, Fields, Gravitation and Cosmology*, 73(7):1–41, 2006. DOI: 10.1103/PhysRevD.73.072003.

[9] Y. Fukuda et al. Evidence for oscillation of atmospheric neutrinos. *Physical Review Letters*, 81(8):1562–1567, 1998. DOI: 10.1103/PhysRevLett.81.1562.

[10] William J. Marciano, Toshinori Mori, and J. Michael Roney. Charged Lepton Flavor Violation Experiments. *Annu. Rev. Nucl. Part. Sci.*, 58:315–342, 2008. DOI: 10.1146/annurev.nucl.58.110707.171126.

[11] E. P. Hincks and B. Pontecorvo. Search for Gamma-Radiation in the 2.2-Microsecond Meson Decay Process. *Phys. Rev.*, 73(3):257–258, 1948. DOI: 10.1103/PhysRev.73.257.

[12] Hideki Yukawa, Shoichi Sakata, and Mitsuo Taketani. On the Interaction of Elementary Particles. III. *Proc. Phys.-Math. Soc. Japan.*, 20:319–340, 1938. DOI: 10.11429/ppmsj1919.20.0_319.

[13] Yoshitaka Kuno and Yasuhiro Okada. Muon decay and physics beyond the standard model. *Reviews of Modern Physics*, 73(1):151–202, 2001. DOI: 10.1103/RevModPhys.73.151.

[14] R. H. Bernstein and Peter S. Cooper. Charged lepton flavor violation: An experimenter's guide. *Physics Reports*, 532(2):27–64, 2013. DOI: 10.1016/j.physrep.2013.07.002.

[15] A M Baldini et al. Search for the lepton flavour violating decay $\mu^+ \to e^+\gamma$ with the full dataset of the MEG experiment. *Eur. Phys. J. C*, 76, 2016. DOI: 10.1140/epjc/s10052-016-4271-x.

[16] U. Bellgardt et al. Search fro the decay $\mu^+ \to e^+e^+e^-$. *Nucl. Phys.*, 299:1–6, 1988. DOI: 10.1016/0550-3213(88)90462-2.

[17] W. Bertl, R. Engfer, E. A. Hermes, G. Kurz, T. Kozlowski, J. Kuth, G. Otter, F. Rosenbaum, N. M. Ryskulov, A. Van Der Schaaf, P. Wintz, and I. Zychor. A search for μ-e conversion in muonic gold. *Eur. Phys. J. C*, 47(2):337–346, 2006. DOI: 10.1140/epjc/s2006-02582-x.

[18] L. Bartoszek and et al. Mu2e technical design report. 10 2014. DOI: 10.2172/1172555.

[19] Benjamin Edward Krikler. *Sensitivity and Background Estimates for Phase-II of the COMET Experiment*. PhD thesis, High Energy Physics Group, Department of Physics, Imperial College London, 2017.

[20] J. Bernabéu, E. Nardi, and D. Tommasini. μ-e conversion in nuclei and Z' physics. *Nuclear Physics, Section B*, 409(1):69–86, 1993. DOI: 10.1016/0550-3213(93)90446-V.

[21] Jonathan M. Arnold, Bartosz Fornal, and Mark B. Wise. Phenomenology of scalar leptoquarks. *Physical Review D - Particles, Fields, Gravitation and Cosmology*, 88(3):1–7, 2013. DOI: 10.1103/PhysRevD.88.035009.

[22] I. Doršner, S. Fajfer, A. Greljo, J. F. Kamenik, and N. Košnik. Physics of leptoquarks in precision experiments and at particle colliders. *Physics Reports*, 641:1–68, 2016. DOI: 10.1016/j.physrep.2016.06.001.

[23] A. Abada, V. De Romeri, and A. M. Teixeira. Impact of sterile neutrinos on nuclear-assisted cLFV processes. *Journal of High Energy Physics*, 2016(2):1–36, 2016. DOI: 10.1007/JHEP02(2016)083.

[24] Japan Proton Accelerator Research Complex (J-PARC). http://j-parc.jp/c/en/index.html.

[25] J-PARC, Haddron Experimental Facility. http://j-parc.jp/Hadron/en/index.html.

[26] W. Bertl et al. A search for μ-e conversion in muonic gold. *European Physical Journal C*, 47(2):337–346, 2006. DOI: 10.1140/epjc/s2006-02582-x.

[27] R. Abramishvili et al. COMET Phase-I technical design report. *Progress of Theoretical and Experimental Physics*, 2020(3), 2020. DOI: 10.1093/ptep/ptz125.

[28] Andrzej Czarnecki, Xavier Garcia I Tormo, and William J. Marciano. Muon decay in orbit: Spectrum of high-energy electrons. *Physical Review D - Particles, Fields, Gravitation and Cosmology*, 84(1):1–8, 2011. DOI: 10.1103/PhysRevD.84.013006.

[29] Tomohisa Uchida et al. Readout Electronics for the Central Drift Chamber of the Belle-II Detector. *IEEE Transactions on Nuclear Science*, 62(4):1741–1746, 2015. DOI: 10.1109/TNS.2015.2435747.

[30] Data Sheet: AD9212. http://www.analog.com/AD9212?doc=AD9212.pdf.

[31] LTC2630. https://www.xilinx.com/support/documentation/ip_documentation/aurora_8b10b/v11_0/pg046-aurora-8b10b.pdf.

[32] Virtex-5 Family Overview (DS100). https://japan.xilinx.com/support/documentation/data_sheets/ds100.pdf.

[33] MEG-Array connector : 84512.

[34] T. Uchida. Hardware-based tcp processor for gigabit ethernet. *IEEE Transactions on Nuclear Science*, 55(3):1631–1637, 2008. DOI: 10.1109/TNS.2008.920264.

[35] Yu Nakazawa. COMET Phase-I CDC 用読み出し回路のファームウェア開発及び性能評価. Master's thesis, Osaka University, 2016.

[36] Yu Nakazawa et al. Radiation study of FPGAs with neutron beam for COMET Phase-I. *Nuclear Instruments and Methods in Physics Research, Section A: Accelerators, Spectrometers, Detectors and Associated Equipment*, 936(July 2018):351–352, 2019. DOI: 10.1016/j.nima.2018.10.130.

[37] Yu Nakazawa et al. Radiation hardness study for the COMET Phase-I electronics. *Nuclear Instruments and Methods in Physics Research, Section A: Accelerators, Spectrometers, Detectors and Associated Equipment*, 955(December 2019):163247, 2020. DOI: 10.1016/j.nima.2019.163247.

[38] Eljen Technology. Fast timing plastic scintillator EJ-232, EJ-232Q. https://eljentechnology.com/products/plastic-scintillators/ej-232-ej-232q, 2016.

[39] M. Pesaresi et al. The FC7 AMC for generic DAQ & control applications in CMS. *Journal of Instrumentation*, 10(3), 2015. DOI: 10.1088/1748-0221/10/03/C03036.

[40] 7 Series FPGAs GTP Transceivers, User Guide (UG482). https://www.xilinx.com/support/documentation/user_guides/ug482_7Series_GTP_Transceivers.pdf.

[41] 7 Series FPGAs Data Sheet: Overview (DS180). https://www.xilinx.com/support/documentation/data_sheets/ds180_7Series_Overview.pdf.

[42] Maximum Integration Data Acquisition System. https://midas.psi.ch/.

[43] J. R. Quinlan. Bagging, Boosting, and C4.5. *In Proceeings of the Thirteenth National Conference on Artificial Intelligence*, 1996.

[44] Xilinx UG353 LogiCORE IP Aurora 8B/10B v5.2, User Guide. https://www.xilinx.com/support/documentation/ip_documentation/aurora_8b10b_ug353.pdf.

[45] Xilinx XAPP645 Single Error Correction and Double Error Detection application note. https://www.xilinx.com/support/documentation/application_notes/xapp645.pdf.

[46] Si5326 Any-Frequency Precision Clock Multiplier/Jitter Attenuator. https://www.silabs.com/documents/public/data-sheets/Si5326.pdf.

[47] Xilinx Vivado Design Suite 7 Series FPGA Libraries Guide (UG953). https://www.xilinx.com/support/documentation/sw_manuals/xilinx2012_2/ug953-vivado-7series-libraries.pdf.

[48] Yugo Matsuda. COMET実験 Phase-I CDCにおける宇宙線を用いた性能評価試験. Master's thesis, Osaka University, 2018.

[49] DAQ-Middleware Home Page. https://daqmw.kek.jp/.

[50] KiNOKO - A General-Purpose Data Acquisition System. https://www.awa.tohoku.ac.jp/~sanshiro/kinoko-e/index.html.

[51] Tai Thanh Chau. Development of front-end electronics for onlie trigger system of comet phase-i. Master's thesis, Osaka University, 2018.

[52] Thomas Lindner. Evolution of the T2K-ND280 computing model. *Journal of Physics: Conference Series*, 664(3), 2015. DOI: 10.1088/1742-6596/664/3/032021.

[53] S. Agostinelli et al. GEANT4 - A simulation toolkit. *Nuclear Instruments and Methods in Physics Research, Section A: Accelerators, Spectrometers, Detectors and Associated Equipment*, 506(3):250–303, 2003. DOI: 10.1016/S0168-9002(03)01368-8.

[54] Tatsuhiko Sato et al. Features of Particle and Heavy Ion Transport code System (PHITS) version 3.02. *Journal of Nuclear Science and Technology*, 55(6):684–690, 2018. DOI: 10.1080/00223131.2017.1419890.

[55] N. V. Mokhov and S. I. Striganov. MARS15 overview. *AIP Conference Proceedings*, 896(March):50–60, 2007. DOI: 10.1063/1.2720456.

[56] T. T. Böhlen et al. The FLUKA Code: Developments and challenges for high energy and medical applications. *Nuclear Data Sheets*, 120:211–214, 2014. DOI: 10.1016/j.nds.2014.07.049.

[57] Research Center for Electron PHoton Science (ELPH), Toohoku University. https://www.lns.tohoku.ac.jp/en/.

[58] Yuki Nakai. COMET 実験に用いるトリガー検出器の開発. Master's thesis, Kyushu University, 2 2015.

[59] Garfield++. https://garfieldpp.web.cern.ch/garfieldpp/.

[60] G Cataldi and F Grancagnolo. Cluster counting in helium based gas mixtures. *Nuclear Instruments and Methods in Physics Research, Section A: Accelerators, Spectrometers, Detectors and Associated Equipment*, 386:458–469, 1997.

[61] Ting Sam Wong. Development of prototype detector for cylindrical drift chamber in comet phase-i. Master's thesis, Osaka University, 8 2016.

[62] T Nakano et al. Multi-GeV laser-electron photon project at SPring-8. *Nuclear Physics, Section A*, pages 71c–79c, 2001. DOI: https://doi.org/10.1016/S0375-9474(01)00490-0.

[63] P. Speckmayer, A. Höcker, J. Stelzer, and H. Voss. The toolkit for multivariate data analysis, TMVA 4. *Journal of Physics: Conference Series*, 219(1 PART 3), 2010. DOI: 10.1088/1742-6596/219/3/032057.

[64] H. C. Chiang, E. Oset, T. S. Kosmas, Amand Faessler, and J. D. Vergados. Coherent and incoherent (μ-, e-) conversion in nuclei. *Nuclear Physics, Section A*, 559(4):526–542, 1993. DOI: 10.1016/0375-9474(93)90259-Z.

[65] T Abe et al. Belle II Technical Design Report. *arXiv*, pages 1–480, 2010. DOI: arXiv:1011.0352.

[66] HFBR-7934. https://media.digikey.com/pdf/Data%20Sheets/Avago%20PDFs/HFBR-7934WZ,EWZ,HWZ,EHWZ.pdf.